On-sky Applications of Adaptive Optics: Performance Measurements and Globular Cluster Photometry

by

Tarun Kumar
B.Tech., Indian Institute of Technology Bombay, 2008
M.Sc., Turku University, Finland, 2019

A Dissertation Submitted in Partial Fulfillment of the
Requirements for the Degree of

DOCTOR OF PHILOSOPHY

in the Department of Physics and Astronomy

We acknowledge and respect the Lək^{w}əŋən (Songhees and X^{w}sepsəm/ Esquimalt) Peoples on whose territory the university stands, and the Lək^{w}əŋən and W̱ SÁNEĆ Peoples whose historical relationships with the land continue to this day.

On-sky Applications of Adaptive Optics: Performance Measurements and Globular Cluster Photometry

by

Tarun Kumar
B.Tech., Indian Institute of Technology Bombay, 2008
M.Sc., Turku University, Finland, 2019

Supervisory Committee

Dr. David R. Andersen, Co-Supervisor
(Department of Physics and Astronomy)

Dr. Kim A. Venn, Co-Supervisor
(Department of Physics and Astronomy)

Dr. Colin Bradley, Outside Member
(Department of Mechanical Engineering)

ABSTRACT

With the dawn of extremely large optical telescopes (ELTs) , there is a need to develop next-generation adaptive optics systems to fully exploit D^4 capabilities. Adaptive optics is a technology-driven field that relies on new developments in photonics and electronics. Before an adaptive system is commissioned, it needs to be tested in both laboratory and on-sky conditions.

This thesis is structured around four key projects, each contributing to a better understanding of adaptive optics in astronomical applications. These projects focus on the performance of multi-conjugate adaptive optics (MCAO) systems, the development of an optical simulator, the design of a calibration unit for adaptive optics systems, and the analysis of the performance of next-generation adaptive optics technologies. These address technical challenges and innovative solutions to support next-generation extremely large telescopes such as the Thirty Meter Telescope and European-Extremely Large Telescope.

The first project centres on the photometric analysis of the globular cluster NGC 5904 (M5) using Gemini multi-conjugate adaptive optics systems, GeMS (Kumar et al., 2024a). MCAO is a significant advancement that offers a wider corrected field of view than traditional adaptive optics systems. M5 was selected for its extended structure, dense stellar population, and relevance in understanding stellar evolution and the Milky Way's history. The data is from an ongoing survey of Galactic Globular Clusters within Milkyway using GeMS. The study demonstrates how MCAO systems can achieve near-diffraction-limited imaging over large fields, enabling deeper analysis of complex stellar systems. Using near-infrared photometry, our study reveals unprecedented depths within M5, showing multiple stellar populations. It addresses challenges related to crowded fields and proposes improved correction techniques that significantly enhance the accuracy of photometric data. This project highlights MCAO's potential for future studies of globular clusters, especially with the advent of ELTs.

The second project involves the development and testing of the Herzberg NFIRAOS Optical Simulator (HeNOS), a laboratory simulator for the adaptive optics system of the Thirty Meter Telescope known as NFIRAOS. It is crucial to validate NFIRAOS performance before its deployment. HeNOS simulates wavefront corrections, allowing researchers to predict NFIRAOS's performance in real-world conditions. HeNOS uses a micro-lenslet array to simulate guide stars. When imaged this micro-lenslet array suffers from aberrations. In this project, we developed a simple imaging system to address the cause of the aberrations. Challenges

like interference from camera windows and Talbot effect distortions are explored, and the results contribute to refining NFIRAOS's design. This work not only ensures NFIRAOS's optimal performance for the TMT but also provides valuable insights for other MCAO systems. The development of HeNOS is vital for the successful implementation of adaptive optics in future large telescopes.

The third project focuses on the design and implementation of a precision calibration unit for the Keck Telescope's adaptive optics systems (Lin et al., 2020). This unit is essential for achieving precise astrometric measurements, particularly by minimizing geometric distortion. It employs a pinhole mask with known reference points to calibrate the telescope's adaptive optics instruments, offering significant improvements over traditional on-sky calibration techniques, which are limited by observing time and atmospheric conditions. One key advancement is the ability to perform calibrations during the day, saving valuable on-sky time. By addressing geometric distortions in the telescope's optical system, the precision calibration unit enhances the accuracy of instruments like NIRC2 and OSIRIS which are the adaptive optics instruments of Keck I and Keck II telescopes. This project lays the groundwork for future calibration systems for adaptive optics systems like NFIRAOS for Thirty Meter Telescopes to support high-precision astrometric science.

The fourth project is a performance analysis of the REVOLT (Research, Experiment and Validation of Adaptive Optics with a Legacy Telescope) instrument at the McKellar Telescope at NRC Victoria, BC (Kumar et al., 2024b). REVOLT tests AO performance under real observational conditions, focusing on the instrument's response to environmental changes and atmospheric turbulence. This project examines the opto-mechanical design of REVOLT and its integration with the telescope, analyzing the performance of the science camera and wavefront sensors. REVOLT successfully demonstrated closed-loop single conjugate adaptive optics operation with the HEART (Herzberg Extensible Adaptive Realtime Toolkit) as Real-Time controller and First Light Imaging's C-Blue One detector as wavefront sensor. Both of these technologies will be implemented in TMT and Gemini Telescope. The research identifies residual wavefront errors, vibration-induced distortions, and overall temporal performance, providing critical data to improve the development of REVOLT. Simulations also validate the wavefront error budget, offering insights into areas for further development.

This thesis is situated at the intersection of technological innovation and scientific discovery. By addressing both this research contributes to the development of tools and techniques that will shape the future of NIR astronomy.

Contents

List of Tables

List of Figures

ACKNOWLEDGEMENTS

I am deeply grateful to my supervisors, David Andersen and Kim Venn, for their invaluable mentorship, unwavering encouragement, and patience over the past six years. Their guidance has been instrumental in shaping me into an astronomer.

I extend my sincere appreciation to the entire NRC adaptive optics group for their support, with special thanks to Jean-Pierre Veran for the opportunity to work in the AO laboratory, and to Kate Jackson and Olivier Lardiere for their invaluable assistance in the lab.

I am also thankful to Paolo Turri and Peter Stetson (PBS) for their patience and insightful answers to my countless questions on photometric analysis.

Finally, I would like to acknowledge the financial support received from NSERC, the New Technology Canadian Telescope (NTCO), and the Discovery Grant program.

Chapter 1

Introduction

This thesis presents a multifaceted exploration of the on-sky applications of AO, focusing on performance measurements, precision calibration, and photometric analysis of globular clusters. It delves into the advancements in adaptive optics technology, especially in the realm of MCAO, and how these systems improve astronomical imaging and data quality. By addressing several technical challenges and presenting innovative solutions, this thesis aims to contribute to the growing body of knowledge that supports the operation of next-generation telescopes like the Thirty Meter Telescope (TMT). The work is built on four core projects, each contributing to a broader understanding of AO in astronomy. These projects focus on testing the performance of an MCAO system by analyzing the M5 data, the development of an advanced optical simulator, the design of a high-precision calibration unit for telescopes, and performance analysis of the REVOLT instrument. Each of these projects plays a role in addressing both the scientific potential and technical limitations of adaptive optics systems. Before discussing each of these projects, we will briefly introduce MCAO technology.

1.1 Multi-Conjugate Adaptive Optics

Stars, other than the Sun, are sufficiently far away to appear point-like, thus the light that reaches the Earth's atmosphere is well-represented by a plane wave. If the Earth had no atmosphere, this plane wave would be captured as an image that is the absolute value of the Fourier transformation of the entrance pupil squared. For a circular telescope, this diffraction-limited image is an Airy disk, *i.e.*, where most of the light is focused in a small

core with concentric bright rings surrounding it. This response of an imaging system to a point source is the PSF and in this particular case, the Airy disk is a diffraction-limited PSF. The resolution of this imaging system is given by its full width at half maximum (FWHM) $\sim 1.22\lambda/D$ where, λ is the wavelength and D is the size of the aperture (see Fig. 1.1a). In reality, the Earth's atmosphere creates turbulence due to heat from the Sun and differential mixing by winds, which creates eddies of different temperatures that cause variations in the indices of refraction. A plane wave passing through this turbulence will be distorted, and the wavefronts will no longer remain parallel to each other as they arrive at the telescope. The image created when averaged over many realizations leads to a blurry image, degrading the angular resolution. The size of the blurring effect is the 'seeing' (Roddier, 1981). In seeing limiting conditions, the size of the image is not limited by the aperture of the telescope, but by "seeing," often defined as the FWHM of the image, λ/r_0, where r_0 is the coherence length of the atmospheric turbulence also known as Fried parameters. The Fried parameter (r_0), is a measure of atmospheric turbulence strength and is given by the equation:

$$r_0 = \left(0.423\, k^2\, \sec(\zeta) \int_0^\infty C_n^2(h)\, dh\right)^{-3/5}$$

where:

- k is the wave number, defined as $k = \frac{2\pi}{\lambda}$, where λ is the wavelength of light (in meters),
- $\sec(\zeta)$ accounts for the zenith angle ζ,
- $C_n^2(h)$ is the refractive index structure constant at height h, representing turbulence strength (in $\mathrm{m}^{-2/3}$),

A simplified approximation of the Fried parameter for vertical viewing ($\zeta = 0$) is:

$$r_0 \approx 0.185 \left(\frac{\lambda^2}{C_n^2}\right)^{3/5}$$

where C_n^2 represents an approximate constant value of turbulence strength near the ground.

The typical value of $r_0 \sim 10$ cm at visible wavelengths at most observatories; thus, building a larger telescope (D $\gg r_0$) does not improve the resolution and will always be

limited by seeing (Tyson, 2015).

AO mitigates blurring of the PSF by trying to correct for the effects of atmospheric disturbances, allowing a telescope to achieve near diffraction-limited images from the ground. Traditional AO uses a bright star, a NGS, that is close to the astronomical target to measure the details of the atmospheric turbulence using a WFS. A real-time control system uses measurements from the WFS and sends commands to the DM to cancel the effects of turbulence. The result is that the light reflected from the DM to the science camera is much closer to a plane wave, and can produce images consistent with the diffraction limit of the telescope (for a more comprehensive review of AO, see Davies & Kasper, 2012). In Fig. 1.2, the basic principles of AO are illustrated. Performance of an AO system is characterized by the SR, which is the ratio of the peak in the core of an AO-corrected PSF to the theoretical diffraction-limited PSF (see Fig. 1.1b). Thus, a high value indicates a better correction. A classical AO system works best when light from the object and guide star passes through the same turbulent volume. If the science target is too far from the NGS, the WFS makes a measurement of the wavefront that is not the same as the wavefront in the direction of the science target, thereby leading to a decrease in the level of AO correction. This effect is called *anisoplanatism* (see Fig. 1.3a). It defines the angular region over the sky where the atmospheric turbulence is similar enough that a single correction (derived from a guide star or laser) remains valid. The isoplanatic angle is given by (θ_0):

$$\theta_0 = 0.314\frac{r_0}{h}$$

Where

- r_0 being the Fried parameter (coherence length of turbulence) defined above,
- h the effective turbulence altitude (weighted average of the turbulent layers' heights).

The RMS wavefront error due to anisoplanatism (σ_{ani}) expressed in radians is typically given by:

$$\sigma^2_{\text{ani}} \approx \left(\frac{\theta}{\theta_0}\right)^{5/3}$$

Here, θ is the angular separation between the science target and the guide star (in radians).

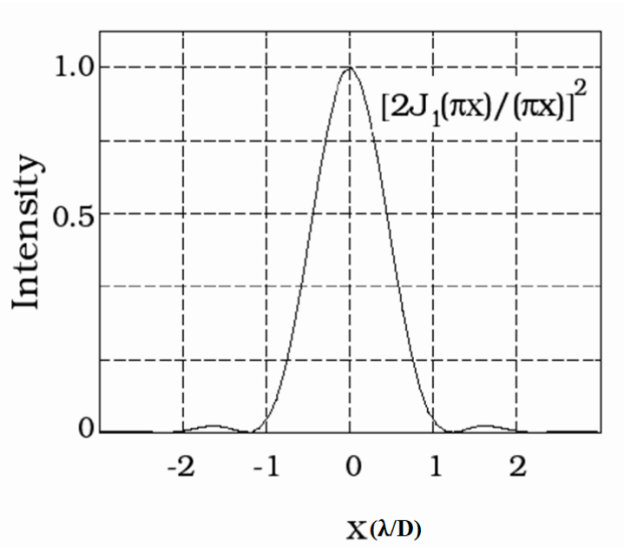

(a)

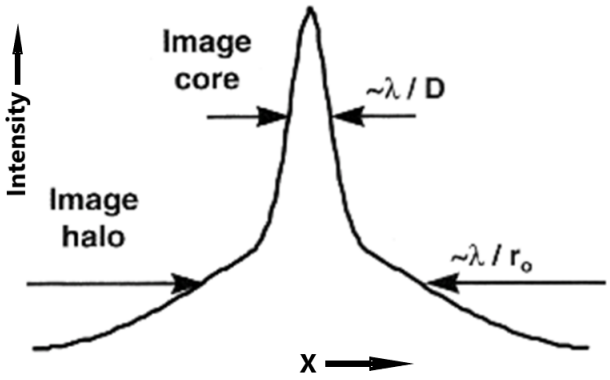

(b)

Figure 1.1: (a) Theoretical diffraction limited PSF of a point source observed with a circular telescope (also known as Airy disk) with most of the light in the core. (b) PSF of a point source after AO correction with diffraction-limited core and seeing-limited halo or wings. The ratio of the peak of flux with AO corrected PSF to that of the Airy disk is known as SR. Figures adapted from C. Max [1]

[a]http://www.ucolick.org/ max/289/

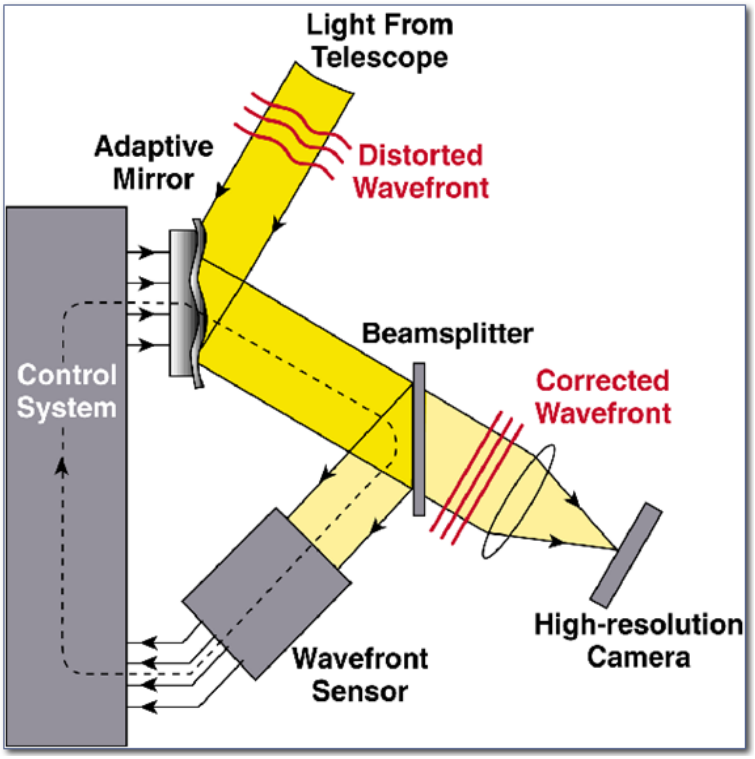

.

Figure 1.2: Basic principle and optical path for AO: Light from the guide star arrives at the telescope and reaches the deformable (or adaptive) mirror. A beam splitter splits the light into two beams: one going to the WFS, which records the turbulence information and sends it to the control system, and the other to the science camera. The control system creates the shape to be applied on the DM to correct the distortion and sends the command to the DM. This corrects the distortion and yields a flat wavefront that reaches the science camera. Figure adapted from Max, 2001

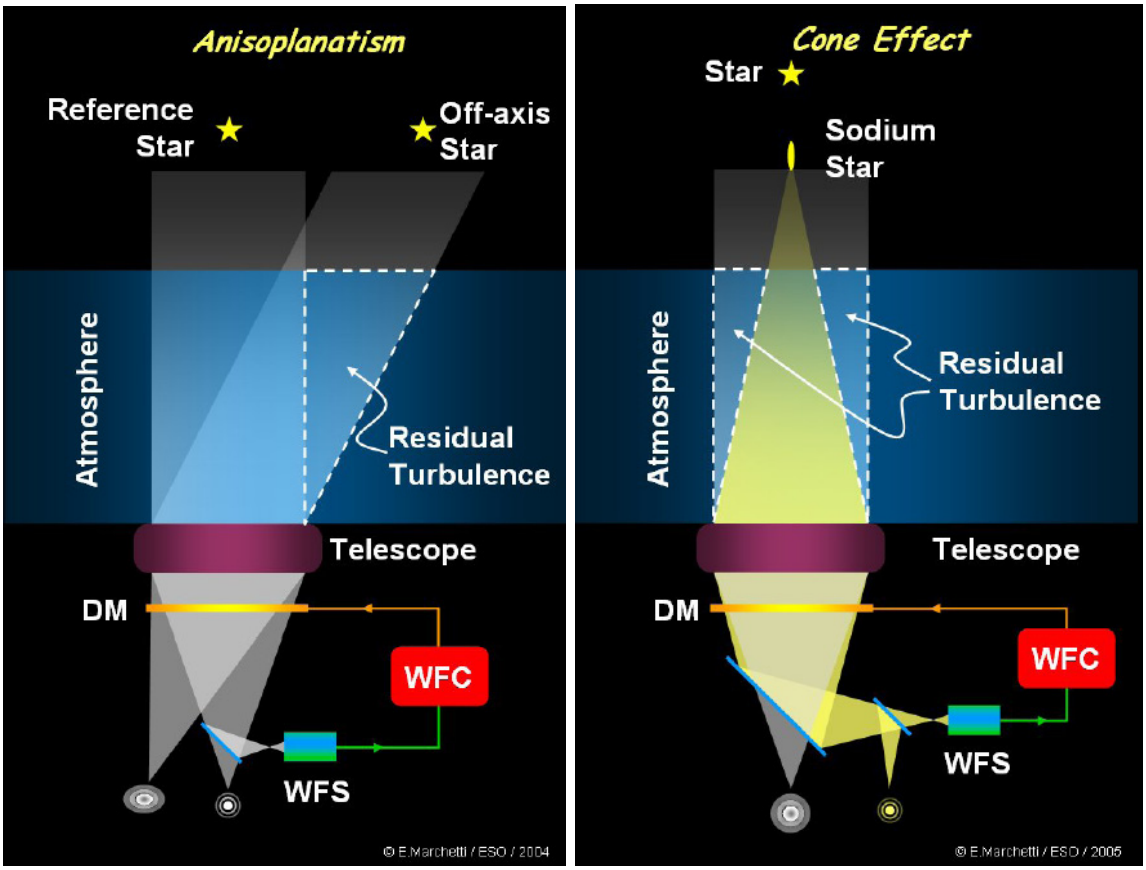

(a) (b)

Figure 1.3: Limitations of SCAO: (a) Turbulence seen by WFS differs for reference star and target (b) A LGS increases the sky coverage but suffers from cone effect due to finite altitude above the telescope (Credit: Marchetti/ESO).

Bright stars needed for AO corrections are not common, which limits the sky coverage of classical AO systems (Roddier, 2004). This sky coverage limitation can be overcome by using a LGS. A powerful laser beam is launched in the direction of the target object from the telescope (See Sandler, 1999 for a comprehensive review of LGS AO). In the most common LGS AO systems, the light is absorbed by the sodium layer of the atmosphere at an altitude of 90 km, which then fluoresces, creating a spot that serves as an artificial guide star (Pfrommer & Hickson, 2010). However, a LGS suffers from the cone effect due to the finite altitude of the sodium layer (see Fig. 1.3b) (Rigaut & Gendron, 1992). Also, the LGS is blind to tip-tilt corrections, as the light follows the same path up and down. Therefore, an NGS is still required, but the NGS can be fainter, as it is only needed to sense tip/tilt and focus (due to variations in altitude of the sodium layer).

A traditional SCAO system provides corrections over a few arcsec FOV in the NIR (typ-

ically between 1-2.5 micron) due to anisoplanatism (see Fig. 1.3) which limits the scientific usefulness of AO observations when observing extended or multiple targets in the vicinity of a guide star. An improvement in the field coverage can be achieved by Ground Layer adaptive optics (GLAO) system which employs an ensemble of guide stars typically a combination of NGSs and LGSs and multiple WFSs to drive a single DM conjugated to the ground layer (Tokovinin, 2004) since a dominant fraction of atmospheric turbulence is concentrated in the ground layer (Vernin & Muñoz-Tuñon, 1994). This allows GLAO system to provide much wider FOV coverage than traditional SCAO at the expense of resolution; GLAO effectively provides an improvement on the seeing, not diffraction-limited performance. A Multi-Object adaptive optics (MOAO) (Vidal et al. (2010); Gendron et al. (2011)) system provides high-resolution correction for multiple, widely separated science targets simultaneously. It uses an open-loop method to perform tomographic reconstruction from multiple guide stars to estimate atmospheric turbulence and applies custom corrections via individual deformable mirrors in each science channel. Because MOAO correction is highly localized and GLAO corrects only low-altitude turbulence, neither approach can supply the uniformly high-resolution imaging required for extended objects such as globular clusters.

A MCAO system overcomes this limitation by using several guide stars and multiple DMs that are conjugated optically to different heights in the Earth's atmosphere to provide a relatively uniform, near-diffraction-limited correction (see Fig. 1.4) over a FOV that can be up to 20 times that of a classical AO system (Rigaut & Neichel, 2018). The GeMS uses a combination of three NGSs, five sodium LGSs and two DMs conjugated to 0 km (ground layer) and 9 km above the telescope to provide correction over a 85"x85" FOV (Rigaut et al., 2014; Neichel et al., 2014a). The upcoming Extremely-Large Telescopes (ELTs) will be equipped with MCAO systems, including a similar combination of NGSs and LGSs, *e.g.*, Multi-conjugate Adaptive Optics for ELT Observation for E-ELT (MORFEO) (Diolaiti et al., 2010; Ciliegi et al., 2024), and NFIRAOS (Crane et al., 2018). The investigation of current GeMS performance and the scientific exploitation of its data products provide us with a unique opportunity to prepare for the future ELTs.

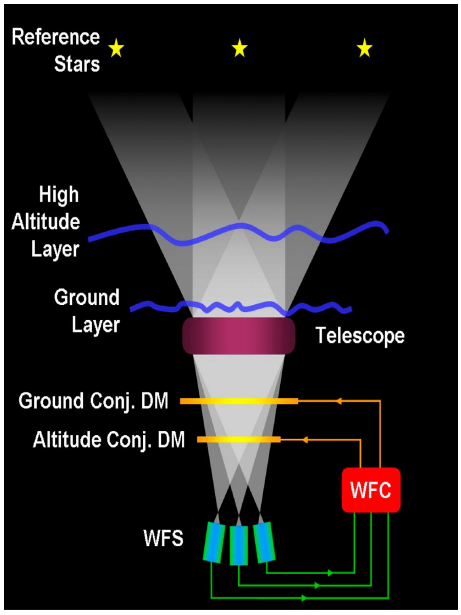

Figure 1.4: Principle of an MCAO system: Tomography of the atmospheric turbulence volume above the telescope is performed using a combination of multiple NGS and LGS WFS simultaneously. Measurements of the WFSs are combined in real-time to generate the commands applied on the DMs, which are optically conjugated typically to two or more layers in the atmosphere– the ground layer (close to the telescope) and one or more high altitude layers. DM commands are optimized to maximize the correction over a large, uniform scientific FOV. [3]

[c]https://www.eso.org/public/images/eso0719c/

1.2 MCAO Performance with Globular Cluster Photometry

The first project of this thesis centres on the photometric analysis of the globular cluster NGC 5904 (M5) using the GeMS (Carrasco et al., 2012a; Rigaut et al., 2014; Neichel et al., 2014a; Neichel et al., 2014b; Turri et al., 2015). Globular clusters are the perfect test subject to analyse the performance and capability of MCAO systems for several reasons: Firstly, they are extended objects with typical sizes of a few arcminutes, which makes them hard to observe with traditional AO systems. Secondly, they typically have a dense core of stars, which truly test the resolving power of an AO system (Moretti et al., 2009; Massari et al., 2016a,b). Finally, they are important scientific targets as globular clusters help answer numerous questions related to stellar evolution, stellar dynamics, variable and binary stars, and the conditions present during the formation of the Milky Way (Gratton et al., 2004; Renzini, 2013, 2017).

Recently, the Advance Camera for Surveys (ACS) (Sarajedini et al., 2007), the Hubble Space Telescope UV Legacy project (Piotto et al., 2015), and Gaia DR2 (Gaia et al., 2018) have produced deep UV and optical photometry of many Globular Clusters (GCs) in the Milky Way thereby allowing the creation of high-quality, deep CMDs in both UV and visible bands. Fitting the CMDs with stellar evolution models allows one to determine the age, distance, metallicities, and reddening of the clusters and to test theories of stellar evolution and star cluster formation. These models generally assume that the GCs are composed of stars with virtually the same chemical composition formed nearly at the same time. However this assumption has been challenged recently as a number of GCs, including NGC 5904 (M5), have been found to be harboring multiple stellar populations (Milone et al., 2008; Piotto et al., 2015).

While significant effort has been expended to obtain deep UV-VIS photometry of galactic globular clusters, especially using HST surveys, little work has been done to obtain equivalent NIR photometry. NIR photometry has certain advantages over UV-VIS photometry. First, NIR photometry does not suffer from differential reddening. Second, the main sequence in NIR CMDs shows a characteristic "S" shape also known as MSK, which can be used as an absolute age indicator, as it does not depend on the distance, extinction, or photometric calibration (Bono et al., 2009). The MSK is only observable in the NIR (see Figure 5 in Milone et al. (2017)) and is due to collision-induced absorption of hydrogen molecules in low mass M-dwarfs (Borysow et al., 2001; Borysow, 2002; Richard et al., 2012; Milone et al., 2019).

Milone et al. used a HST large programme survey to obtain deep NIR (F110W and F160W) photometry for NGC 2808 (Milone et al., 2012), Omega-Centauri (Milone et al., 2014), NGC 6121 (M 4) (Milone et al., 2017), and NGC 6752 (Milone et al., 2019). All these clusters show multiple sequences of low-mass stars below the MSK. These sequences are consistent with multiple stellar populations observed in red giant branch (RGB) of these clusters in UV-VIS photometry (see Figures 6, 8, 11 and 20 in Piotto et al. (2015)). Inspired by these results, similar surveys are being conducted using NIRCAM of James-Webb Space Telescope (JWST) to study globular clusters, and recent results have revealed multiple populations in lower main-sequence of globular clusters 47 Tucanae (Milone et al., 2023), in M92 (Ziliotto et al., 2023) and NGC 6397 (Scalco et al., 2024).

In this work, photometric analysis of NGC 5904 (M 5), a GC of intermediate metallicity in the NIR is presented. It has been widely studied in UV-VIS and is known to host multiple stellar populations (Piotto et al., 2015; Lee, 2017) but limited work has been done in the NIR. Coppola et al. (2012) presented deep NIR photometry of NGC 5904 using the SOFI NIR camera on the New Technology Telescope (NTT), but the CMD barely reached the main sequence turn-off point (MSTO). In this work, we present the deepest NIR photometry of NGC 5904 with a CMD clearly indicating the MSK. This globular cluster is a part of an ambitious ongoing survey (Program IDs: GS-2012B-SV-406 and GS-2013A-Q-16) to provide a comprehensive database of deep NIR photometry of Galactic globular clusters using GeMS on the Gemini South Telescope. The results of this survey have produced the deepest and most precise NIR photometry of globular clusters from the ground. Turri et al. (2017) revealed the double RGB in NGC 1857. Other observations include the robust age determination of NGC 2808 (Massari et al., 2016a), NGC 2298, and NGC 3201 (Monty et al., 2018). The clusters in this survey have already been observed with HST/ACS (Sarajedini et al., 2007) and HST/WFPC2 (Piotto et al., 2002) over a period of 5-10 years. The lower main sequence in the NIR-CMD can be used to determine binary fractions and look for mass segregation, which provides a dynamical fingerprint of the formation epoch and evolution of MSPs (see Piotto et al., 2015 and reference therein).

The GeMS analysis presented here demonstrates how MCAO systems can provide near-diffraction-limited imaging across extended fields, allowing for a deeper understanding of complex star systems. This study presents the deepest NIR photometry of globular cluster M5 to date. The photometry shows a broad dispersion in the lower main-sequence hinting at the existence of multiple stellar populations which have not previously been observed from a ground-based telescope. This work addresses key challenges in photometric extractions, particularly the effects of crowding in dense star fields, and proposes an improved crowding

correction technique that improves the accuracy of the photometric data (Kumar et al., 2024a). This project emphasizes the scientific utility of MCAO for future studies of globular clusters, as well as its potential application in the upcoming era of extremely large telescopes (ELTs).

1.3 Herzberg NFIRAOS Optical Simulator (HeNOS)

The second project focuses on the development and testing of the Herzberg NFIRAOS Optical Simulator (HeNOS), an essential component for validating the performance of NFIRAOS, the adaptive optics system for the Thirty Meter Telescope. HeNOS is designed to simulate the complex wavefront correction processes of NFIRAOS, allowing researchers to predict how the system will perform under real-world observational conditions. HeNOS serves as a critical testbed for NFIRAOS, enabling the study of wavefront corrections originating from measurements from three tier of optical wavefront sensors running at different speeds. This thesis presents work that explores various technical challenges encountered during testing, such as the interference caused by camera windows and the distortion from the Talbot effect. The results from this simulator have helped refine the HeNOS and NFIRAOS design, ensuring that it will deliver optimal performance once deployed on TMT. The development of HeNOS also provides insights into the operation of other MCAO systems and contributes to the growing body of knowledge necessary for the successful implementation of adaptive optics on extremely large telescopes.

1.4 Keck Precision Calibration Unit (PCU)

The third project focuses on the design and implementation of PCU for the Keck Telescope's adaptive optics systems. High-precision astrometry has the potential to address a variety of scientific questions, such as studying the proper motion of globular cluster member stars to analyze their dynamical properties (Massari et al., 2015; Platais et al., 2018), conducting orbital measurements of nearby binaries of low-mass stars to investigate planet formation (Rodet et al., 2018; Dupuy et al., 2018), and exploring the fundamental physics of supermassive black holes (SMBHs) (Ghez et al., 2008; Gould & Yee, 2014).

The current best solution for distortion calibration in astronomical instruments is often

referred to as the self-calibration method. This approach requires observers of crowded stellar fields to simultaneously solve for the static optical distortions of the imaging system and determine the intrinsic on-sky positions of each star. The telescope pointing is translated and rotated multiple times to move the stellar cluster across the field of view, constraining all possible distortion modes (Anderson & King, 2002; Service et al., 2019a). The precision of the self-calibration method improves with the quantity and diversity of data, but acquiring such data can be challenging due to the expensive on-sky observing time.

Astronomical instruments consist of multiple optical components, each fabricated to a certain tolerance. The accumulated effect of these imperfections can result in image distortion, necessitating periodic recalibration every few months. Most ground-based instruments utilize an external set of calibrated stellar positions, such as those from HST or Gaia, as distortion-free references, modeling the distortion as the difference between the measured positions and the external catalog (Yelda et al., 2010; Maire et al., 2016; Lu et al., 2016a; Massari et al., 2016c). While this approach reduces the need for full self-calibration, it still requires observing time to measure the reference fields. However, this technique is not inherently limited to stellar observations; it can also be applied using artificial sources, provided that the reference positions can be rotated and translated.

Thus, on-sky observations for distortion calibration can be replaced by using an internal "astrometric flat field" to measure geometric distortions. A pinhole mask with a regular grid of holes at precisely known positions is an ideal choice for such an astrometric flat field. Distortion solutions measured using an internal pinhole mask would be insensitive to optical distortions in the telescope itself and still require on-sky observations. However, in most high-resolution, AO-fed astronomical systems, higher-order distortions are dominated by the distortions intrinsic to the instrument, which can be accurately measured using the internal pinhole mask.

Using a pinhole mask for distortion solutions is not a new idea. However, previous attempts have not been able to match the accuracy achievable with images of star fields (Cameron & Kulkarni, 2007). Recent advancements in photolithographic fabrication techniques have improved the precision of pinhole masks by an order of magnitude compared to those deployed in first-generation AO systems. These masks are now sufficient to meet the distortion calibration requirements for upcoming very large aperture telescopes.

This method offers a significant improvement over traditional on-sky calibration techniques, which are limited by observing time and atmospheric conditions. One of the key

advancements in this project is the ability to perform distortion calibrations during the day, thus reducing the need for valuable on-sky time. By addressing the geometric distortions intrinsic to the telescope's optical system, the PCU improves the overall accuracy of adaptive optics-fed instruments like Keck Observatory's NIRC2 and OSIRIS, making it a valuable tool for astrometric science.

The PCU is crucial for achieving high-precision astrometric and photometric measurements, particularly in cases where geometric distortion must be minimized for scientific observations. The PCU utilizes a pinhole mask with precisely known reference points to calibrate distortion solutions for the telescope's adaptive optics instruments. Laboratory experiments have shown that current pinhole fabrication tolerances are better than 50 nm, which translates to 0.17 mas on Keck with AO–an order of magnitude improvement over current on-sky distortion calibration precision for NIRC2 (Service et al., 2019a). Thus, the proposed PCU will significantly enhance all astrometric science cases. Furthermore, the TMT plans to deploy a similar calibration unit containing a pinhole mask for NFIRAOS and IRIS, aiming for precision astrometry at the 0.05 mas level. The Keck PCU enables the development of operational models and analysis methodologies that can directly apply to the TMT. This work has been published in the proceedings of SPIE 2020 (Lin et al., 2020).

1.5 Performance Analysis of the REVOLT Instrument

The final section focuses on the performance analysis of the REVOLT instrument, an adaptive optics system integrated with the McKellar Telescope. REVOLT is a single conjugate adaptive optics instrument designed to test next-generation adaptive optics technologies. With the advent of next-generation astronomical observatories such as the European Extremely-Large Telescope (E-ELT) and the TMT, there is a growing need to develop and validate cutting-edge AO technologies. AO is an enabling technology for high-angular-resolution observations, and it continues to evolve rapidly as new methodologies, sensors, and control strategies are explored. To ensure that these innovations can deliver the required performance in real-world conditions, extensive laboratory testing and on-sky demonstrations are critical.

Several pioneering AO systems have demonstrated the feasibility and effectiveness of novel approaches, paving the way for current and future observatories. For instance, the Multi-Conjugate Adaptive Optics Demonstrator (MAD) was developed by the European Southern

Observatory (ESO) and a consortium of Italian universities to assess the performance of MCAO system and to evaluate the on-sky efficacy of pyramid WFS (Marchetti et al., 2003; Moretti et al., 2009). The success of MAD directly influenced the development of the GeMS, which has been a cornerstone of MCAO for the Gemini Observatory (Neichel et al., 2014a; Rigaut et al., 2014). Similarly, the Victoria Open Loop Testbed (VOLT) and the Visible Light Guidestar Experiments (ViLLaGEs) advanced the technology readiness of DMs and demonstrated open-loop control on-sky (Andersen et al., 2008; Ammons et al., 2008). Canary at the William Herschel Telescope (WHT) and Raven at the Subaru Telescope subsequently built upon these demonstrations to validate Multi-Object AO (MOAO) operations (Myers et al., 2008; Sivo et al., 2014; Andersen et al., 2012; Lardière et al., 2014). These early-stage demonstrators are critical as they serve as precursors to full-scale AO instruments, such as the Gemini InfraRed Multi-Object Spectrograph (GIRMOS) currently under development (Chapman et al., 2018, 2022).

Within this context of rapidly advancing AO research, the REVOLT project was established on the 1.22-meter McKellar telescope at the Dominion Astrophysical Observatory (DAO) in Victoria, Canada (Jackson et al., 2023). The primary objective of REVOLT is to enable on-sky testing of next-generation AO technologies, particularly those developed by NRC Herzberg Astronomy and Astrophysics (HAA). This testbed is instrumental in demonstrating the performance of key AO components, including wavefront sensors, deformable mirrors, and real-time control systems, all of which are crucial for upcoming AO systems at major observatories. In this project, two key technologies were tested. First, the C-Blue One detector from First Light Imaging, implemented as a high-speed SHWFS which will also be used in the NFIRAOS Laser Guide Star WFS. The second is HEART, a real-time control (RTC), developed at HAA to provide high-performance, scalable control for a variety of AO systems (Smith et al., 2022). HEART is a software toolkit designed to be adaptable to different configurations, and it will be used in future AO systems for the Gemini Observatory and the TMT.

These technologies, coupled with a commercial ALPAO DM, form the backbone of the current adaptive optics loop of REVOLT. Future upgrades to REVOLT will include the integration of a novel Micro-ElectroMechanical Systems (MEMS) low-voltage deformable mirror (LVDM) developed at the NRC Nanotechnology Research Centre in Edmonton (Ross et al., 2018). In addition to testing the fundamental adaptive optics technology, REVOLT has been used to validate new AO concepts and calibration techniques. For example, the testbed was employed to evaluate the performance of an experimental Spectral Correlation Sensor fed by an AO-corrected single-mode fiber injection unit (Cheriton et al., 2022). This

configuration helps analyze the spatial and temporal response of the system, providing a unique platform for evaluating the AO loop's stability and residual wavefront errors. Another recent experiment at REVOLT involved an open-loop channel designed to test the calibration techniques for GIRMOS (Turri et al., 2022). As REVOLT continues to evolve, its capabilities will expand, enabling more sophisticated experiments and validation studies.

For the thesis, we focused on constructing the opto-mechanical setup of REVOLT in the laboratory, then integrating it with the telescope, and finally evaluating the on-sky performance based on the science camera data and WFS telemetry. The key achievement of the REVOLT system is the on-sky demonstration of key adaptive optics technologies that will be implemented in future AO systems for the next-generation telescopes, including TMT. This work provides insights into the residual wavefront errors, vibration-induced distortions, and the overall temporal performance of the system. Additionally, the project used simulations to validate the wavefront error budget, helping to identify areas for further improvement in future adaptive optics systems (Kumar et al., 2024b).

1.6 Summary

Collectively, these projects underscore the critical importance of adaptive optics systems in modern astronomy. The performance of MCAO systems, as demonstrated through the study of M5, showcases their potential for unraveling complex stellar populations in globular clusters, a field that will greatly benefit from the high-resolution imaging capabilities of the next generation of telescopes. The HeNOS project serves as a stepping stone toward perfecting NFIRAOS, the core MCAO system for the TMT, which will allow astronomers to study the universe with unprecedented clarity and depth. The Keck PCU not only improves the precision of current astronomical instruments but also lays the groundwork for future calibration methods that will support the observational goals of the TMT. Finally, the REVOLT project adds another dimension by testing adaptive optics performance under real-world conditions, providing critical data for refining future instruments. This thesis thus positions itself at the intersection of technological innovation and scientific discovery, contributing to the development of tools and techniques that will shape the future of observational astronomy. By addressing both the technical challenges and the scientific potential of adaptive optics, this work provides valuable insights that will help pave the way for new

discoveries in the study of distant and faint objects in the universe.

Chapter 2

Photometric analysis of NGC 5904 (M5)

The work described in this section has been in published in the Monthly Notices of the Royal Astronomical Society (MNRAS) under the title Pushing the Limits of Near-Infrared Photometry with the Gemini Multi-Conjugate Adaptive Optics System: Study of crowded fields in the Globular Cluster M5 (Tarun Kumar, Paolo Turri, Kim A. Venn, David R. Andersen, Peter B. Stetson, Alan W. McConnachie and Mojtaba Taheri) is fully reproduced here as published with some improvements. For details, refer to Kumar et al. (2024a). I led all aspects of the research and writing of this article.

2.1 Introduction

Adaptive optics (AO) systems have revolutionized observational astrophysics by compensating for the wavefront distortions introduced by the Earth's atmosphere, thus providing diffraction-limited images from ground-based telescopes. However, a traditional AO system only provides correction over a small angular region around the guide star because the AO system is only getting information through the cylinder of turbulence in the direction of the guide star and as one moves away from the guide star an increasing amount of turbulence is unsensed. The angle at which the residual wavefront variance due to this effect increases by one radian is known as the isoplanatic angle (Fried, 1982; Roddier, 2004; Davies & Kasper, 2012). The isoplanatic angle is a function of wavelength and the distribution of turbulence

as a function of altitude, but is typically close to 10" in the near-infrared at a good site. To address this limitation of traditional AO systems, MCAO employs multiple guide stars along different lines of sight, each sensed by wavefront sensors in order to reconstruct the three-dimensional volume of atmospheric turbulence. To correct over a larger field of view, multiple deformable mirrors conjugated to different altitudes are required. Thus, MCAO provides a close to diffraction-limited image across a much wider field of view which allows the study of extended objects like nearby galaxies and crowded fields such as GCs with unprecedented resolution. (Rigaut et al., 2000; Rigaut & Neichel, 2018).

The first MCAO system on sky was the Multi-conjugate adaptive optics demonstrator (MAD; Marchetti et al., 2003, 2007) that was tested on the VLT (see Ferraro et al., 2009; Bono et al., 2010; Ortolani et al., 2011; Fiorentino et al., 2011). The first facility-class MCAO system is GeMS, which remains the only operational MCAO system (Carrasco et al., 2012a; Rigaut et al., 2014; Neichel et al., 2014a; Neichel et al., 2014b; Turri et al., 2015).

The upcoming generation of extremely large telescopes, e.g., the E-ELT, the TMT, and the Giant Magellan Telescope (GMT), all have plans to utilize MCAO to reach unprecedented depths and spatial resolutions on account of their enormous apertures (see e.g., Bouchez et al., 2014; Boyer & Ellerbroek, 2016; Diolaiti et al., 2016). These future ELT MCAO facilities highlight the importance of developing the necessary tools and techniques to fully exploit MCAO data from GeMS.

GeMS uses three natural guide stars, five sodium laser guide stars, and two deformable mirrors conjugated to different altitudes to provide near diffraction-limited images in the NIR across the 85" x 85" FOV of the GSAOI, which is the science instrument mounted behind GeMS. Since commissioning in 2012, GeMS routinely enables high-resolution imaging of extended and crowded stellar fields from the ground. Previous analyses of several Galactic globular clusters have been made with GeMS in the J and K_s bands, including NGC 1851, NGC 2808, NGC 6681, NGC 6652 and NGC 6723 (Program IDs: GS-2012B-SV-406 and GS-2013A-Q-16) . These clusters were selected as southern hemisphere targets that had pre-existing, high-quality, space-based imaging from the HST ACS Survey of Galactic Globular Clusters (Sarajedini et al., 2007) for direct comparisons. First results for NGC 1851 were presented in Turri et al. (2015), and later Turri et al. (2017) revealed its double RGB. Results for NGC 2808 and NGC 6681 are published in Massari et al. (2016b,a), including robust ages. In a separate program by Monty et al. (2018), NGC 2298 and NGC 3201 were also analysed to provide precision ages, distances, and reddening values. Taheri et al. (2022) used the photometric observations of NGC 6723 to study the on-sky astrometric performance

of GeMS and the astrometric capability of future MCAO systems. In this paper, we analyse GeMS observations of M5 (NGC 5904). This is the last of the early GeMS observations from this program to be analysed.

It has been suggested from both spectroscopic and photometric studies that M5 hosts multiple stellar populations. This has been determined from UV and optical photometry (Piotto et al., 2015; Lee, 2017; Mészáros et al., 2018; Lee, 2019; Marino et al., 2019), as well as from chemical abundance measurements (i.e., variations in Li, C, N, O, Na, Mg, Al and Si by Carretta et al. 2009a,c; Gratton et al. 2013; Szigeti et al. 2021; Lee 2021; VandenBerg et al. 2022; Boesgaard & Deliyannis 2023). In response, Gontcharov et al. (2019) examined a wide range of theoretical isochrones, including those with enhanced helium and a range in α-element abundances, and report a distance, true distance modulus, interstellar extinction, and age as follows: D = 7.4±0.3 kpc, $(m - M)_o$ = 14.34±0.09 mag, E(B–V) = 0.055±0.005, and Age= 12.15 ± 1.00 Gyr. This distance modulus is consistent with that from the GCs photometric investigation of M5 by Coppola et al. (2012) using the SOFI camera on the New Technology Telescope and NICS camera at Telescopio Nazionale Galileo, where $(m - M)_o = 14.39 \pm 0.10$ mag. It is also consistent with the high precision value of 7.479 ± 0.06 kpc using Gaia EDR3 astrometric data and HST photometry from Baumgardt & Vasiliev (2021). The age has also been updated by VandenBerg et al. (2014) to 11.75 ± 0.25 Gyr from isochrone fitting utilizing the data from HST UV-VIS survey (Sarajedini et al., 2007). VandenBerg et al. (2014) also determined a metallicity of [Fe/H] = –1.33 and low reddening E(B–V) = 0.032. A metallicity [Fe/H] = –1.33 ± 0.06 has also been found from spectroscopic analyses of its members (Carretta et al., 2009a; Kraft & Ivans, 2003).

M5 also appears to be tidally stripped. Grillmair (2019) detected a 50°-long stream of about 70 stars extending westward from M5 using Gaia DR2 photometry and proper motion measurements. The current mass for M5 implies it has lost 55% of its initial mass (from N-body simulations by Baumgardt et al., 2023), which may be expected given its highly eccentric orbit (e= 0.86 Vasiliev & Baumgardt, 2021).

Nevertheless, the destruction rate predicted by Gnedin & Ostriker (1997) is quite low, and the calculations by Baumgardt et al. (2023) find a half-mass relaxation time of 3.2 Gyr. These (and more) fundamental physical parameters for Galactic globular clusters are available in a database [1] managed by H. Baumgardt.

While significant effort has been put into obtaining deep ultraviolet and visible (UV-VIS)

[1]Database of fundamental parameters for Galactic globular clusters managed by H. Baumgardt (version 4, March 2023) is available here: https://people.smp.uq.edu.au/HolgerBaumgardt/globular/.

photometry of Galactic globular clusters, especially using HST, little work has been done to obtain equivalent NIR photometry. For example, the NIR study of M5 by Coppola et al. (2012) only just reached the MSTO. NIR observations have several advantages over UV-VIS photometry, e.g., they suffer less from foreground and differential reddening and sample a new portion of stellar spectra that have different sensitivities to the stellar parameters. One unique feature available in a NIR CMD is a bend and spread in the lower main sequence due to the detailed chemistry in the cluster, e.g., Calamida et al. (2009) identified a main sequence knee. This is a feature that appears only in the NIR and only at the lowest part of the CMD (Saracino et al., 2016; Milone et al., 2017, 2019; Milone et al., 2023) due to collision-induced absorption of hydrogen molecules in low mass M-dwarfs (Borysow et al., 2001; Borysow, 2002; Richard et al., 2012). For a fixed chemical composition, the main sequence knee has been used as an age indicator (Bono et al., 2010), as it does not depend on the distance, extinction, nor detailed photometric calibrations; however, VandenBerg et al. (2022) cautions that the main sequence knee is sensitive to star-to-star variations in the abundances of carbon, nitrogen, and oxygen (CNO). This has been important for the very recent analyses the NIR CMDs for two Galactic globular clusters from James Webb Space Telescope (JWST) NIRCam photometry; M92 (Ziliotto et al., 2023) and 47 Tuc (Milone et al., 2023). Both clusters reveal spreads on the CMD below the main sequence knee, which were well fit with stellar evolution models that include variations in the CNO abundances due to multiple stellar populations.

Finally, it is possible to also combine measurements from HST imaging with ground-based NIR observations, such as those from GeMS, to study the internal proper motions of member stars to fully dissect the chemical and kinematic properties of stars in Galactic globular clusters. For example, the proper motion analysis of NGC 6723 by Taheri et al. (2022) showed that the GeMS/GSAOI is able to probe to considerably smaller radii (by a factor $\simeq 5$) than either the Gaia satellite measurements or ground-based radial velocity measurements due to its superior image quality and light-gathering abilities. An early demonstration of the power in combining NIR MCAO (at the VLT) with HST NIR imaging showed that the bulge cluster NGC 6388 has two distinct (bimodal) sub-giant branches (Moretti et al., 2009). Looking at the relative proper motions and internal dynamics of M5 through multiple epochs of observations may provide clues to the existence of a central intermediate-mass black hole in the future.

In this project, we present an analysis of the Gemini GeMS J and K_s data for M5. In Section 2.2, the observations and data analysis steps from pre-processing to the profile fitting photometric extraction are presented. In Section 2.3, we present the photometric calibration,

improvement made with crowding correction, and challenges with calibration using seeing limited 2MASS system. In Section 2.4 we compare our photometry with theoretical models and discuss scientific features of the M5 globular cluster based on our new deep near-IR photometry, highlighting the evidence for multiple populations along the main sequence knee. These results are summarized as our Conclusions in Section 2.5.

2.2 Observations

Observations of M5 were conducted at the Gemini South telescope using GSAOI (Carrasco et al., 2012b) which is behind GeMS (Rigaut et al., 2014; Neichel et al., 2014a). The data acquisition took place on April 17th, 2013 under clear weather conditions. The photometric seeing measured by FWHM of the seeing disk was ~ 0.5 arcsec, while remarkably, the GSAOI consistently achieved a FWHM of ~ 0.06 arcsec in J–band using GeMS. Table 2.1 provides a summary of the observation log for the data acquired for M5. For flat field correction, standard baseline calibration files were downloaded, with observation dates as close as possible to the date of the scientific data. Table 2.1 presents the log of the data and baseline calibration files used.

Fig. 2.1 displays an image of M5 captured using the GeMS instrument, showcasing the four identified detector chips as well as the intermediate gaps between them. A dithering pattern is applied between 160 second exposures to account for the data lost due to the gaps between detectors. The combined field of view covered by the GSAOI detector is 85" x 85". The positions of the three NGS are identified. Their coordinates and magnitudes are provided in Table 2.2

2.2.1 Preprocessing

We used the Gemini IRAF package (Gemini Observatory & AURA, 2016) for flat field correction. Both dome and twilight flats were created and combined for a super flat in each of the J and K_s bands. The super flat is created by multiplying a master dome flat by the ratio of the twilight/dome master flats. This ratio has information on the spectral signature and the low-frequency variations seen on the sky instead at the dome. A top-hat median circular filter was applied to the ratio to boost the signal-to-noise ratio (SNR), while preserving the low frequency spatial variations. These super flats were divided into the science images in

Band	exp time(s)	# of exps	Data taken	Notes
J	23.5	1	2013 Apr 17	λ (500 nm) $\backsim$ 0.5”
J	90	1	2013 Apr 17	FW $\backsim$ 60 mas in J band
J	160	8	2013 Apr 17	
K_s	23.5	1	2013 Apr 17	
K_s	90	1	2013 Apr 17	
K_s	160	8	2013 Apr 17	
Associated calibration data				
J	7	10	2013 Apr 16	Dome flat
J	5.4-140	17	2013 Mar 03	Twilight flat
K_s	13	10	2013 Apr 16	Dome flat
K_s	13	10	2013 Apr 23	Dome flat OFF
K_s	15-50	8	2013 Apr 22	Twilight

Table 2.1: Observation log of M5 observed with GeMS

NGS	RA	DEC	J	H	K_s	Comment
NGS1	15:18:30.9109	+02:05:02.810	10.885	10.287	10.141	upper left
NGS2	15:18:34.8681	+02:05:07.102	9.941	9.182	8.970	upper right
NGS3	15:18:34.2382	+02:04:24.196	9.290	8.478	8.250	lower right

Table 2.2: NGS Positions and Magnitudes for GeMS M5 observations

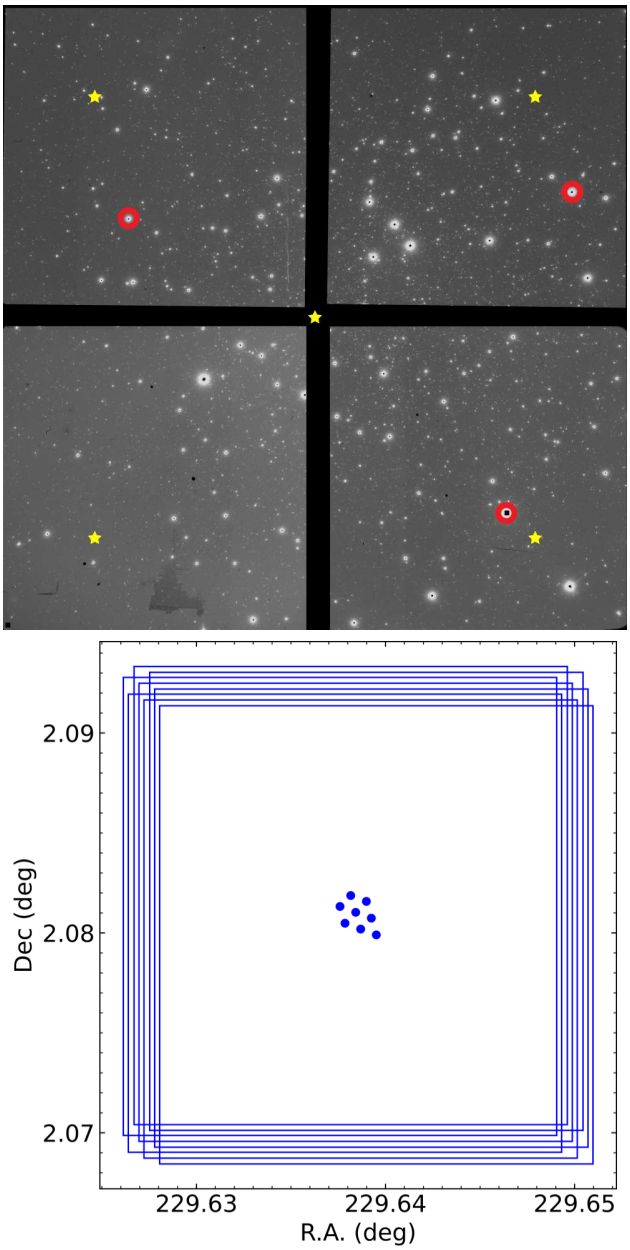

Figure 2.1: (Left) A typical image of M5 taken with the GSAOI camera which is made of 4 NIR detectors, Yellow stars shows the location of LGS and red circle NGS. In this figure, North is up and East is left. (Right) The dithering pattern was applied for 160s exposure to account for the data lost due to intermediate gaps between detectors.

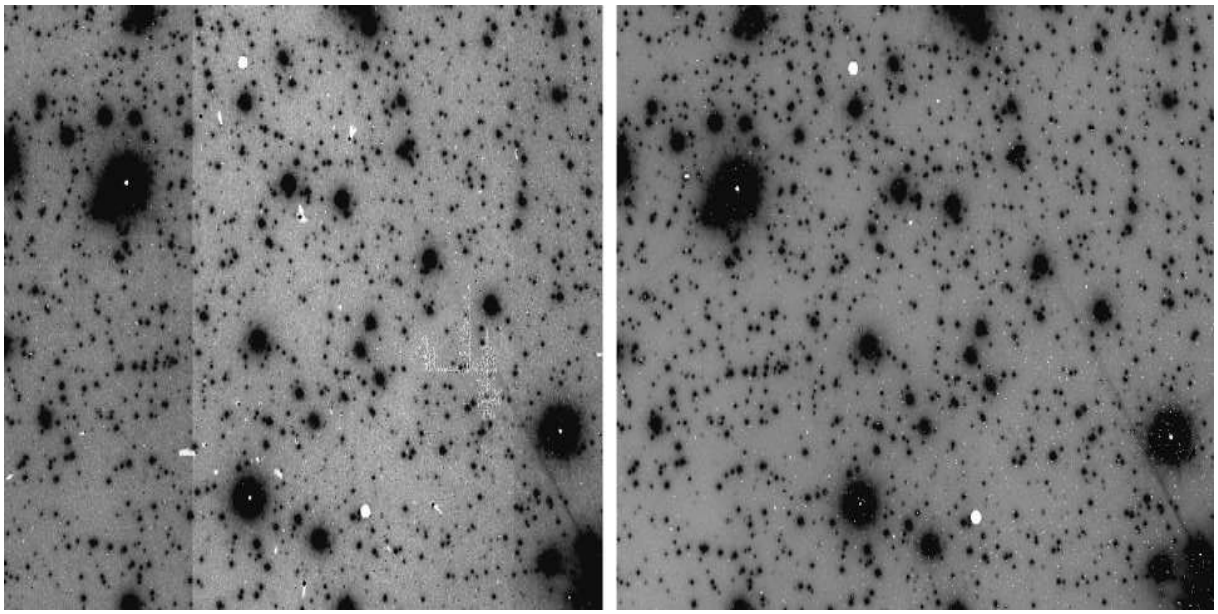

Figure 2.2: A section of chip # 1 for 160s K_s band exposure before (Left) and after (Right) the flat field correction has been applied.

each band as the flat field correction. A sample of the flat field corrections is shown in Fig. 2.2, which includes a section of chip 1 observed for 160 seconds in the K_s band before and after the flat field correction.

2.2.2 Photometric Extraction

We used the DAOPHOT-II (Stetson, 1987, 1990, 1992) package for the photometric extraction. Unlike classical adaptive optics, MCAO systems provide a relatively uniform, near-diffraction-limited correction over a wider FOV. However, there is still variation in the PSF across the GeMS FOV, especially at the edge of the field where the MCAO correction starts to drop off. Fig. 2.3 shows how the shape of tends to vary as we move from the centre to the edge of FOV. Therefore, to mimic the variability seen in the PSFs in the data quadratic spatially varying, models were computed on the individual images.

Profile-fitting photometry was performed in sequential steps to obtain the best PSF model for each chip and exposure. In the first step DAOPHOT was automatically allowed to select the PSF stars automatically which are used to model the PSF for the whole field. However, it did not perform optimal photometry due to the crowding of the field, so 100 stars were manually selected from each chip that were better suited for modelling the PSF. These stars

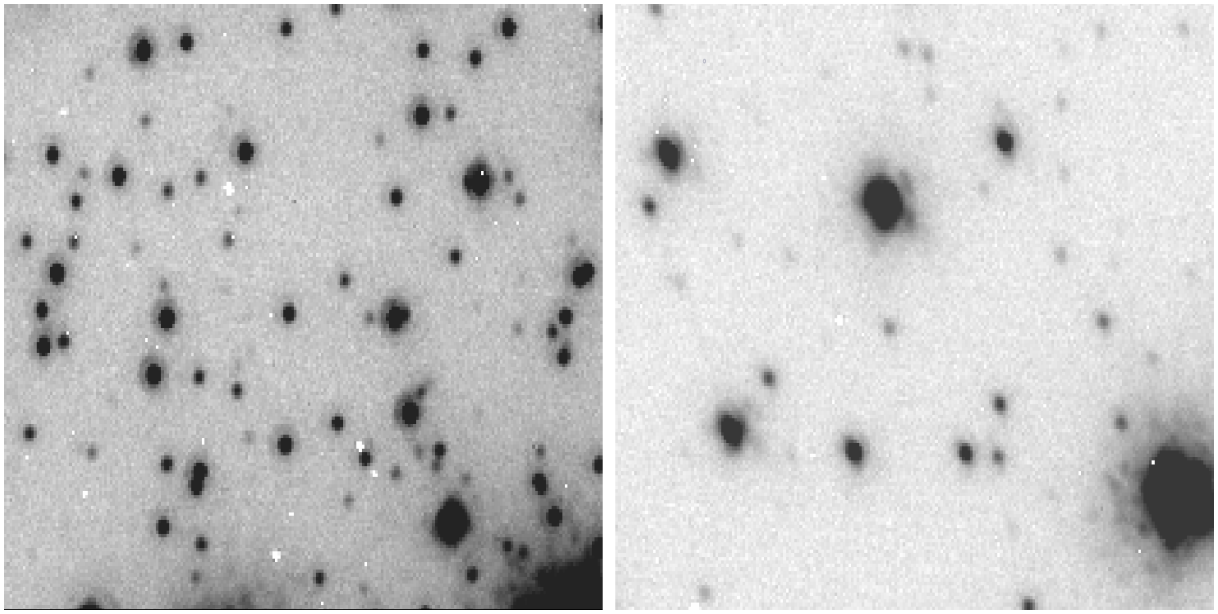

Figure 2.3: Portion of a detector at the centre (Left) and at the edge (Right) of the field of view. It can be seen that in the centre, the has a round shape while it is elongated at the edge of the detector.

were selected with the criteria that they were not too faint ($>$ 2500 ADU) or too bright ($<$ half of the threshold ADU value used), were not too close to bright or saturated stars, and were distributed uniformly across the FOV. For multiple 160 sec exposures, frames were stacked together by matching common stars between them for each chip and PSF stars were selected manually. Fig. 2.4 shows manually selected PSF stars for a stacked J band 160 sec exposure for chip # 3. J band photometry has higher residuals compared to K_s due to the relatively poor Strehl ratio of the AO corrections. However, residuals in both cases are negligible except for very bright or saturated stars (see Fig. 2.5).

2.3 Photometric Calibrations

2.3.1 Standard Photometric Catalogue

A seeing limited standard photometric catalogue for M5 was created and provided by one of the co-authors (PBS). The data for this catalogue was collected from four different instruments: Wide-field InfraRed Camera (WIRCam) at the Canada-France-Hawaii Telescope (Hawaii, US; Puget et al. 2004), Son of ISAAC (SOFI) on the New Technology Telescope (La

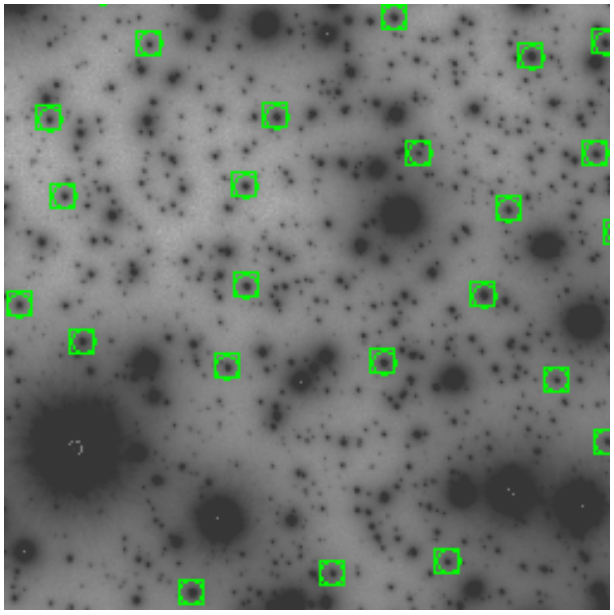

Figure 2.4: A section of one of the J band image stacks (8 exposures of 160 seconds each) used for selecting stars with good PSFs for calibrations.

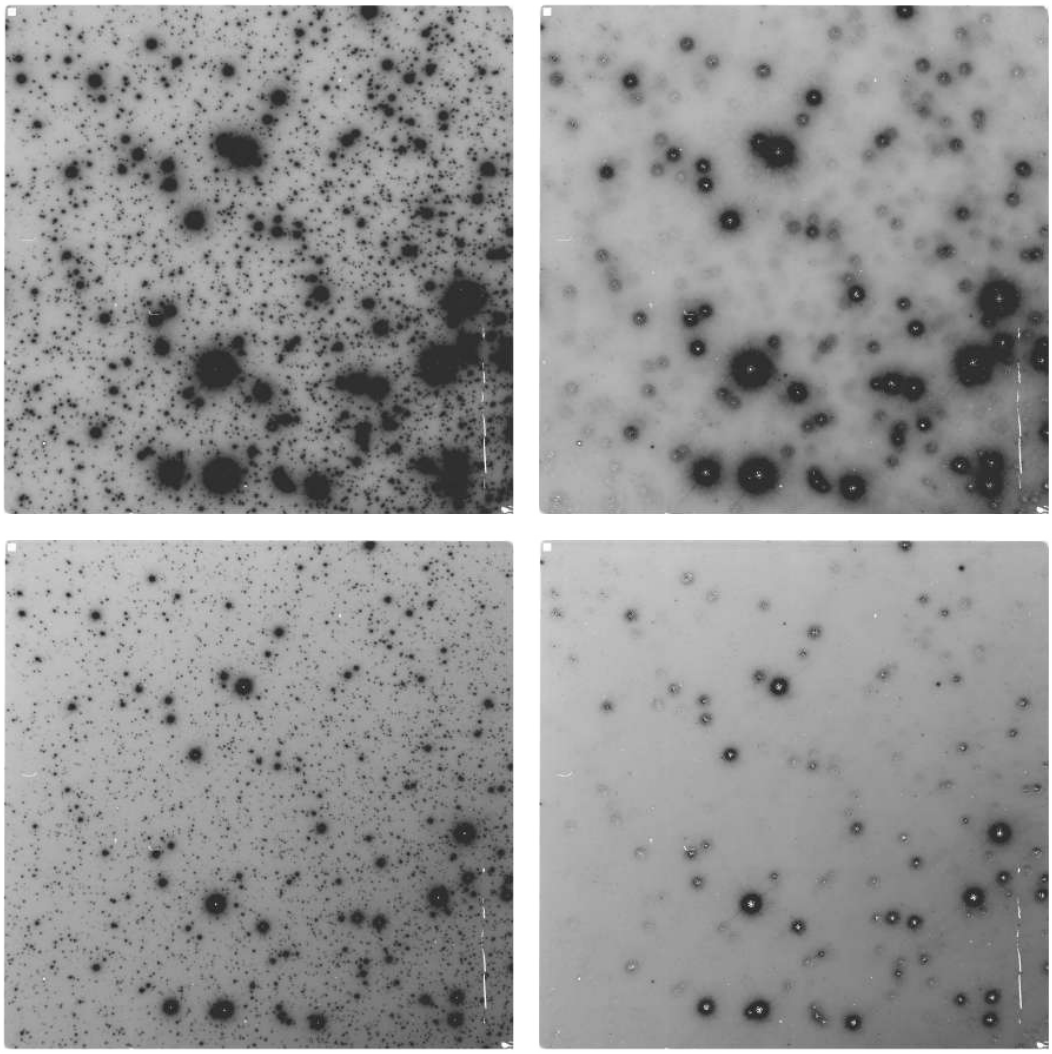

Figure 2.5: Top panels (left to right): J band image before and after the subtraction for 1st exposure of the of chip # 3. Bottom panels (left to right) show the same for Ks band.

Serena, Chile; Moorwood et al. 1998), High Acuity Wide-field K-band Imager (HAWK-I) on the Very Large Telescope (Paranal, Chile; Casali et al. 2006), and NICS on the Italian National Telescope Galileo (La Palma, Spain; Baffa et al. 2001), all under seeing limited conditions (see Fig. 2.6). The catalogue has a field of view of $\simeq$ 2000" x 2000" and was calibrated based on 2MASS photometry. This catalogue was used to define local standard stars from $10 < J < 18.5$ (see Fig. 2.7), and $10 < K_s < 18$ (see Appendix A for K_s calibration information) for our calibrations of the GeMS photometry.

We created a match file containing geometric transformation coefficients from the natural coordinate system of the GeMS images to the equinox 2000 equatorial coordinates of the standard photometric catalogue. Using these transformation coordinates and DAOMASTER PACKAGE within DAOPHOT-II, the standard photometric catalogue was matched with the GeMS instrumental magnitude catalogues for each chip and exposure, to find common stars and generate calibration curves.

Crowded regions such as in GCs, when observed in seeing limited conditions, can cause multiple neighboring stars to appear as a single 'blob' (e.g., see Fig. 2.6). Therefore, when a calibration curve is created by matching a seeing limited photometric standard catalogue with an AO-corrected instrumental magnitude catalogue created by photometric extraction using DAOPHOT (see Section 2.2.2), then multiple stars that are resolved in the AO-corrected data can be matched with a single star (or 'blob') in the standard calibration catalogue. To partially address this problem, we exclude faint stars from the standard photometric catalogue and retain only the bright stars with low photometric uncertainties (and which are also unsaturated in the GeMS images). This method retained an adequate number of calibration stars ($\sim$ 400-500) throughout the field of view to ensure accurate calibrations. An example of our fits for the J band photometry is shown in Fig. 2.7 (see Appendix A for K_s).Note that the standard photometric catalogue is always referred to as "Cat" in the Figures.

2.3.2 Zero-point calibrations

To further improve the calibration process and correct for the effects of crowding, we adopt the crowding correction technique developed by Turri et al. (2017). Improvements made to this technique are briefly summarized in Appendix A. Unfortunately, this technique does not provide homogeneous photometry when the stars are divided into groups across the field of view, e.g., AO field corrections. This behaviour is not restricted to M5, and

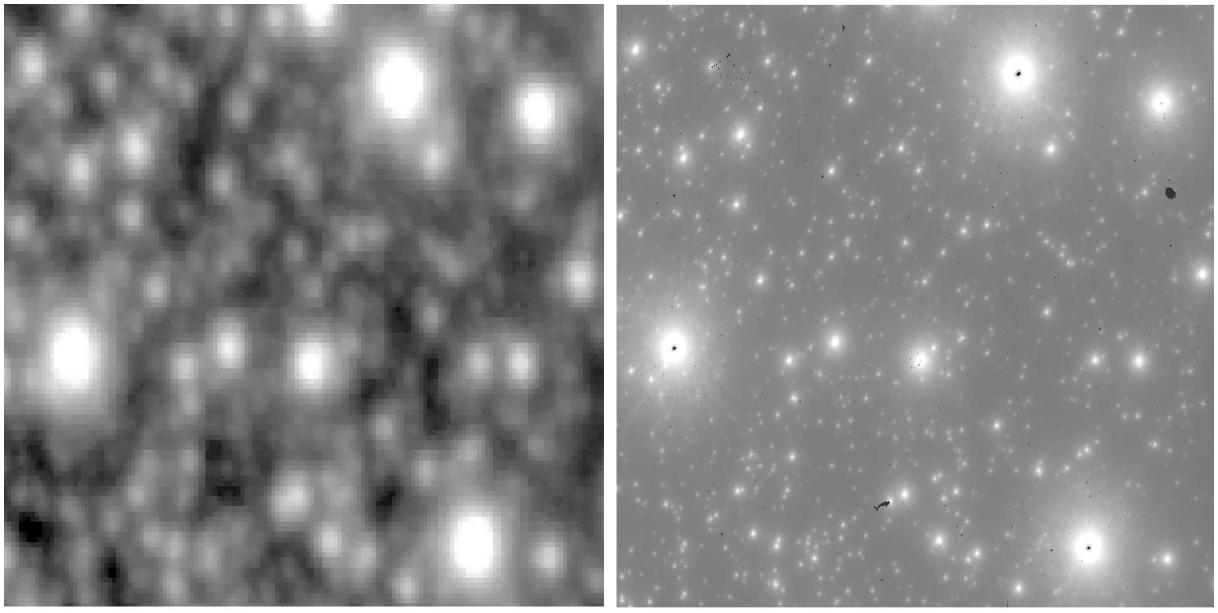

Figure 2.6: A comparison of two J band images of the same field in M5. Left: Image of M5 from the seeing-limited standard photometric catalogue as described in section 2.3.1 Right: Same section as seen from GeMS. The three brightest stars are saturated in GeMS, and therefore excluded from our photometric calibrations.

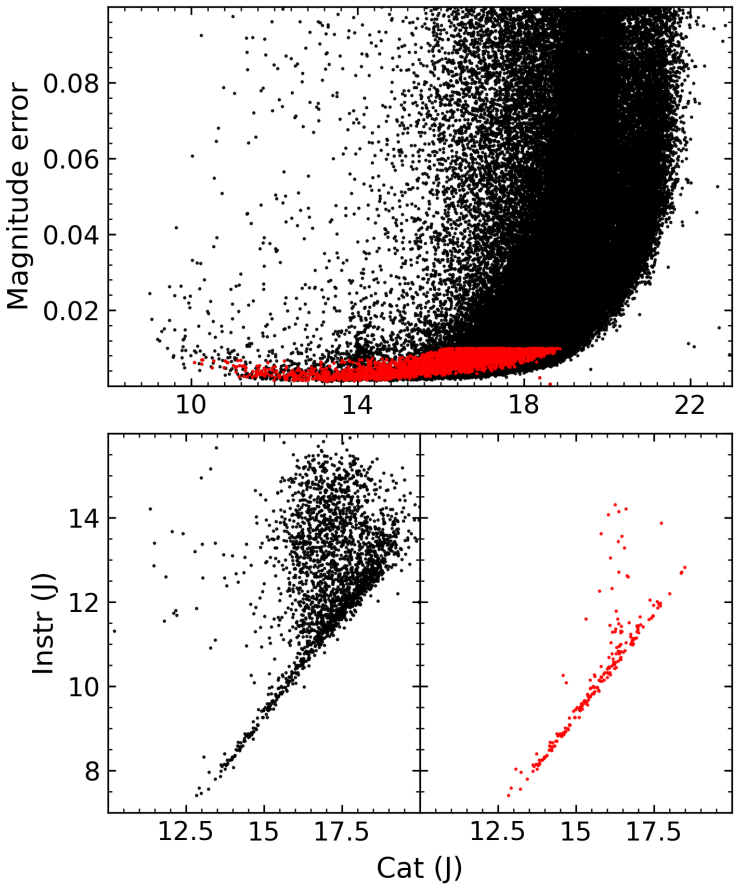

Figure 2.7: Top: J magnitude vs magnitude error for the seeing limited standard photometric catalogue. Only the red data points with low magnitude errors were used for calibration. Bottom: Instrumental J (referred to as Instr (J)) vs standard catalogue J (referred to as Cat (J)) for one of the detector chips from the 160-second exposure. Instrumental magnitudes were extracted using DAOPHOT. The left panel shows all calibration stars used, while the right panel shows only stars marked with the red points above, which clearly improves the calibration (see Appendix A for equivalent K_s band). This is further subjected to crowding correction to improve the zero-point calibration as shown in Fig. 2.8.

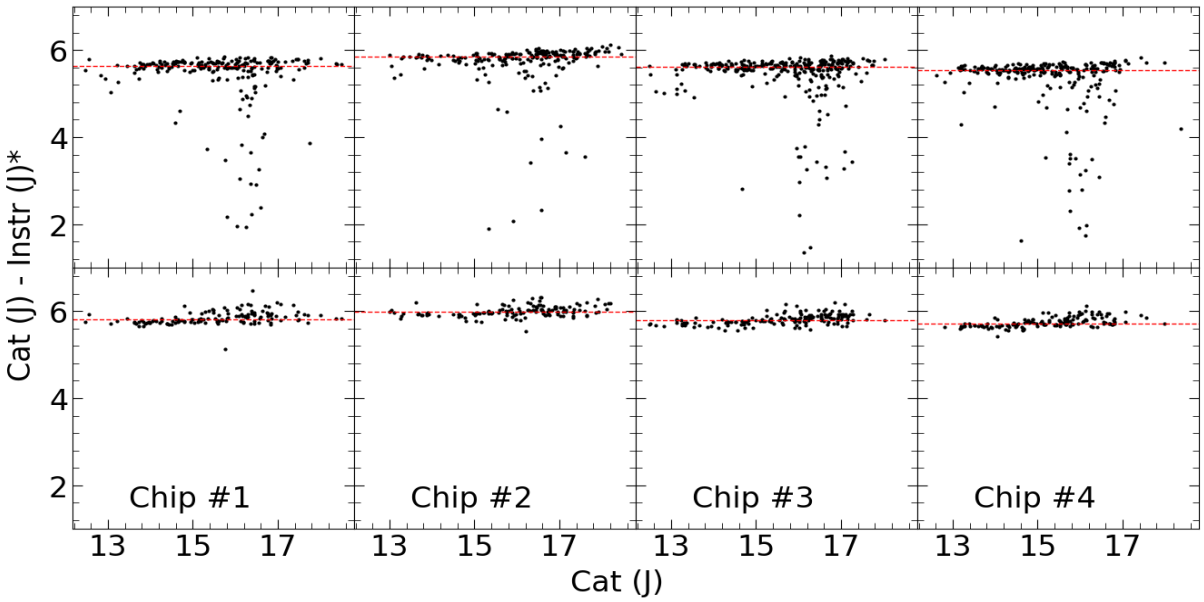

Figure 2.8: Zero-points before and after the crowding correction is applied to one of the J band 160-second exposures. Top: before crowding correction. Bottom: after crowding correction. Note that Instr(J)* refers to the instrumental magnitude in the upper panels while in the lower panels, it is the crowding-corrected instrumental magnitude (see Section A for details).

Exposure (#)	J band	K_s band	Exposure (#)	J band	K_s band
	Chip #1			Chip #2	
160s-1	5.901 ± 0.172	5.884 ± 0.165	160s-1	6.094 ± 0.117	6.002 ± 0.146
160s-2	5.865 ± 0.127	5.885 ± 0.193	160s-2	6.019 ± 0.115	6.009 ± 0.141
160s-3	5.843 ± 0.140	5.831 ± 0.179	160s-3	5.984 ± 0.117	5.982 ± 0.129
160s-4	5.818 ± 0.149	5.872 ± 0.178	160s-4	5.985 ± 0.122	6.030 ± 0.121
160s-5	5.830 ± 0.144	5.867 ± 0.178	160s-5	5.962 ± 0.111	6.007 ± 0.128
160s-6	5.869 ± 0.138	5.874 ± 0.190	160s-6	5.998 ± 0.121	6.005 ± 0.142
160s-7	5.864 ± 0.137	5.892 ± 0.182	160s-7	6.027 ± 0.118	6.026 ± 0.142
160s-8	5.944 ± 0.145	5.853 ± 0.177	160s-8	6.088 ± 0.116	6.008 ± 0.139
90s	5.266 ± 0.144	5.138 ± 0.173	90s	5.408 ± 0.124	5.359 ± 0.128
23s	3.846 ± 0.159	3.749 ± 0.186	23s	4.002 ± 0.104	3.922 ± 0.130
	Chip #3			Chip #4	
160s-1	5.885 ± 0.117	5.877 ± 0.151	160s-1	5.833 ± 0.131	5.788 ± 0.164
160s-2	5.844 ± 0.118	5.853 ± 0.158	160s-2	5.782 ± 0.111	5.793 ± 0.194
160s-3	5.807 ± 0.123	5.866 ± 0.153	160s-3	5.736 ± 0.131	5.773 ± 0.189
160s-4	5.801 ± 0.119	5.901 ± 0.163	160s-4	5.722 ± 0.114	5.827 ± 0.164
160s-5	5.808 ± 0.109	5.897 ± 0.165	160s-5	5.761 ± 0.103	5.819 ± 0.195
160s-6	5.857 ± 0.123	5.873 ± 0.163	160s-6	5.791 ± 0.108	5.791 ± 0.174
160s-7	5.833 ± 0.118	5.874 ± 0.165	160s-7	5.803 ± 0.108	5.816 ± 0.178
160s-8	5.913 ± 0.115	5.855 ± 0.173	160s-8	5.868 ± 0.109	5.814 ± 0.168
90s	5.218 ± 0.112	5.172 ± 0.168	90s	5.202 ± 0.104	5.127 ± 0.165
23s	3.772 ± 0.117	3.749 ± 0.164	23s	3.755 ± 0.111	3.674 ± 0.174

Table 2.3: Field corrections for J and K_s-band for all exposures

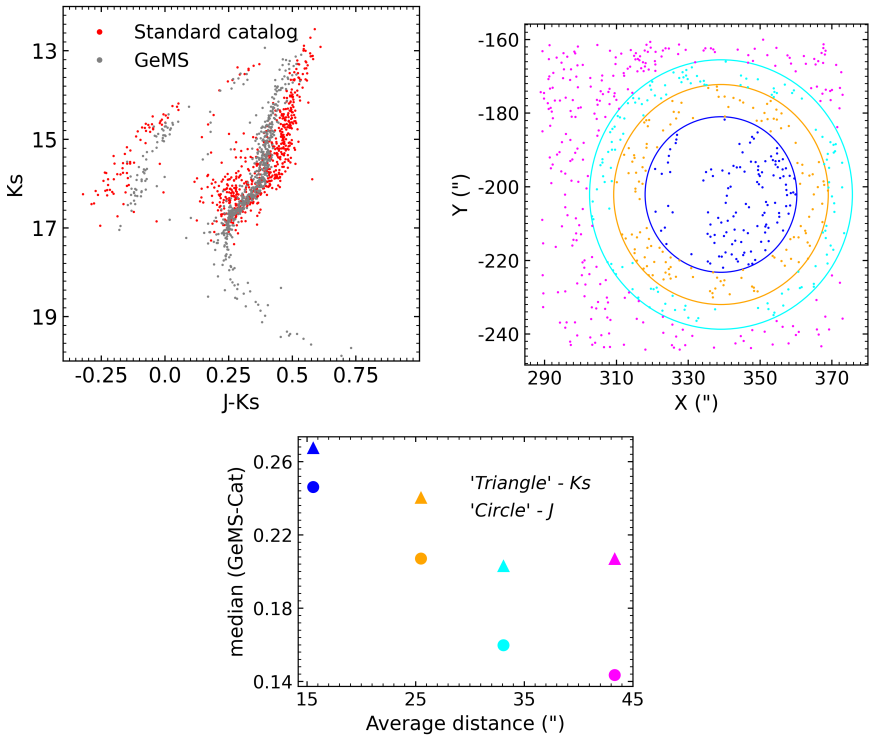

Figure 2.9: Comparison of the J and K_s photometry for common stars between GeMS photometry and standard catalogue. Top: a colour-magnitude diagram showing the common stars from both catalogues. Middle: common stars plotted in the X-Y plane as seen on sky. These common stars are divided into circular regions of equal area, from the centre of M5. Each region contains at least 100 stars. Bottom: the median difference in magnitude for each band within each region.

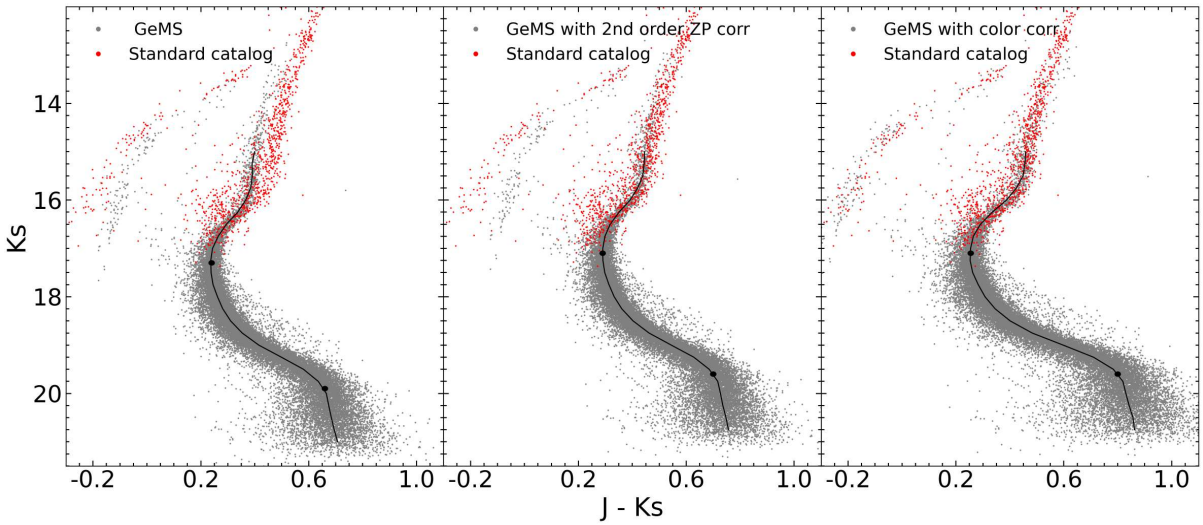

Figure 2.10: The K_s vs J – K_s colour-magnitude diagram for our GeMS photometry and the standard photometric catalogue used for calibration. The left panels show base GeMS CMD with the zero-point calibration, middle panels show when additional zero-point correction has been applied to the J and K_s bands. The last panel shows colour correction applied on top of zero-point calibration. The black curve shows the MSRL and solid dots show the positions of MSTO and MSK. See text for details.

was also observed in our independent analysis of NGC 1851 (Turri et al., 2017), but the effect is much stronger in the more crowded field of M5. Fig. 2.8 shows the impact of these field corrections after crowding corrections have been applied for one of the 160-sec exposures for the J band (see Appendix A for K_s data. Without these field corrections, the distribution of stars around the zero-point line is primarily towards the lower side (i.e., brighter magnitude) because crowding makes the stars appear brighter than their actual magnitude due to the effects of the neighbouring stars. Field corrections for all exposures and chips after the crowding corrections are presented in Table 2.3. These field corrections are applied to each instrumental catalogue before combining them to create the master J and K_s source catalogue. These catalogues are combined using DAOMASTER package to plot K_s vs J – K_s CMD. In Appendix A, CMDs with and without the field corrections are shown, including the improvement in the quality of the photometry.

2.3.3 Effects of Crowding Corrections

To investigate the potential impact of crowding on the observed differences between the CMDs, we identified the common stars between the standard catalogue and GeMS using DAOPHOT-II with positional uncertainty of 0.02" ($\simeq$ 1 pixel) (see top panel of Fig. 2.9). These common stars were initially plotted on the X-Y plane and were segmented into four circular regions with equal areas, centred on the M5 centre. We ensured that each region contained over 100 stars to derive meaningful statistics. The median difference in magnitude of stars for each region was calculated and plotted against each respective region. First, we notice that the magnitude difference decreases as the distance from the centre of the cluster for both J and K_s band (see bottom panel of Fig. 2.9). This is expected because stars farther from the core are relatively isolated and can be identified in the seeing-limited standard photometric catalogue as individual stars, aligning closely in magnitude with the AO-corrected GeMS catalogue stars. Second, the difference in magnitude is consistently larger (i.e. fainter) for K_s band than for J band. This is because *seeing* which determines the resolution of the photometry is better in K_s than in J, thus a star in a crowded region is more likely to be resolved in K_s. This implies the J – K_s colour will always be negative (or bluer). Thus, crowding explains why some standard catalogue stars appear bluer than in the GeMS catalogue (as mentioned in Section 2.3.4), i.e., RGB stars with $K_s \simeq 15$ and below, and the blue horizontal branch (HB) stars.

Finally, we note that our analysis is presented only for the GeMS FOV which is $\simeq$ 20

times smaller than the standard catalogue. Since the effects of crowding are much lower for stars in the outermost regions, e.g., those of the standard catalogue, then these differences only occur in the most crowded inner fields observed by GeMS. Therefore, we find that the bright stars ($K_s < 14$) in the standard catalogue are the most reliable, which are mostly stars from the outer regions of the GeMS FOV.

2.3.4 The zero-point corrections

When our GeMS photometry and the standard catalogue are compared directly on the CMD, we find that they do no match (see the left panel in Fig. 2.10). To address this, we examined common stars identified in both catalogues (see Section 2.3.3) and computed the median of the differences between the catalogues in their J and K_s magnitudes. These are J(Cat - GeMS) = -0.232 and K_s(Cat - GeMS) = -0.179, and when applied to our results, they improve the match with the standard catalogue on RGB. We note however that the differences for stars on the HB increased (see the middle panel in Fig. 2.10).

2.3.5 The colour corrections

The remaining differences between our GeMS photometry and the standard photometric catalogue required a final colour correction. We computed the colour terms for each J and K_s for the common stars, as shown in Fig. 2.11, and applied these to our base GeMS photometry (as shown in the right panel of Fig. 2.10). This improved the match for stars on both the RGB and HB, but stretched the lower main sequence towards the red. We note that both the zero-point corrections and colour-term corrections were computed using only the common stars, which are the brightest stars in M5. Therefore, we caution that these final corrections may be poor for stars on the lower main sequence. We also note that our standard photometric catalogue was calibrated using the 2MASS system, and specifically stars on the "red clump". While the RGB in the 2MASS photometry of M5 is clear and distinct, the HB is not. The HB exhibits high photometric errors. When comparing the standard catalogue with 2MASS, we find larger errors for stars on the lower part of the CMD (see Fig. 2.12), thus it is of limited guidance as a reference for the faintest stars in our GeMS catalogue.

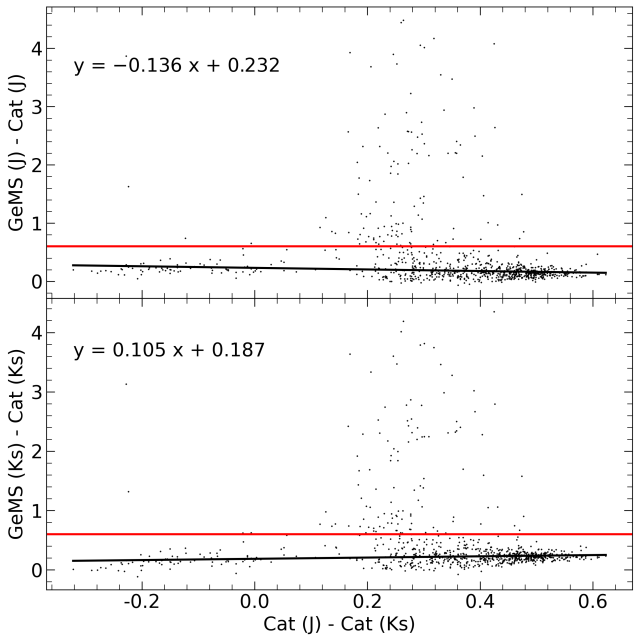

Figure 2.11: Colour corrections required to match the GeMS and standard stars photometric catalogues. Here GeMS refers to the calibrated GeMS catalogue while Cat refers to standard photometric catalogue. Only the stars below the red line (y = 0.6) were used to find the colour correction terms.

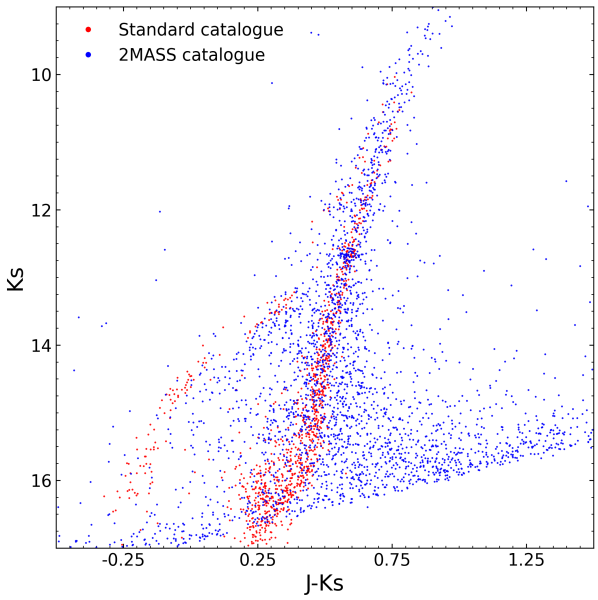

Figure 2.12: A comparison of the 2MASS catalogue (blue) and our standard photometric catalogue (red).

2.4 Discussion

2.4.1 Comparisons to Isochrones

Stellar isochrones show the instantaneous relationship between effective temperature and luminosity for a model stellar population having a range of masses, but a common fixed age and chemical abundance pattern. We generated initial stellar isochrones for M5, adopting the following parameters as from the HST F814W−F606W CMD analysis by Gontcharov et al. (2019): true distance modulus = 14.34 mag, age=12 Gyr, [Fe/H]= −1.35, Y = 0.246, [α/Fe] = 0 and reddening A_v=0.2. We note that when transformed to J and K_s using the Cardelli-Clayton- Mathis method (Cardelli et al. 1989), the reddening in the infrared bands was found to be negligible (A_J = 0.05 and A_{K_s} = 0.02). In Fig. 2.13, we then examined a wide range of isochrones and isochrone parameters to compare our photometry. These include;

- The Dartmouth Stellar Evolution model program (Dotter et al., 2007, 2008) with scaled solar abundances, and a range in age, helium Y, and [α/Fe].
- MESA models for Isochrone and Stellar evolution Tracks (MIST) (Dotter, 2016; Choi et al., 2016) with scaled solar abundances, and a range in age and [α/Fe] (only, not Y). We also explored these models with and without rotation ($v_{\rm initial}/v_{\rm critical}$) = 0 and 0.4), but found no significant differences.
- The Padova and TRieste Stellar Evolution Code (PARSEC) models (Bressan et al., 2012; Chen et al., 2014, 2015; Tang et al., 2014), also with scaled solar abundances, and a range in ages, but with fixed helium Y = 0.25 and [α/Fe] = 0. These models also include and a mass loss efficiency factor (η) = 0.2.
- Two unique isochrones to test the existence of multiple populations in the lower main sequence kindly provided by Don Vandenberg (VandenBerg et al., 2014, 2022). These two isochrones have age= 11.5, [Fe/H]=−1.33 and Y = 0.26, but one has enhanced oxygen (i.e., [C/Fe] = 0.0, [N/Fe] = 0.0, and [O/Fe] = +0.6) and the other has reduced C and O, but enhanced N (i.e., [C/Fe] = −0.80, [N/Fe] = +1.48, [O/Fe] = −0.40). These are discussed in the Section 2.4.3.

As seen in Fig. 2.13, the various isochrone grids provide similar results for a range of parameters in the metallicity range of M5. We examined age and metallicity in steps of ±0.5

Gyr and ±0.1 dex, respectively and independently, focusing on the main sequence, and to a lesser extent the RGB. We also examined Dartmouth isochrones with slightly different helium and alpha abundances; Dell'Agli et al. (2018) suggested that stars in M5 may be enhanced in helium and Carretta et al. (2009a,b) found large star-to-star abundance variations in M5; e.g., $-0.2 <$ [O/Fe] $< +0.4$ often accompanied by helium enrichment through mixing with CNO-processed gas. As the Dartmouth isochrones provided the most and widest range of parameters, we selected those to find the best fitting isochrones to our zero point and colour corrected GeMS photometry in Section 2.4.2 while no isochrones models could be fitted to our color-correction photometry.

2.4.2 Best Isochrone Fits

To find the best isochrone fits to our photometry, we began by computing a main sequence ridge line (MSRL) by gathering all of the available data in a series of boxes of depth ±0.125 in K_s and width of the full colour-axis. Median values were computed in steps of $K_s = 0.25$. These values were smoothed using a second degree spline function to generate the MSRL. For $K_s < 17$, the box width was also chosen to avoid HB stars. This MSRL represents the observed data as a single star population that we will use to compare with the isochrone models.

The MSRL has been compared to a grid of Dartmouth isochrones with ages varying from 11 – 13.5 Gyr in steps of 0.5 Gyr, [Fe/H] varying from −1.20 to −1.40 in steps of 0.05 dex, for three values of the helium abundance (Y= 0.24, 0.33, 0.40), and three values for $[\alpha/Fe]$ = 0, 0.2, and 0.4 (note that $[\alpha/Fe] = 0.2$ only was available for Y = 0.24). As we fit these isochrones to our MSRL, we also varied the distance between 6 kpc to 8.5 kpc in steps of 0.1 kpc, and varied reddening from 0.01 to 0.06 in steps of 0.01. For each isochrone, we interpolated the MSRL to get the same number of points as the isochrone between bottom of the RGB (at $K_s \sim 16.0$) and the MSK (at $K_s \sim 19.5$), and computed the net difference between the model isochrone and MSRL.

To find the best isochrone fits, we began by varying the age ± 0.1 while keeping the other parameters fixed, although we found it was necessary to also adjust the distance modulus and reddening slightly to maintain the best fits. This process was repeated for metallicity after determining the best age by adjusting [Fe/H] ± 0.01. Holding these parameters as fixed, we computing the best fit Dartmouth isochrones by adjusting the Y and [α/Fe] values. The best fit Dartmouth isochrone has an age = 13.4 Gyr, [Fe/H] = −1.29, Y = 0.24, and [α/Fe]

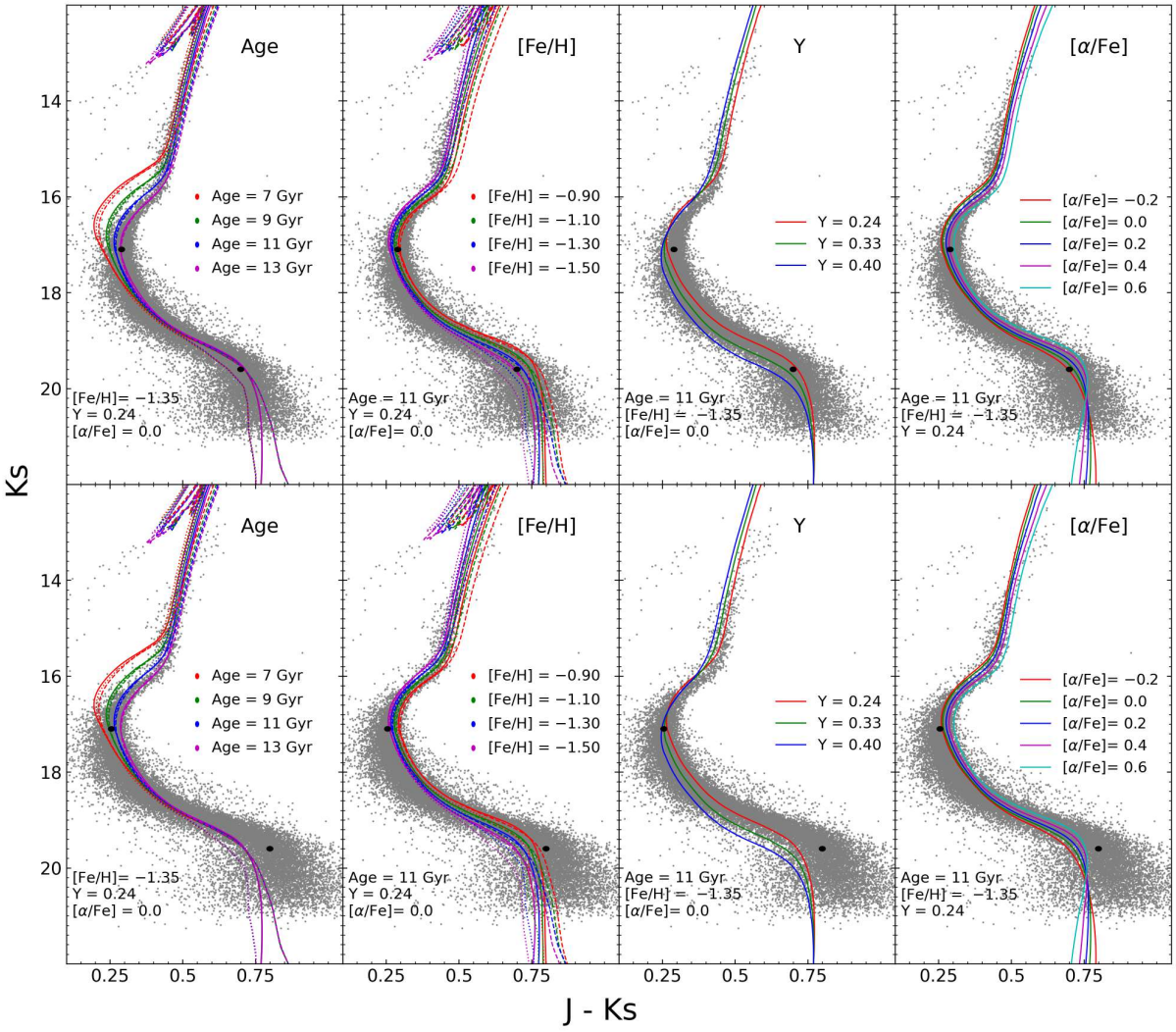

Figure 2.13: Isochrone model fits to our GeMS photometry. Top-row: GeMS photometry with additional zero-point correction applied. Bottom-row: GeMS photometry with colour corrections only for comparisons. Dartmouth isochrones are plotted as solid lines, MIST-MESA as dash lines, and PARSEC as dotted lines. The last two panels are for Dartmouth models only which include variations in helium (Y) and $[\alpha/Fe]$. A distance modulus of 14.2 mag was adopted for these plots while reddening was ignored. Solid black dots show the positions of MSTO and MSK on the CMD.

= 0.0, with distance modulus d = 14.24 mag and reddening E(J – K_s)= 0.01 provided the best fit. We note that a second Dartmouth isochrone with very similar parameters provided nearly as good of a fit; age = 13.0 Gyr, [Fe/H] = −1.29, Y = 0.33, and [α/Fe] = 0.4, distance modulus = 14.1 mag, and E(J – K_s) = 0.0 (we note that no reddening was also adopted by Gontcharov et al. (2019)). While these two isochrone fits are in excellent agreement, we note that the isochrone fit with the larger distance modulus (14.24 mag) is in better agreement with the recent value (14.37 mag) in Baumgardt & Vasiliev (2021).

Finally, we compute our photometric errors from DAOPHOT, added in quadrature, for each star within the MSRL sliding boxes. We find our photometric errors are smaller than the spread in colour along the MSRL at all magnitudes, as shown in Fig. 2.14. This suggests the colour spread along the main sequence is real, a possible indication of variations in chemical abundances (discussed below, Section 2.4.4).

2.4.3 Main Sequence Knee as an age indicator

Our GeMS J – K_s CMD is the deepest observed in the NIR for M5 so far (for comparison see Figure 2 in Coppola et al. (2011)). It clearly shows a MSK near K_s = 19.5, the first time the MSK has been observed in M5. As discussed in the Introduction, the main sequence knee can be used as an absolute age indicator, as it does not depend on the distance, extinction, nor detailed photometric calibrations. In addition, the uncertainty in the age of a globular cluster can be significantly reduced when the age from the MSK and the MSTO are used together. As an example, the absolute age of the globular NGC 3201 has been determined using both the MSTO and the MSK. The uncertainty in the absolute age was reduced by a factor of 2 when both are used simultaneously (Bono et al., 2010).

In our analysis in Section 2.4.2, we have used the MSTO and MSK together to find the best fitting Dartmouth isochrone. As seen in Fig. 2.13 (top panels), the position of the MSK in M5 is sensitive to [Fe/H], Y, and [α/Fe], but not age. This allowed us to find the age more precisely from the MSTO before iterating on the other parameters. The quality of the isochrone fits to our photometry imply an age uncertainty $\lesssim$ 1 Gyr. However, the inset to Fig. 2.14 shows that a new set of models with variations in CNO from VandenBerg et al. (2022) can fit the data well with ages of only 11.5 Gyr. To fit these new models, we also had to adjust the distance modulus slightly to 14.3 mag, which is in excellent agreement with the recent value (14.37 mag) in Baumgardt & Vasiliev (2021). This suggest that while having the MSK can help to anchor the age of a globular cluster during isochrone fitting,

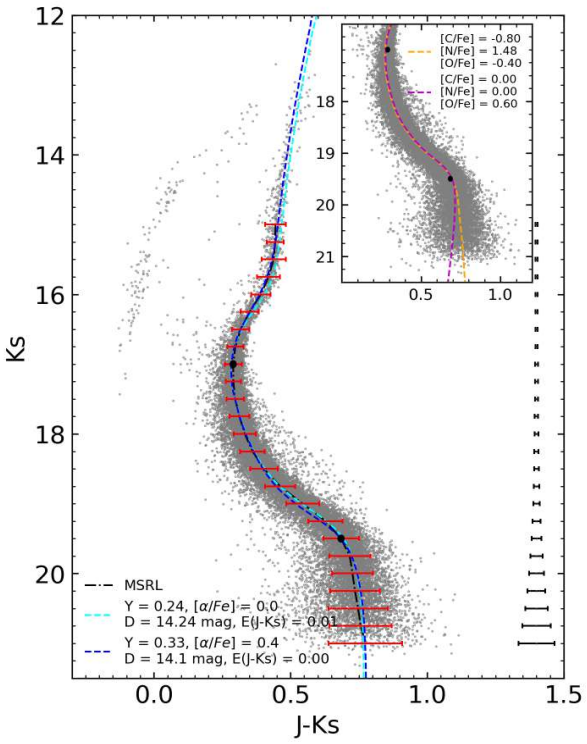

Figure 2.14: The final calibrated GeMS photometry (grey points). Our two best fit Dartmouth isochrones are superimposed: in cyan, age = 13.4 Gyr, [Fe/H] = −1.29, Y = 0.24, and [α/Fe] = 0.0, with distance modulus = 14.24 mag and reddening E(J–K$_s$)= 0.01; in blue, age = 13.0 Gyr, [Fe/H] = −1.29, Y = 0.33, and [α/Fe] = 0.4, distance modulus = 14.1 mag, and E(J–K$_s$) = 0.0. Photometric errors are shown (black lines, right side), and the main-sequence ridge line (dot-dash) and standard deviations in the data are plotted on the CMD as red lines. The inset provides VandenBerg et al. (2022) isochrones plotted with variations in the CNO abundances at fixed age = 11.5 Gyr, distance modulus = 14.3 mag, and E(J–K$_s$) = 0.03. Black solid circles on the CMDs show the location of MSTO and MSK.

systematic variations between isochrone models can still dominate the age errors.

2.4.4 Multiple populations along the Main Sequence Knee

An HST large programme survey was carried out to obtain deep NIR F110W and F160W photometry of several globular clusters, including NGC 2808 (Milone et al., 2012), ω Centauri (Milone et al., 2014), NGC 6121 (M4, Milone et al., 2017), and NGC 6752 (Milone et al., 2019). All showed evidence for multiple populations in their M-dwarfs below their MSKs due to different abundances of He (Y), C, N and O. These results were consistent with multiple stellar populations observed on their red giant branches from UV-VIS photometry (Piotto

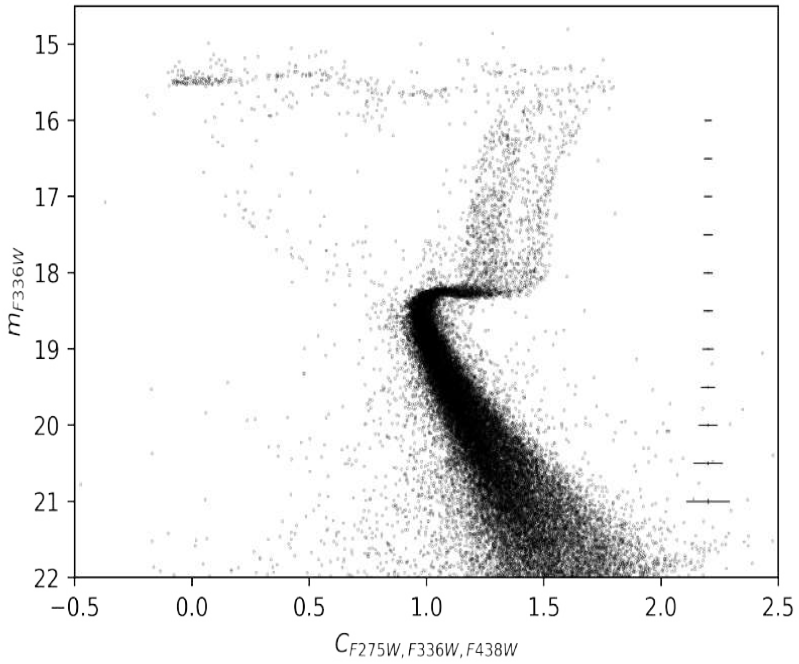

Figure 2.15: CMD of NGC 5904 plotted using HST UV-VIS filter F275W, F336W and F438W. The error bars on the right display intrinsic errors in magnitude and in colour, and were calculated using the same method as discussed above. Here $C_{F275W,F336W,F438W}$ = (m_{F275W} - m_{F336W}) - (m_{F336W} - m_{F438W}) (Piotto et al., 2015)

et al., 2015), where a pseudo colour filter based on HST F275, F336, and F438W was used to discern first and second-generation stars (Milone et al., 2013). First-generation stars have an initial mix of CNO, which is altered in the second-generation stars by CNO-cycled H-burning, such that oxygen and carbon are reduced, while nitrogen is enhanced. This UV-VIS HST program also included M5, finding evidence for multiple stellar populations amongst its RGB stars too. (see Fig. 2.15).

Follow-up studies of M5 combining spectroscopy and photometry were carried out by Mészáros et al. (2018), Milone et al. (2018), Marino et al. (2019) and Lee (2021). Mészáros et al. (2018) found evidence for multiple stellar populations on the lower RGB in M5, and found M5 has two distinct generations on the HB associated with differences in N *and* Al. Marino et al. (2019) analysed the light elemental abundances in GCs and found that second-generation stars of M5 are enhanced in N *and* Na and depleted in O. Moreover, Milone et al. (2018) computed the average ($\delta Y_{1G,2G}$) and maximum (δY_{max}) helium differences between the first and second generations in GCs, finding $\delta Y_{1G,2G} = 0.012 \pm 0.004$ and

$\delta Y_{max} = 0.033 \pm 0.007$ for M5. Lee (2021) showed three distinct populations on the RGB associated with different C and N abundance ratios and two populations of enhanced helium. As widely discussed in the literature, helium-rich RGB and main sequence stars have bluer colours than stars with primordial helium and the same luminosity (see e.g. (D'Antona et al., 2002; Norris, 2004; Sbordone et al., 2011; Cassisi et al., 2017)). In Fig. 2.14, we show that one of our best fit isochrones does have enhanced helium (Y=0.33), however our data is equally well fit with primordial Y (=0.24, after very minor adjustments are made to the other parameters, e.g., distance). We also note that the colour spread along the MSRL is significantly larger than our photometric errors at all magnitudes, i.e., the colour spread = 4 – 8 $\sigma_{\rm J-K_s}$ from the MSK to the RGB, respectively. These spreads are most likely due to variations in helium (Y = 0.24 to 0.33, e.g., see Fig. 2.13).

Below the MSK ($K_s \sim 19.5$), variations in CNO can also affect the distribution of the stars on the J–K_s CMD, particularly as the effects due to helium variations are reduced (see Fig. 2.13). In Fig. 2.14, we see that the (J – K_s) colour spread below the MSK increases slightly but so do the photometric errors, thus the colour spread remains near $4\sigma_{\rm J-K_s}$ near the MSK and reducing to 1.9 $\sigma_{\rm J-K_s}$ in our lowest bin. We suggest that this spread is consistent with the effects of variations in CNO below the MSK, and therefore the first evidence for multiple stellar populations on the lower main sequence in M5. Of course, this is also consistent with the study by VandenBerg et al. (2022) of the impact of CNO variations and multiple populations on the HST UV-VIS studies of the RGBs of globular clusters, including M5. Two of their isochrones were kindly provided to us for comparisons with our J – K_s photometry; one with enhanced O but reduced C and N, and a second with enhanced N but depleted in C and O. In Fig. 2.14 (inset), we show that the nitrogen-rich model fits our MSRL best, however both are consistent with our data.

Finally, we comment that we can not rule out field star contamination, as no proper motion analysis has been carried out; however, a significant number of non-members have been removed in a series of cleaning steps described in Appendix A. Thus, our new GeMS J – K_s photometry is consistent with other evidence for multiple stellar populations in M5.

2.5 Conclusions

In this paper, we present new near-infrared photometry in the J and J – K_s bands for the globular cluster M5 (Program ID: GS-2013A-Q-16) obtained from the MCAO system GeMS

at Gemini-South. M5 was included as one of the original six targets for a GeMS quality analysis program, and it is the final cluster to be analysed due to its high level of crowding. Our analysis of the M5 GeMS photometry has yielded the following results:

- Analysis of crowded regions presents significant data reduction challenges for adaptive optics observations.
- GeMS demonstrates exceptional capabilities in resolving crowded regions in globular clusters, enabling deep photometry in the central regions.
- Calibrations based on 2MASS are limited to bright stars and appear to be less reliable for calibrations of faint blue HB stars in M5. An adaptive optics assisted standard photometric catalogue could help to mitigate this issue.
- Our GeMS J–K_s photometry for M5 are best fit by two Dartmouth isochrone models, each providing an age = 13 ± 1 Gyr, [Fe/H] = -1.3 ± 0.1, and distance modulus = 14.2 ± 1 mag. Vandenberg isochrones with CNO variations and age = 11.5 Gyr also fit well, though with a distance modulus = 14.3 mag.
- We find a spread in the mean J–K_s colours that is larger than our photometric errors at all magnitudes for stars in M5, ranging from 8 $\sigma_{\mathrm{J-K_s}}$ at the MSTO to 4 $\sigma_{\mathrm{J-K_s}}$ at the MSK. This is interpreted as due to variations in helium Y.
- A spread in the J–K_s colour below the MSKranges from 4 to 2 $\sigma_{\mathrm{J-K_s}}$, consistent with variations in the CNO abundances that have been observed in RGB stars in M5.

This paper concludes the results from our original GeMS quality analysis program, providing insights into adaptive optics analyses in crowded fields.

Chapter 3

Herzberg NFIRAOS Optical Simulator (HeNOS)

This section outlines my initial work on the HeNOS bench to address the issues with the MLA imaging which is used as a NGS simulator. While the original plan was for me to continue this project throughout my PhD, we later shifted focus to the REVOLT project due to its urgent need for additional manpower. In this project, I primarily worked with Dave Andersen. In this project, I designed the optical setup to test the MLA imaging issue, performed experiments, and conducted literature research on the Talbot effect.

3.1 Introduction

NFIRAOS will be the MCAO facility for TMT. It includes six LGS made with SHWFSs, two DMs, and a NGS truth wavefront sensor (TWFS). NFIRAOS will feed three science instruments providing near diffraction-limited correction over a 30 arcsec FOV and partial correction over a 2 arcminute FOV in the near infrared (JHK bands). All of its opto-mechanical sub-systems will be housed in an enclosure (8m $\times$ 10m $\times$ 4m) cooled down to -30° C in order to improve sensitivity in the thermal near-infrared by reducing the thermal background (Herriot et al., 2014). Considering the scale and complexity of NFIRAOS, a scaled-down test bench, the Herzberg NFIRAOS Optical Simulator (HeNOS), was built at National Research Council Herzberg for Astronomy and Astrophysics to demonstrate the robustness and stability of a NFIRAOS-like MCAO system. The goal of HeNOS is to simulate

slowly evolving background tasks and to be used as a test bench for PSF reconstruction techniques. For a comprehensive review on HeNOS, see Véran et al. (2012); Turri et al. (2014); Mieda et al. (2018). HeNOS uses a uniformly illuminated MLA to simulate NGSs. The MLA creates a grid of diffraction-limited spots at its focal plane. However, when these spots images from the MLA propagating along the optical path of HeNOS, arrive at the pupil plane, a distorted intensity grid pattern is observed due to overlapping PSFs. In this project, I designed an imaging setup to address this issue.

3.2 Bench parameters

In this section I briefly summarize how the bench parameters are derived from NFIRAOS parameters. The parameter subscripts N and H refer to NFIRAOS and HeNOS, respectively. The main challenge in designing the HeNOS bench was to scale down the NFIRAOS to a bench size experiment and to do so a set of constraints were applied. The first set of constraints arises from the need to keep the cost down which means to work at visible wavelength in order to simplify optics alignment and to use inexpensive CCD or CMOS detectors for WFS and imaging. Therefore $\lambda_H = 0.670$ μm was set as the sensing as well as imaging (science) wavelength.

The second cost-related constraint required to work with relatively low cost DMs.Two Alpao magnetic DMs are currently installed on HeNOS: DM0 (11x11 DM with 9 actuator pitches across the clear aperture ($n_H = 9$)), conjugated to ground, and DM1 (19x19 DM with $n_H = 16$), conjugated to a high altitude. Both DMs have the same physical actuator pitch of 1.5mm. To achieve diffraction-limited imaging the turbulence, r_0, should not be significantly less than $d_H = D_H/n_H$ at λ_H. However if $D_H = 30$ m the turbulence would need to be unrealistically weak. Therefore, $D_H = 8$ m was set as the largest telescope diameter that could while simulating realistic turbulence.

Finally, considering the diameter of the simulated telescope (8 m) and the size of DMs (13.5 mm footprint for an NGS beam) the FOV of the system was limited to $FOV_H = 10.9$ arcsec on the sky which is significantly smaller than FOV of NFIRAOS ($FOV_N = 120$ arcsec). This choice gave the HeNOS designers the freedom to work with off-the-shelf optical elements in an affordable size (i.e. 1-2 inch optics). For more details on how the scaled down HeNOS bench parameters are derived see Véran et al. (2012); Mieda et al. (2018). Table 3.1 shows the NFIRAOS parameters while equivalent scaled down HeNOS bench parameters

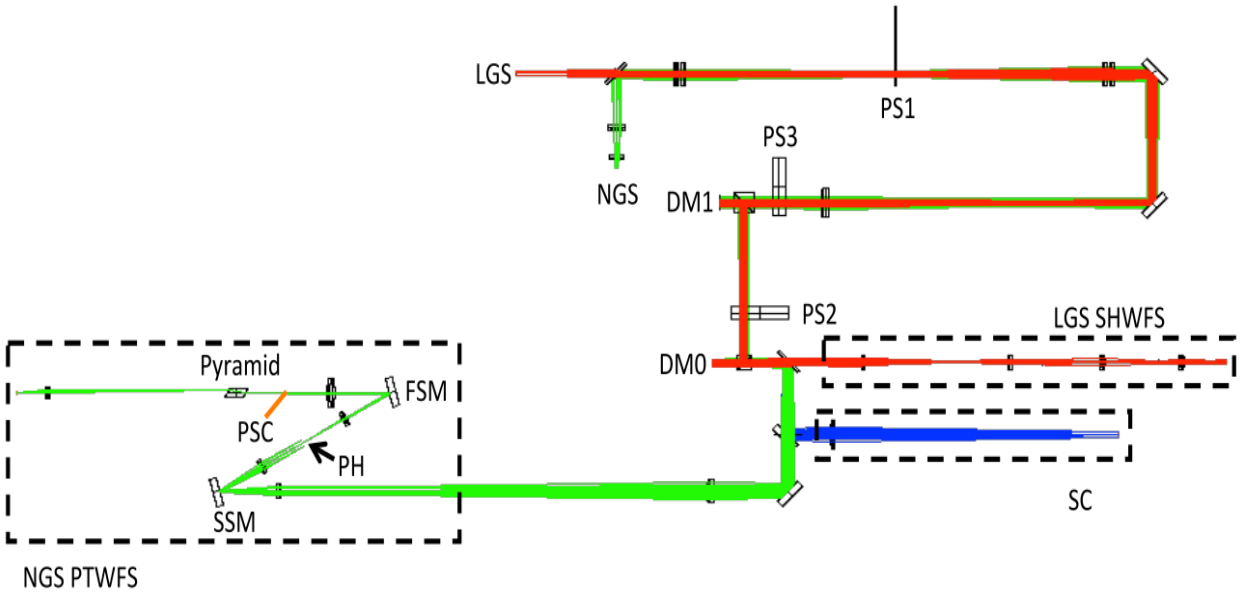

Figure 3.1: The optical design of the HeNOS bench. HeNOS includes four LGSs in a 2 by 2 configuration, a grid of NGSs, two DMs conjugated to 0 and 123 km (see Table 3.2), three-phase screens (PSs) conjugated to 0.6, 5.2, and 16.3 km, one SHWFS (red) simultaneously measuring four LGSs, one science camera (SC) (blue), and one truth WFS made with a double pyramid (green). To calibrate the pyramid WFS performance, one more science camera focused on the NGS that will fall on the tip of the pyramid, called the pyramid science camera (PSC) (orange), is also added. Figure adapted from (Mieda et al., 2018)

are shown in Table 3.2. Figure 3.1 shows the optical design of HeNOS.

3.3 Natural Guide Star Simulator

To simulate NGSs, HeNOS uses an MLA uniformly illuminated by a laser diode. The MLA creates a grid of diffraction-limited images at its focal plane. These PSFs are needed to evaluate the AO performance across the entire science field. However, when these images from the MLA propagate along the optical path of HeNOS arrive at the pupil plane, a distorted intensity grid pattern is observed due to overlapping PSFs (see *Fig. 3.2b*). This affects the images, but has caused the most serious problem in the pyramid WFS (which measures phase by comparing the intensity patterns of four pupil images created by the optical pyramid. It was speculated by Mieda et al. (2018) that this grid pattern is likely due to the transmittance and scattering of light from intermediate gaps between the lenslets. In this work, we designed an experiment to test this hypothesis and perform analysis to

Name	Abbrv	Unit	NFIRAOS
Telescope Diameter	D_N	[m]	30
DM actuator pitch	d_N	[m]	0.5
Imaging wavelength	λ_N	[μm]	1.6
DM altitudes	$h_{DM,N}$	[km]	[0, 11.2]
Fried parameter	$r_0(0.5\mu\text{m})$	[m]	0.186
Turbulence layer altitudes	h_N	[km]	[0, 0.5, 1, 2, 4, 8, 16]
Turbulence layer weights	w_N		[0.4557, 0.1295, 0.0442, 0.0506, 0.1167, 0.0926, 0.1107]
Fried parameter at observing wavelength	$r_{0,N}(\lambda_N)$	[m]	0.75
Anisoplantic angle	$\theta_{0,N}(\lambda_N)$	[arcsec]	9.4
Anisoplantic angle	$\theta_{2,N}(\lambda_N)$	[arcsec]	34.6

Table 3.1: NFIRAOS parameters

Name	Abbrv	Unit	HeNOS
Telescope Diameter	D_H	[m]	8
DM actuator pitch	d_H	[m]	0.89
Imaging wavelength	λ_H	[μm]	0.67
DM altitudes	$h_{DM,H}$	[km]	[0, 123]
Scaling factor	f_s	–	11
Fried parameter at observing wavelength after applying f_s	$r_{0,H}(\lambda_H)$	[m]	0.751
Anisoplantic angle	$\theta_{0,H}(\lambda_H)$	[arcsec]	0.751

Table 3.2: HeNOS parameters

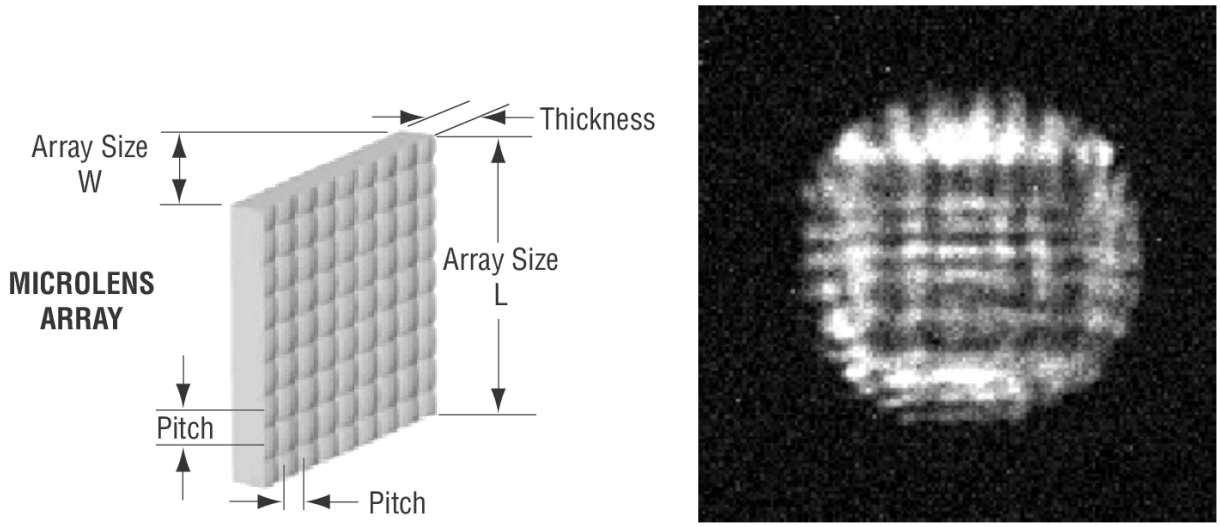

(a) (b)

Figure 3.2: (a) Representation of a square MLA currently in use on the HeNOS bench. (b) Artifact grid pattern observed on the pupil image of HeNOS presumably due to the MLA. Figure adapted from (Mieda et al., 2018).

mitigate this problem.

3.4 Experimental setup

To understand and mitigate the intensity grid pattern seen in the pupil image, we designed a simple experiment which uses a set of lenses to illuminate the MLA to create a grid of point sources. We then isolate a single spot and image its pupil on a detector. To test if the light transmitted through the intermediate gap between the lenslet contributes to the overlapping of PSFs or grid pattern, we experimented with two different MLAs: the MLA from the HeNOS bench with square lenslets (see 3.2a and a pitch of 300 μm ($f_L = 5.11$ mm), and a second MLA with round lenslets and a pitch 150 μm ($f_L = 4.1$ mm) with intermediate gaps between lenslet covered with a chrome mask to block light from transmitting and scattering through the edges of the MLA. The reason for choosing this MLA with a chrome mask of different pitch was because it is an off-the shelf component which we could use to test the hypothesis that the grid pattern in the pupil image was due to scattering in the MLA. A standard single mode fiber fed by a laser diode [4] from thorlabs served as the light source ($\lambda = 0.677\mu$m). We used two different cameras for our tests: the FLIR grasshopper 2 megapixel (MP) CCD camera[5] and the Andor Zyla 4.2 MP sCMOS[6]. Two cameras were used in this test because the same FLIR camera is currently in use on HeNOS bench so we could reproduced the results of (Mieda et al., 2018) while the Andor camera is a more sensitive, high-quality camera free of artifacts which may confuse our results from the FLIR camera. Figure 3.3 shows the experimental setup and its working principle.

3.5 Results and discussion

In Figure 3.4, the focal plane image of both MLAs are shown. It appeared both produce sharp spots at their focal plane without any artifacts whether or not the MLA has a mask. Note that the MLA with the chrome mask did offer an advantage when a Talbot plane is imaged (see Section 3.5.2). There are two potential sources for the artifacts we observed in the pupil image that we discuss below.

[4] https://www.thorlabs.com/thorproduct.cfm?partnumber=LPS-675-FC
[5] https://www.flir.ca/products/grasshopper2-gige/
[6] https://andor.oxinst.com/products/scmos-camera-series/zyla-4-2-scmos

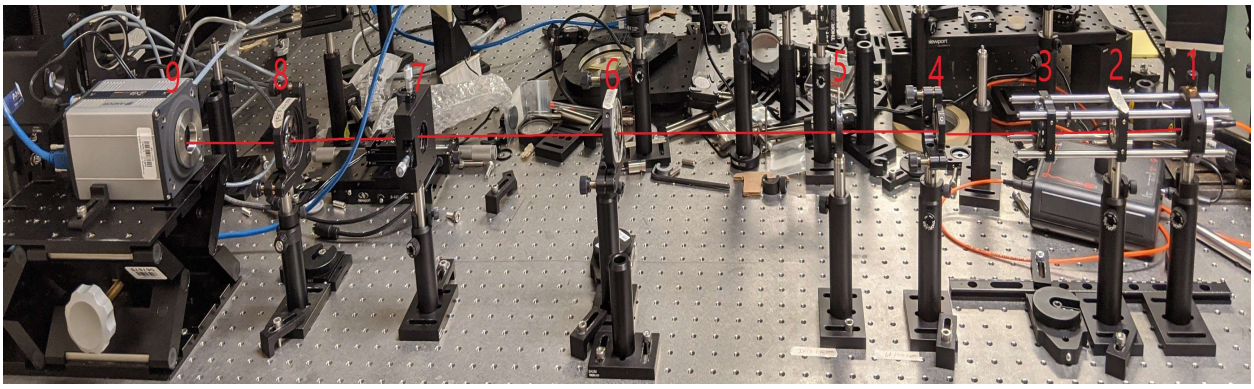

Figure 3.3: Experimental set up: A laser diode (1) beam is collimated using collimator lens (2)(f_1=80 mm) which uniformly illuminates the MLA (3) creating a grid of diffraction limited foci at its focal plane (f_L). This grid of foci is re-imaged using a lens (4) (f_2 = 100 mm) to create a pupil plane image at focus of the lens where an iris (5) is placed to limit the aperture. The pupil plane contains a grid of collimated beams that are focused by another lens(6) (f_3 = 250 mm) where a pinhole (7) (ϕ = 100μm or 200 μm depending on MLA) is placed to isolate the single spot and re-imaged at the focus of third lens (8) (f_3 = 150 mm) where a camera (9) is placed to record observations.

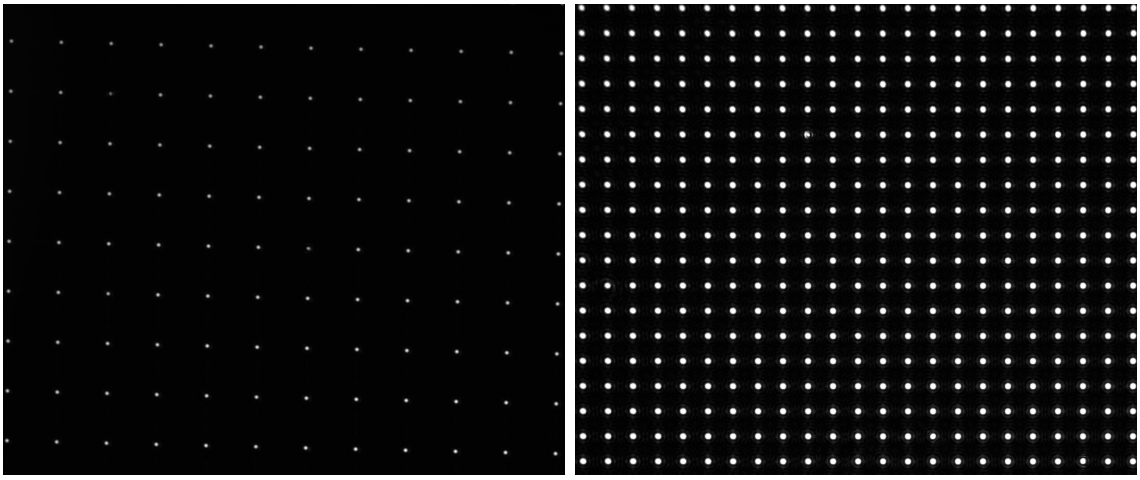

(a) (b)

Figure 3.4: Focal plane images MLA seen by camera at the position of pinhole (see fig.3.3) (a) For MLA with 300 μm pitch. (b) Same for the MLA with 150 μm. Note, it was relatively challenging to align the optical system to obtain the sharp image of MLA with 150 μm and it may not be the sharpest image possible.

(a) (b)

Figure 3.5: Pupil image created from a single, isolated point source of the MLA with 300 μm pitch (a) with FLIR camera which has two glass plate before the CCD. Incoming rays reflecting between the surfaces of glass plate interfere (b) the Andor camera has an entrance window with an AR coating and does not show any interference.

3.5.1 Artifacts due to interference from the camera window

The HeNOS bench uses a FLIR grasshopper 2 camera which has two glass plates before the CCD with no anti-reflection coating. Incoming rays will reflect between these two glass plates creating an interference pattern. We observed this interference effect in all pupil images taken with the FLIR camera but when we recorded images with the Andor camera that has a single entrance window with an anti-reflection coating, this effect was was not seen (Fig. 3.5).

3.5.2 Distortion due to Talbot effect

We hypothesize that a second source of artifacts in the pupil images observed on the HeNOS bench could be due to the Talbot effect. A micro-lenslet array is a 2D grid of small lenslets with a fixed periodicity or pitch along both axis (see Fig. 3.2a). When it is uniformly illuminated it creates a grid of diffraction-limited spots at the focal plane. This grid of spots interfere with each other as they propagate along the optical axis, creating different planes of spots with variable intensity and pitch. This phenomena is called Talbot

effect and these planes are referred to as Talbot planes (Lohmann & Silva, 1971). The Talbot effect is commonly observed for periodic structures such as diffraction gratings and MLAs (Besold & Lindlein, 1997). The pattern at the focal plane repeats itself at a distance Z_T. This distance is referred as The Talbot length and is given as

$$Z_T = \frac{2a^2}{\lambda}$$

Where a is the pitch of the MLA and λ is the wavelength of the light source. This relationship is valid when the pitch of MLA $a \gg \lambda$. In our case we have $\lambda = 0.677\,\mu m$ and $a = 300\,\mu m$ giving $Z_T \approx 267$ mm. The focal plane of the MLA is referred as the 0^{th} Talbot plane and the position of its first recurrence is called the 1^{st} Talbot plane and so on. In the fractional Talbot planes grid patterns have different pitches and are out phase comparing to focal plane. The intensity and consequently their pitches depends on the fraction of Z_T they are away from the focal plane. So, for a plane with a distance $Z = \frac{M}{N} Z_T$ from the focal plane (Where M, N are positive Integers) the number of spots per row (or column) is multiplied by a factor N for odd N and by a factor N/2 for even N so that the effective pitch between the multiplied spots is reduced by the same factor (see fig. 3.6). The sharpness of the spots decreases and intensity variation increases in higher order and fractional Talbot plane due to finite the lenslet size and walk-off effect (see Besold & Lindlein (1997)).

Talbot planes can be observed and distinguished from the focal plane by moving the MLA array along the optical axis and observing the changes on the camera but can be very challenging to distinguish in a more complex optical system like HeNOS which requires isolating a single spot for the pupil viewing Pyramid WFS. Moreover, Besold & Lindlein (1997) also found in their numerical simulations that fractional Talbot plane of a MLA with a mask blocking the light transmission between the lenslet shows less intensity variation comparing to a MLA with no mask (see *Fig. 3.7*).

So if the NGS selected for use for the pyramid WFS (filtered by a pinole) is in reality a spot created at a fractional Talbot plane, which could be quite likely, the isolated single spot used for pyramid WFS is actually formed from the light of multiple lenslets interfering through preceding Talbot planes. Therefore, we expect that the "pupil" image of a Talbot spot would manifest more intensity variation (Fig. 3.8). While we did observe a complicated interference pattern when imaging the pupil of a Talbot spot, we were not able to reproduce the exact features of the pupil image observed on the HeNOS bench. While these results are

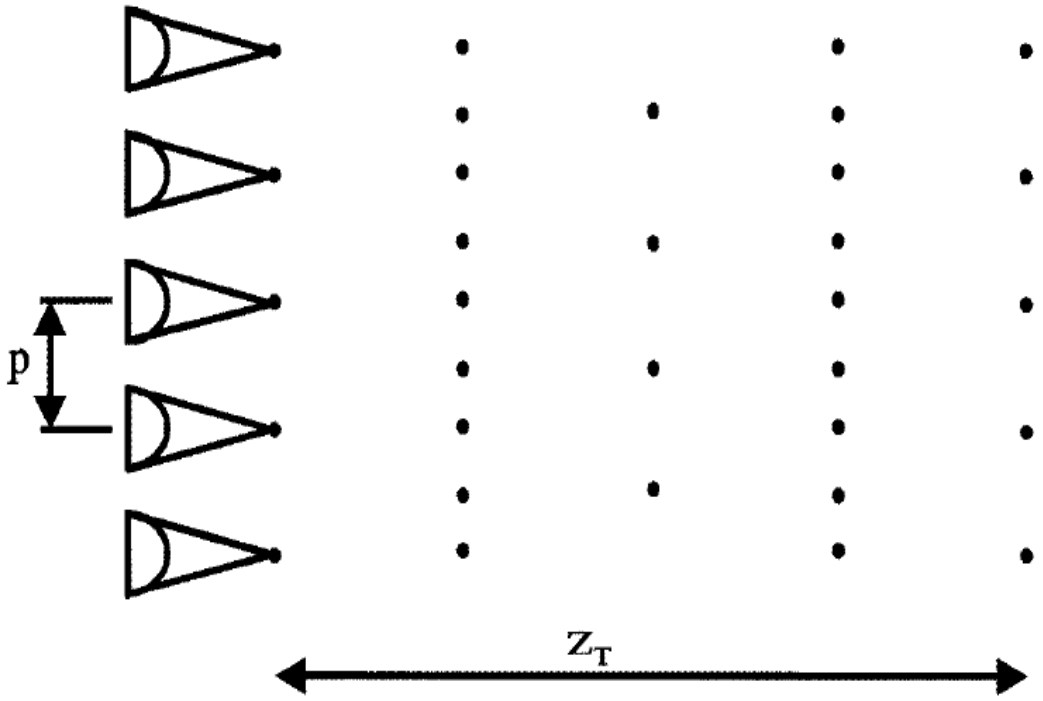

Figure 3.6: Talbot effect created by an MLA. In fractional talbot planes $\frac{1}{4}$ and $\frac{3}{4}$, the pitch has doubled whereas in the $\frac{1}{2}$ Talbot plane pitch is the same as focal plane but spots are laterally shifted by half a pitch. Figure adapted from Besold & Lindlein (1997).

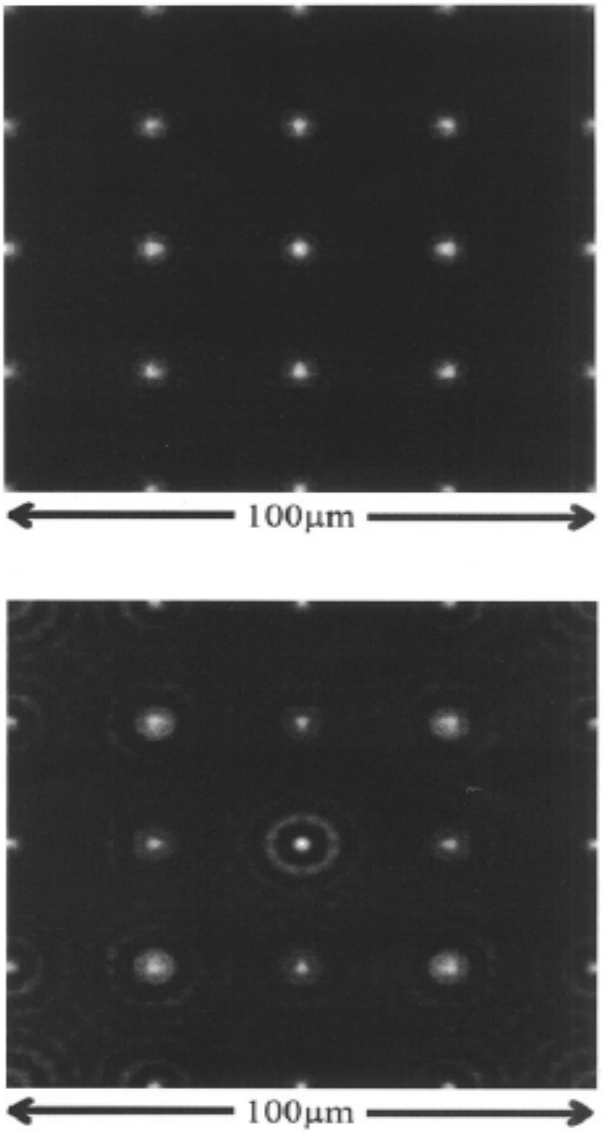

Figure 3.7: Simulation of the foci of a refractive MLA with pitch = 100 μm and lenslet diameter = 80 μm in the $\frac{1}{8}$ Talbot plane. Shown is one period of the array with 4 Ã— 4 multiplied foci. In top panel there are stops between the lenses whereas in the lower panel there are no stops between the lenses. Figure adapted from Besold & Lindlein (1997).

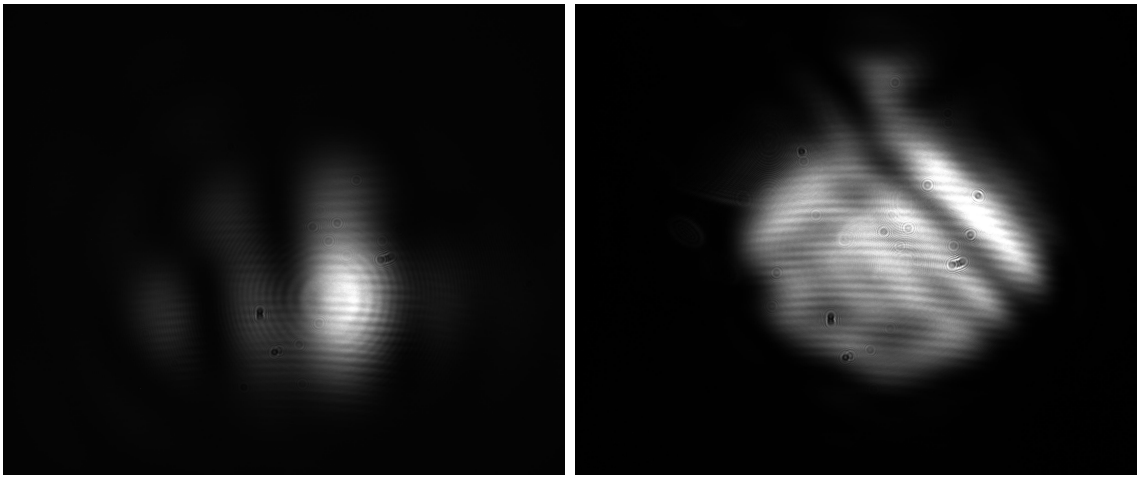

(a) (b)

Figure 3.8: (a) Distortion due to Talbot effect in pupil image when a single spot is imaged for MLA with 300 μm pitch (b) This image was taken when setup was not aligned so it's likely a combination of misalignment and a fractional Talbot plane. Its looks very similar to what Mieda et al. (2018) observed earlier (*see Fig. 3.2b*).

preliminary and derived from a rather simple optical system comparing to HeNOS, we are hopeful we can fix the pupil image problem on HeNOS by ensuring we are not selecting the pyramid NGS in a Talbot plane.

3.6 Summary

We constructed an imaging test setup and objectively analyzed the aberrations observed when using a uniformly illuminated MLA to simulate NGSs. The overlapping intensity grid pattern observed on HeNOS is suspected to arise from a combination of artifacts introduced by the FLIR camera and the Talbot effect. To address this, future measurements on the bench will utilize the Andor camera, which offers improved performance. Based on our observations, we recommend using a focal plane mask in place of a lenslet array, as it may more effectively mitigate ghost imaging associated with the Talbot effect.

Chapter 4

The Keck Precision Calibration Unit (PCU)

The work described in this section has been published in the SPIE proceeding under the title Design of a Precision Calibration Unit for Keck NIRC2 AO instrument (Zeren Lin, Tarun Kumar, Xun Chen, Jessica Lu, Peter Wizinowich, Scott Lilley, Ed Wetherell, Nicholas McConnell) is reproduced here with additional updates. For details refer to Lin et al. (2020). In this project, I led the instrument's design, sourcing of the stages, ensured compliance with all required specifications and helped in writing the manuscript for this article.

4.1 Introduction

High-precision astrometry has been a powerful technique in astrophysics. Combined with diffraction-limited imaging and integral-field spectroscopy on 8-10 m class telescopes, it enables a wide range of science cases, including detecting and studying exoplanets (Marois et al., 2008; Lagrange et al., 2009; Rameau et al., 2013), studying the environments and fundamental physics of supermassive black holes (Ghez et al., 2008; Lu et al., 2008; Gillessen et al., 2012; Do et al., 2019), resolving individual stars in the central regions of the Local Group galaxies (Stephens & Frogel, 2002; Davidge et al., 2000; Davidge, 2001), and searching for stellar-mass black holes using astrometric microlensing (Gould & Yee, 2014; Lu et al., 2016b). The near-infrared camera, NIRC2 (PI: Keith. Matthews), on the W. M. Keck II telescope has been essential for a large number of these studies thanks to its stable and

precise astrometry, yielding a positional uncertainties as low as 0.15 mas (Yelda et al., 2010).

Two factors that currently limit the accuracy of precision astrometry are (1) differential atmospheric refraction mainly consisting of an achromatic term with a correction error of ~ 1 mas under most conditions and ~ 2 μas for crowded fields (Schöck et al., 2014; Trippe et al., 2010), and a chromatic (dispersion) term with a correction error of ~ 15 μas (Schöck et al., 2014), and (2) knowledge of the static component of the AO camera's geometrical distortions with a nonlinear residual of $\sim$ 1 mas for Keck NIRC2 (Yelda et al., 2010; Lu et al., 2016a) for the specific Galactic Center science. The latter, if not properly accounted for, will compromise the astrometry precision by a factor of $10-100\times$ (Service et al., 2019b) and thus must be measured and corrected for each instrument.

4.1.1 State-of-the-Art of Geometric Distortion Calibration Methods

Geometric distortions in NIRC2 were initially characterized using internal fine mask grids (43×43, 8 μm-sized, 7 mm separation pinholes; and 21×21, 4 μm-sized, 3.5 mm separation pinholes) illuminated at single mask positions and fitted to a $\mathcal{O}(3)$ distortion model [1] (Cameron & Kulkarni, 2007). They were later replaced by on-sky measurements utilizing known catalogs, e.g. globular clusters data from the HST (Yelda et al., 2010; Lu et al., 2016a) as external distortion-free references. The two approaches are both limited by the degree of systematic errors in the reference positions: either the pinhole position errors or the intrinsic residual errors in the referenced catalogs. Currently, the on-sky data is more accurate ($\sim$ 1 mas (Yelda et al., 2010; Lu et al., 2016a)) than the solutions from mask grids ($2-3$ mas (Cameron & Kulkarni, 2007)), but requires significant on-sky time ($>$ 1 night and at least once per year if not more frequently).

On the other hand, the best distortion calibrations for astronomical instruments to-date use a technique called 'self-calibration' which has been widely implemented for non-astronomical imaging systems (Faugeras et al., 1992; Hartley, 1993; Pollefeys & Van Gool, 1997; Heyden & Astrom, 1996). Its basic idea is that the intrinsic optical properties (static with respect to the camera's frame) could be separated from other extrinsic effects comoving with the camera through a series of camera motions. In the case of on-sky self-calibrations, the intrinsic term is the static optical distortions of the imaging system, and the extrinsic

[1] https://www2.keck.hawaii.edu/inst/nirc2/astrometry/distortion.pdf

term is the on-sky positions of each star. The camera motion is achieved through translating and rotating the pointing of the telescope multiple times to constrain all possible distortion modes across the field of view. Using this method, the static distortion in HST Advanced Camera for Surveys Wide Field Channel (ACS/WFC) has been corrected down to the ~ 0.01 pixel (~ 0.5 mas) level (Anderson & King, 2006; Anderson, 2007). Similarly, an advanced on-sky self-calibration method including time variation was used for Gaia Data Release 2 (DR2) and achieved an astrometry accuracy of < 0.04 mas for their brightest sources (Bernard et al., 2018; Lindegren et al., 2018).

4.1.2 Self-Calibration Methods using Photo-Lithographic Mask Grids

The same self-calibration methods could also be applied to finding the distortion solution using internal mask grids. Instead of translating and rotating the telescope pointings as in on-sky self-calibrations, only the mask grids need to be translated and rotated. This significantly reduces the complexities of operations and more importantly, could be done during the day thus saving expensive night-time calibrations. One drawback of using internal masks is that it is blind to telescope distortions, which fortunately contributes to only 1/10000 of the distortion in the AO relay (Patti & Fiorentino, 2019).

Another crucial factor enabling the self-calibration methods with mask grids is the progress of photo-lithography technologies. Of particular relevance is the overlay accuracy which directly translates to mask grid irregularities and distortion residuals if the mask is not pre-calibrated. The overlay accuracy has improved from ~ 50 nm in 2000 (Allan et al., 2002) to a value of ~ 3 nm in 2019 (Neisser & Wurm, 2013; Neisser et al., 2018). Service et al. (2019b) have characterised a commercial mask grid (86×86, 56 μm-sized, 1 mm separation pinholes) and performed lab experiments demonstrating the self-calibration methods with the mask grid. In their modeling, the mask motions (translation + rotation) are accounted by linear transformations and the optical distortions by $\mathcal{O}(2-6)$ polynomials. After solving the model self-consistently, they achieved final residuals of: (1) 47.2 ± 4.5 (random) $\pm$ 11 (systematic) nm for non-linear mask distortions (mask irregularities), (2) and 37.8 nm for higher-order $\mathcal{O}(> 6)$ optical distortions over the field of view of 1788 mm^2. The 47.2 nm intrinsic residual of mask distortions set the systematic precision when the mask is used at a single mask position, which corresponds to 0.13 mas for Keck NIRC2. When the mask distortions are pre-calibrated, the 37.8 nm (0.1 mas) optical distortion residual is ~ 10 times

improved over the current $1-2$ mas values for Keck NIRC2 (Section 4.1.1), and could be mitigated using a model including higher-order distortions. Similar method could be applied to future 30 m class telescopes with an astrometry accuracy of $\sim 20-30$ μas.

Inspired by their results, we present a detailed realization of such a calibration unit using photo-lithographic pinhole masks. We describe the top-level requirements in Section 4.2 drawn from the findings of the experiments, Section 4.3 discuss the instrument design as well as critical steps towards a full translation & rotation degrees of freedom of the pinhole mask. Additional engineering challenges arose from accommodating current & future projects, which set requirements on the allowable weight, torque and thermal performance are discussed in Section 4.4 and efforts to satisfy those requirements in the preliminary design phase. Section 4.5 discuss the future work past PDR when our involvement in the project concluded and the path forward to build, test and deliver our proposed calibration units in 2021. A summary of the project up to the final design review (FDR) is provided in Section 4.6.

4.2 Requirements

The major challenge for solving a self-calibration model as described in Service et al. (2019a) is the significant degeneracy between the fit parameters. Not only multiple solutions to the optical distortion model could exist, but also multiple combinations of mask and optical distortions could fit the data equally well. Service et al. (2019a) performed a series of simulations to estimate the effectiveness of their model under various conditions. Their key findings are summarized below:

(i) Only rotating the mask will underestimate radial modes of the mask & optical distortions that cancel each other. Only translating the mask will lead to 95 % of the mask distortion misidentified as optical distortion. An accurate self-consistent solution is achieved when the mask is able to rotate 360 degrees continuously and translate ~ 15 % of the camera FOV.

(ii) The degeneracy between mask & optical distortions are very sensitive to scale-variations. Therefore, stable scales for each mask position are required to disentangle the two. Possible factors that affect the scale, such as inaccuracies of movements along the optical-axis, and mask deformation by flexures, should be minimized.

(iii) Ordered (correlated) mask distortions are significantly more difficult to separate from

Part	Topic	Requirement	Rationale
Pinhole mask	FOV	$\geq$ 40" x 40"	NIRC2 wide field camera
	Mask pattern size	$\geq$ 41 x 41 mm^2	FOV to size in the focal plane
	Mask size	$\geq$ 61 x 61 mm^2	Manufacturer requirements
	Pinhole array pattern	$\geq$ 10 x 10	Sufficient for $\mathcal{O}(6)$ distortion model
	Pinhole size	$\geq$ 43 μm	SNR $\geq$ 600 within 120s exposure
X-/Y-stages	Precision & repeatability	$\leq$ 5 μm	Stability of single-mode fibers
	Travel range X-stage	$\geq$ 276 mm	Compatible with other projects
	Speed X-stage	$>$ 8 mm/s	Acquisition time
	Travel range Y-stage	$\geq$ 140 mm	Optical axis height
Z-stages	Precision & repeatability	$\leq$ 50 μm	$\sim$ 10^{-4} scale-variation, Section 4.2 (ii)
	Travel range	$\geq$ 95.5 mm	Distance to the focal plane
Rotation stage	Range	$\geq 360^\circ$	Section 4.2
	Clear aperture	$\geq$ 41 mm	To cover the NIRC2 FOV
	Angular repeatability	$< 0.5^\circ$	Set by other project
	Rotation speed	$> 45^\circ$/s	Set by other project
	Working temperature	0 $\pm$15°C	Bench requirement

Table 4.1: Top-level requirements

and could easily alias into optical distortions. Therefore, any effect that flexes the mask with spatial correlations (choice of mount, temperature, manufacturing process) should be mitigated.

(iv) Environmental instability in a non-linear fashion will contribute to the distortion residual and should be avoided. Those include but are not limited to a changing temperature gradient and/or vibrations on the mask.

Therefore, to alleviate the degeneracy problem, we list a set of top-level requirements for PCU in Table 4.1. The optical axis is denoted as Z, and the gravity direction as Y. We emphasize that even though some of the requirements are specific to NIRC2 and OSIRIS (e.g., the precision and repeatability of translation stages) to be compatible with other projects, most of them are derived from (i)-(iv) above. In particular, a rotation stage with high precision is not necessary since the positioning errors are included in the first order term for the mask motions. Moreover, we require the PCU to work in the temperature range of 0 ± 15°C to meet the requirements set by Keck team to meet the future plan to put the AO bench under 15°C temperature.

4.3 Instrument design

A key challenge in this project has been to find compact stages with high precision that can fit into the tight spatial requirements. The PCU assembly also needed to be compatible as well as host components from other projects. Figure 4.1 shows the current AO bench of Keck 2 telescope where PCU will be mounted. In Figure 4.2 a computer aided design (CAD) rendered model of the instrument is shown and how the instrument will work. The project passed its PDR phase in October 2020 (Lin et al., 2020). Table 4.2 shows the status of the project and relevant technical specifications of the selected stages when the PDR was completed.

The core of the PCU functionalities is to freely translate and rotate the pinhole mask at the first focal plane of the telescope (Figure 4.1). It utilizes the dome light in the H and K bands to illuminate the mask. For 56 μm-sized pinholes as discussed in Service et al. (2019b), or equivalently FWHM of ~ 60 mas, a single exposure of 30 sec will produce SNR = 600 pinhole images on the NIRC2 narrow field camera (OSIRIS imager camera). A set of images will be taken at various mask positions to decouple the static optical distortion from other effects, achieving an expected distortion residual of ≤ 0.1 mas. As part of the AO bench upgrades, the PCU will replace the Simulator Fiber Positioner stages (SFP-XYZ) at the entrance and provide support for a few existing and new modules:

(i) A clear aperture of ~ 110 mm for night observations.
(ii) A pathway to fold the telescope simulator beam to the AO system.
(iii) Holding a translatable and rotatable pinhole mask at the first focal plane.
(iv) Transporting the Keck All sky Precision Adaptive Optics (KAPA) fibers to the first focal plane.
(v) Feeding the Keck Planet Finder (KPF) fiber injection unit (FIU).
(vi) Holding a few swappable waveplates for polarimetry science along the optical axis.

All the above top-level requirements are satisfied in our preliminary design (Figure 4.2). The main opto-mechanical components are five translation/rotation stages from Physik Instrumente (PI): X-/Y- and two Z-stages, plus one rotation stage. Their compliances with respect to the design requirements are summarized in Table 4.2. The delivery of each module to their proposed locations as well as dithering/rotating the pinhole mask are fulfilled through stage movements labeled by (x, y, z_1, z_2, θ) (Table 4.3).

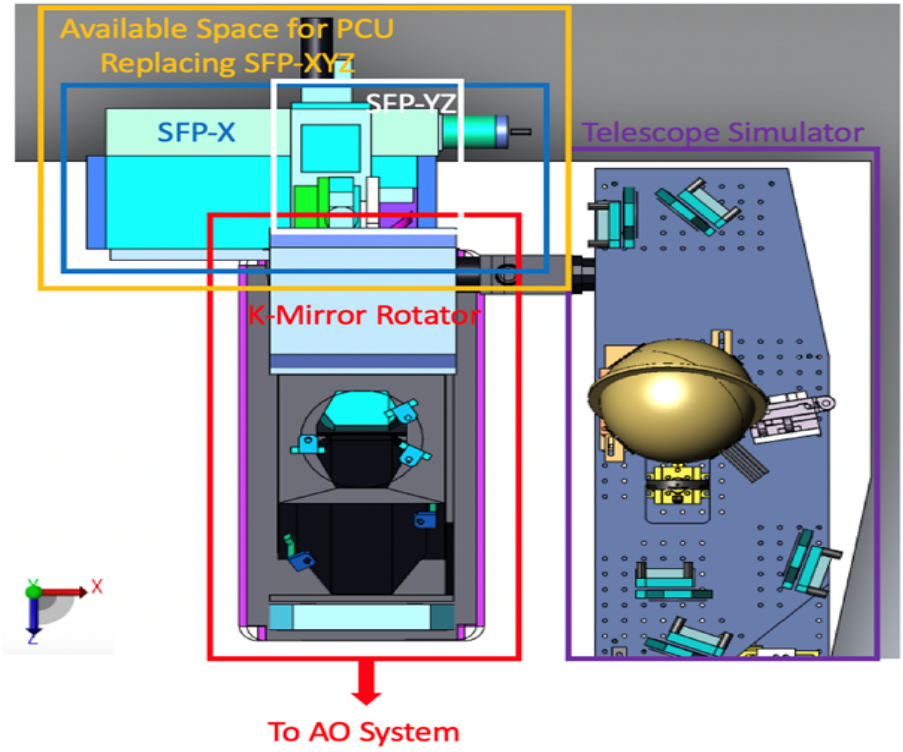

Figure 4.1: Location of the new PCU relative to the other components on the Keck 2 AO bench. The SFP unit will be replaced by the PCU instrument.

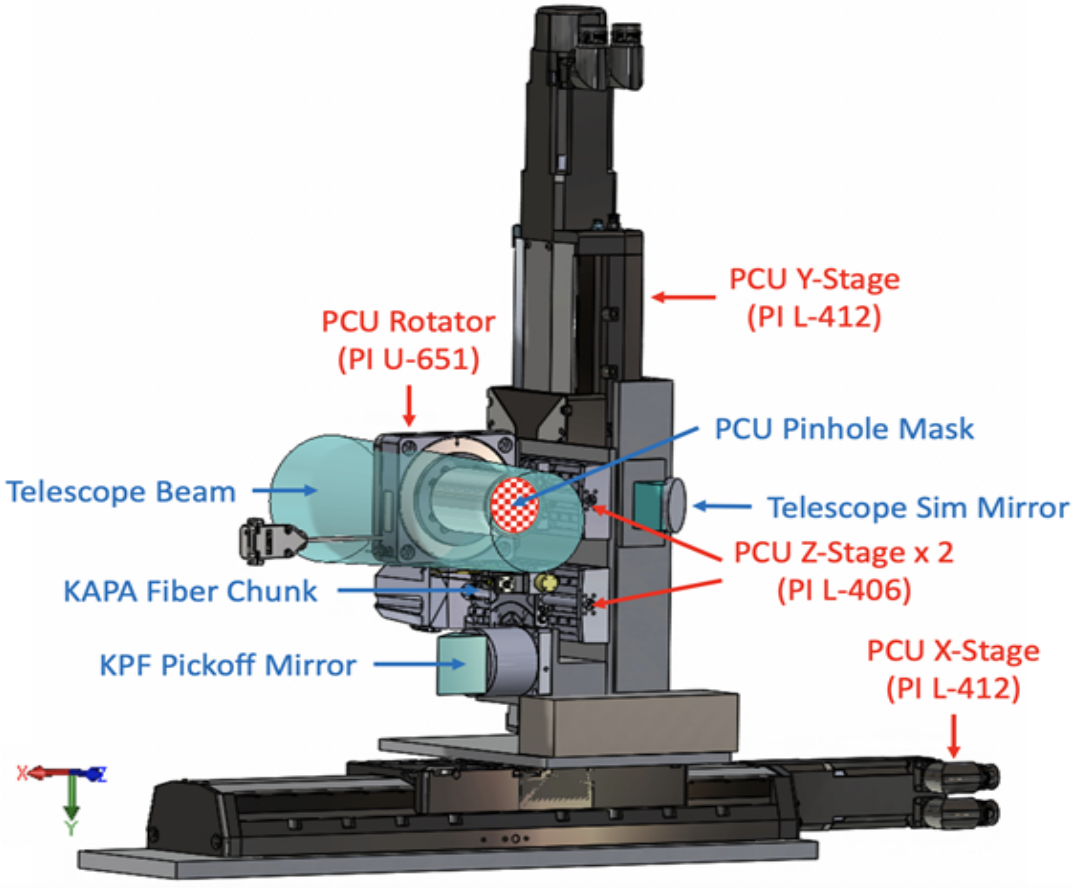

Figure 4.2: CAD rendering of the design showing different components of the instrument. Light comes from the telescope, passes through the first focus, and into a field de-rotator K-mirror (see *Fig. 4.1*). The focal point is slightly inside the K-mirror housing. The PCU can be slid into place in one of 4 positions: (1) a pinhole mask can be illuminated with dome light, (2) fiber sources can be positioned to simulate guide stars and science objects (with the AO hatch closed), (3) a fold mirror can be positioned to bring in light from the telescope simulator, (4) a fold mirror can accept light from the telescope and sends it to the KPF fiber injection unit. The PCU can also be slid out of the way for other modules, and for night time AO operations. In parenthesis shows the selected stage code name from Physik Instrumente (PI).

Part	Topic	Requirement	PDR status
Pinhole mask	FOV	$\geq$ 40" x 40"	under review
	Mask pattern size	$\geq$ 41 x 41 mm^2	,,
	Mask size	$\geq$ 61 x 61 mm^2	,,
	Pinhole array pattern	$\geq$ 10 x 10	,,
	Pinhole size	$\geq$ 43 μm	12, 24, 56, 120 μm
X-/Y-stages	Precision & repeatability	$\leq$ 5 μm	$\pm$1 μm
	Travel range X-stage	$\geq$ 276 mm	305 mm
	Travel range Y-stage	$\geq$ 140 mm	204 mm
	Speed X-stage	$>$ 8 mm/s	300 mm/s (max)
Z-stages	Precision & repeatability	$\leq$ 50 μm	$\pm$5 μm
	Travel range	$\geq$ 95.5 mm	102 mm
Rotation stage	Range	$\geq$ 360°	$\geq$ 360°
	Clear aperture	$\geq$ 41 mm	53 mm
	Angular repeatability	$<$ 0.5°	$\pm$0.003°
	Rotation speed	$>$ 45°/s	540°/s (max)
	Working temperature	0 $\pm$15°C	5-40° (specified) -30° (conditional)

Table 4.2: PDR status of the project

Position	x (mm)	y (mm)	z_1 (mm)	z_2 (mm)	θ
Telescope simulator	0	140	0	0	
Pinhole mask	-173.4	0	95.5	0	$0 - 360°$
Waveplates	-173.4	0	0	0	$0 - 360°$
KAPA fibers	-173.4	69	0	95.5	
KPF FIU	-193.7	140	0	0	
Telescope beam	-276	140	0	0	

Table 4.3: Proposed stage movements.

4.4 Engineering Challenges

We highlight here a few requirements that were particularly challenging to meet, which should be addressed in future calibration units of a similar kind.

Weight & Torque Budget: One of the major complexities of the current design is the multiple stages and their various orientations in all three axes: the pinhole mask is mounted on a $\sim$ 100 mm-length tube on the rotation stage, providing access to the first focal plane inside the K-mirror housing. The two Z-stages and the KPF fold mirror are mounted on the vertical Y-stage. Moreover, the Y-/Z-stages need to be placed away from the X-stage's center of the gravity due to the limited space available on the optical bench. All those above result in a significant amount of torque on the supporting stages. Great efforts have been made to ensure the weight and torque on each stage will not exceed their specified limits. In particular, (1) we deliberately chose a heavier Y-stage with a travel range larger than the required value (see Table 4.2) because of its large passive brake limit which keeps the assembly in the current state to avoid collisions in the case of sudden power outage. (2) We include the option to place a counterweight on the X-stage to further balance the torque exerted by all the other parts. We summarize the estimated weight & torque of the current design in Table 4.4.

Thermal Budget: To maintain a stable working temperature of $0 \pm 15°$C and minimize the unnecessary heat, we place all active components (for example, all motion controllers) except for the stage actuators away from the optical bench. For our current design, the primary heat source is the i^2R loss from stage motors, which is proportional to the input power and is motor dependent. Generally we prefer motors without feedback controls as our top choice. However, in the case of X-/Y-stages, we have to make the trade-off between

Stage	Mass (kg)	Torque (Nm)	Mass Limit (kg)	Torque Limit (Nm)
Rotation stage[1]	0.15–0.22	0.020–0.070	2	0.3
Pinhole Z-stage	1.60	NA	10	7.5
Y-stage[2]	6	4.40	40.8	15
X-stage[2]	14.7[3]	14.33[3]	40.8	20

[1] The mass and torque on the rotation stage will depend upon which of the two swapable modules: pinhole mask or half wave plate (another project coming on Keck 2 AO bench) is attached.
[2] The torque on the X-stage is estimated with the two Z-stages both extracting all the way back, which is the maximal torque possible during operations. Similarly, the torque on the Y-stage is estimated when the two Z-stages are inside the K-mirror housing, reaching their positive limits.
[3] Values without the counterweight.

Table 4.4: Weight & Torque estimations.

heat and other factors (permissible torque & weight for the Y-stage and motor speed of the X-stage). The risks are partially reduced by the fact that the X-/Y-stages will only be active when switching among different modules, unlike the rotation stage which needs to run continuously when calibrating the distortion. We list the input power data for all stages in our current design in Table 4.5 and leave the full thermal analysis as part of the future work.

Stage	Motor Type	Input Power	Usage	Reason of Choice
Rotation stage	Ultrasonic piezo motor	21 W (max)	Cont.	Low profile & mass
Z-stages	DC gear motor	8.5 W (max)	Interm.	As above
Y-stage	Synchronous servo motor	874 W (nom)	Interm.	Passive brake
X-stage	Synchronous servo motor	874 W (nom)	Interm.	Motor speed

Table 4.5: Selected stages and their power inputs.

4.5 Project Status

The waveplate swapping mechanism with the polarimetry project team was completed after the PDR. A few potential risks were identified at the time of PDR and were later addressed as by local ground team that are summarized below:

(i) Thermal Analysis: The impact of the heat dissipation from stages (mostly X-/Y-stages)

on the system, and to estimate the settling time needed for the heat to dissipate away after each stage movement.

(ii) Image Quality Analysis: The potential effects the telescope distortion could have on the distortion modelling proposed by Service et al. (2019b).

(iii) Flexure Analysis: The flexure on several critical parts: pinhole mask mount, interface plates, etc, and its potential effects on the stability of PCU and the distortion residuals via mask deformations.

(iv) Vibration Analysis: The potential risks from vibrations, especially whether the PCU is prone to certain resonant frequencies.

(v) Safety: Implement a multiple-level safety control scheme, including software & electric control and hard stops to avoid collisions of stages during mis-operations of movements.

4.6 Summary

The goal of the Keck PCU project was to design, build and deliver two PCUs for both NIRC2 and OSIRIS instruments behind Keck AO. As an upgrade of the current on-sky distortion calibration method, the two new units each contain a pinhole mask that can be used to calibrate distortion solutions during the day, saving the expensive on-sky time (~ 1 night per time and > 1 time per year), and will provide an order-of-magnitude improvement over the current calibration precision. The project was initiated in December, 2018 as a mini-project at the TMT early career initiative (TECI) workshop. The initial design was developed by TECI participants in 2018-2019 and was then matured as the team expanded to include Keck engineers in 2020. The project successfully completed its PDR in October 2020 and its FDR in January 2021 without any changes. Our involvement concluded following the FDR due to travel restrictions imposed by COVID-19, and the project was subsequently managed by the local team. The final procurement, assembly, and installation was completed in 2021 (See Fig. 4.3). The instrument was successfully commissioned in 2022 [2] (Surendran et al., 2022). Currently, the required pipelines for daytime calibration are in the development phase (Wizinowich et al., 2024).

[2]https://ar5iv.labs.arxiv.org/html/2207.14433

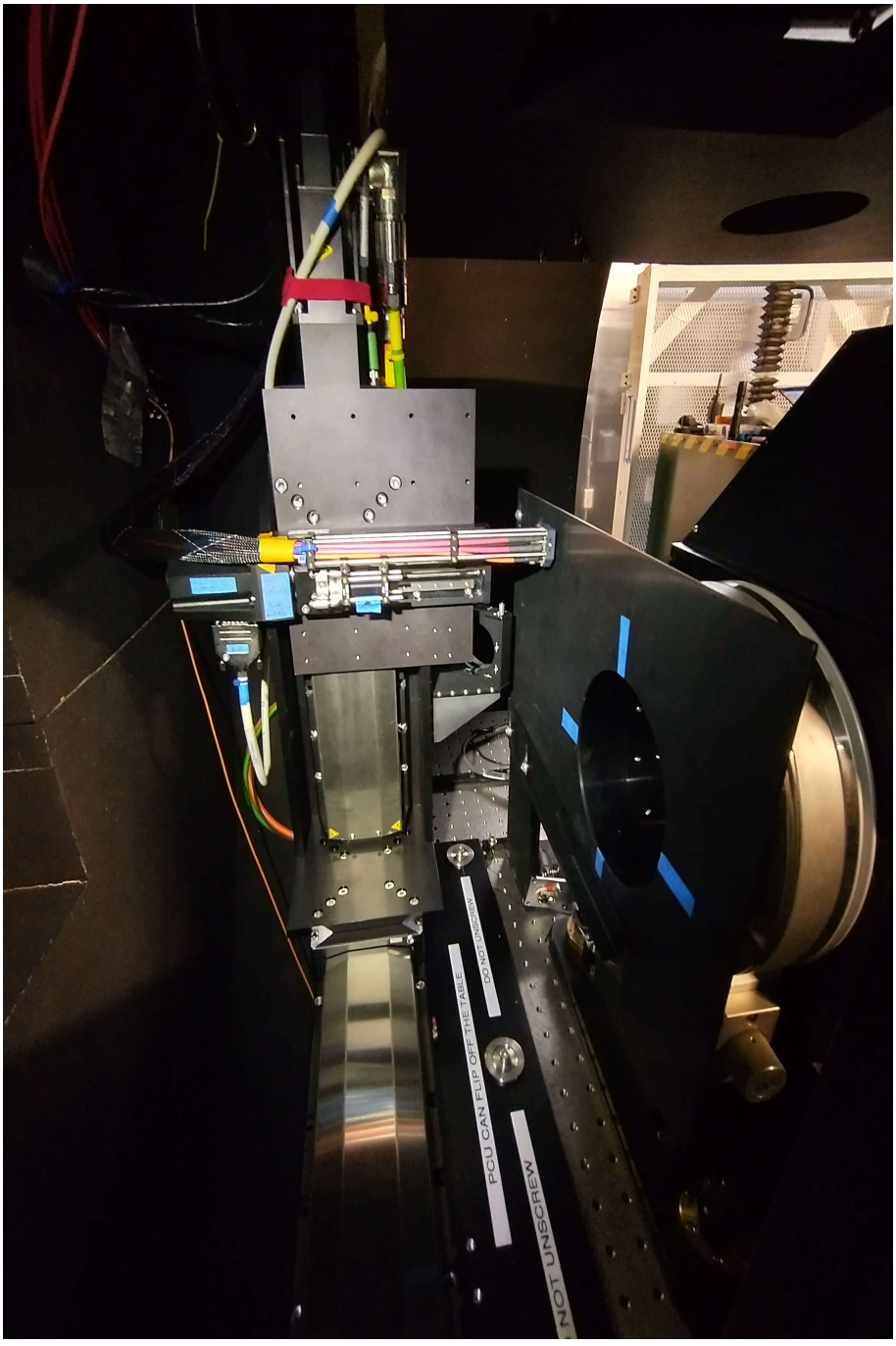

Figure 4.3: The PCU installed on the Keck I AO bench. The fibre bundle is mounted. The opening to the K-rotator is on the right, marked with blue tape.

Chapter 5

Performance analysis of REVOLT

The work described in this section has been published in the SPIE proceeding under the title Performance analysis of REVOLT from laboratory and on-sky tests (Kumar, Tarun ; Andersen, David; Jackson, Kathryn ; van Kooten, Maaike A. ; Lardiere, Olivier ; Veran, Jean-Pierre) is reproduced here as published with minor changes. For details refer to (Kumar et al., 2024b). I led the implementation and initial alignment of the REVOLT in the laboratory and developed the necessary pipelines for closed-loop operation. I collaborated closely with the HEART team – providing them with REVOLT data to fine-tune HEART for REVOLT. I participated in the observing runs, using the resulting measurements to build a comprehensive error budget. Finally, I led all aspects of the research and writing of this article.

5.1 Introduction

With the dawn of extremely large telescopes such as the E-ELT and the TMT there is a growing need to test and validate next-generation adaptive optics technologies. AO is a field driven by technological advancements, where on-sky experiments frequently serve to demonstrate new technologies and evaluate innovative modes of operation. As an example, the Multi-Conjugate Adaptive Optics Demonstrator (MAD) was built by ESO and a consortium of Italian universities to demonstrate the feasibility of MCAO and to evaluate the performance of pyramid WFS on-sky (Marchetti et al., 2003; Moretti et al., 2009). The Gemini facility MCAO system GeMS (Neichel et al., 2014a; Rigaut et al., 2014) owes a

debt to MAD. Likewise, there have been several on-sky experiments that have advanced the feasibility of future MOAO systems. The Victoria Open Loop Testbed (VOLT) (Andersen et al., 2008) and Visible Light Guidestar Experiments (ViLLaGEs) (Ammons et al., 2008) used new DM technologies and demonstrated open-loop control of the DMs on-sky. Canary at the William Herschel Telescope (Myers et al., 2008; Sivo et al., 2014) and Raven at Subaru (Andersen et al., 2012; Lardière et al., 2014) both built upon the proof of concept demonstrations of open loop control from VOLT and ViLLaGEs to demonstrate full MOAO functionality on-sky. In turn, these demonstrators help guide the design of future MOAO instruments, such as GIRMOS for Gemini Telescope, which is currently under development (Chapman et al., 2018, 2022).

REVOLT is a SCAO located on the 1.2-meter McKellar telescope at Dominion Astrophysical Observatory (DAO) (Jackson et al., 2023). The goal of the REVOLT bench is to enable on-sky testing of key AO technologies being developed by NRC Herzberg (HAA). So far, we have incorporated First Light Imaging C-Blue detector as a high-speed SHWFS. The REVOLT WFS is currently used to control a commercial ALPAO DM which will later be replaced by a new Micro-ElectroMechanical Systems (MEMS) low voltage deformable mirror (LVDM) currently being developed at the NRC Nanotechnology Research Centre in Edmonton (Ross et al., 2018). The Real-Time control (RTC) System is implemented using the HEART, which has been developed at HAA and will be used on next-generation AO systems for Gemini Observatory and the TMT (Smith et al., 2022). So far, REVOLT has enabled testing of an experimental Spectral Correlation Sensor fed by an AO corrected single mode fibre injection unit (Cheriton et al., 2022) and an open loop device to test the calibration techniques for GIRMOS (Turri et al., 2022). Recently, a new Pyramid WFS and an open loop channel were incorporated into REVOLT. As REVOLT continues to evolve it is critical to understand its baseline performance.

In this work, we present the REVOLT wavefront error budget and validate its performance using simulations. Wavefront error budgeting is an essential process in the design and optimization of AO systems. It involves identifying and quantifying various sources of wavefront error to ensure that the overall system meets performance requirements. In Section 4.3 we discuss the opto-mechanical design of REVOLT, its integration with the McKeller telescope and the HEART Real-Time Control system that drives the WFS. In Section 5.3, we discuss our REVOLT observations and calibration data. In Section 5.4, we present the performance of REVOLT AO bench. This section details the calculation of the science camera's throughput, SR computation, and the temporal performance of the WFS camera. Additionally, it discusses the comprehensive end-to-end Monte Carlo simulations conducted

for REVOLT. Finally, in Section 5.7, we present the REVOLT wavefront error budget.

5.2 REVOLT Instrument Design

5.2.1 Opto-Mechanical Design

The initial optical design of REVOLT is a relatively straightforward implementation of SCAO but was flexible enough to incorporate open loop and pyramid paths in future upgrades. Figure 5.1 shows the optical layout of the initial SCAO configuration of REVOLT. REVOLT is located in the coude room of the McKellar 1.22m telescope at the DAO in Victoria. This provides REVOLT with a gravity-invariant, temperature-stable environment. Light from the telescope's coude focus is reflected by a deployable fold mirror into the main REVOLT optical relay, which incorporates an ALPAO DM277 with 17 x 17 actuators across the pupil diameter. A dichroic beam-splitter reflects the near-infrared light to the science camera while the visible light is passed to a SHWFS. The SHWFS uses a 16 x 16 lenslet array with a 15.33" field of view in each subaperture. The SHWFS detector makes the first on-sky use of the 1.7M pixel First Light C-Blue One detector, a recently available high-speed, low-noise, scientific CMOS detector with 9 μm pixels. The C-Blue One detector operates within 400-1000 nm, but the peak quantum efficiency (QE) of $\simeq 70\%$ is achieved at 580 nm. The full dimensions of the detector are 1608 x 1104 px (Gach et al., 2022), but REVOLT only uses a 352 x 352 pixel window. By reading out only a portion of the detector, we operate the REVOLT SHWFS at a frame rate of up to 1 kHz. The infrared light reflected off the dichroic beam-splitter is imaged onto the science camera, an Allied Vision Goldeye G-008 Cool TEC1 operating in the 1000–1650 nm wavelength range. The Natural Guide Star used by the WFS also serves as the "science" target for REVOLT, as the main purpose of this SCAO science channel is to measure the PSF and provide performance benchmarks. A summary of telescope and REVOLT parameters is presented in Table 5.1.

5.2.2 HEART

REVOLT makes the first use of the HEART (Smith et al., 2022; Gamroth et al., 2022). HEART is a software framework and set of utility tools that serve as RTC for REVOLT and will be used in future NRC HAA-developed AO systems including Gemini GPI2 (Kerley

McKeller Telescope		
Diameter (D)	1.22 m	
F/#	34.5	
Central obscuration	200 x 230 mm	
FOV	0.5'	
Throughput	33%	in H band
REVOLT design parameters		
Shack Hartmann WFS		
Detector	C-Blue One	
Quantum efficiency	0.7	at 540 nm
Read Noise	3.5 e^-	See Section 5.5
Lenslet array (LA)	16 x 16	
Subaperture size	8 cm	D/LA
Pixels/subapertures	22	
Plate scale	0.7"	
FOV/subaperture	15.4"	
Frame rate	1khz	
DM	17 x 17	
Science path		
Detector	GoldEye Allied vision	
Read Noise	170 e^-	Manufacturer supplied
Gain	2.6	Manufacturer supplied
Quantum efficiency	0.60	at H-band
plate scale	0.0896"	See Section 5.4.1

Table 5.1: Summary of telescope and REVOLT design parameters

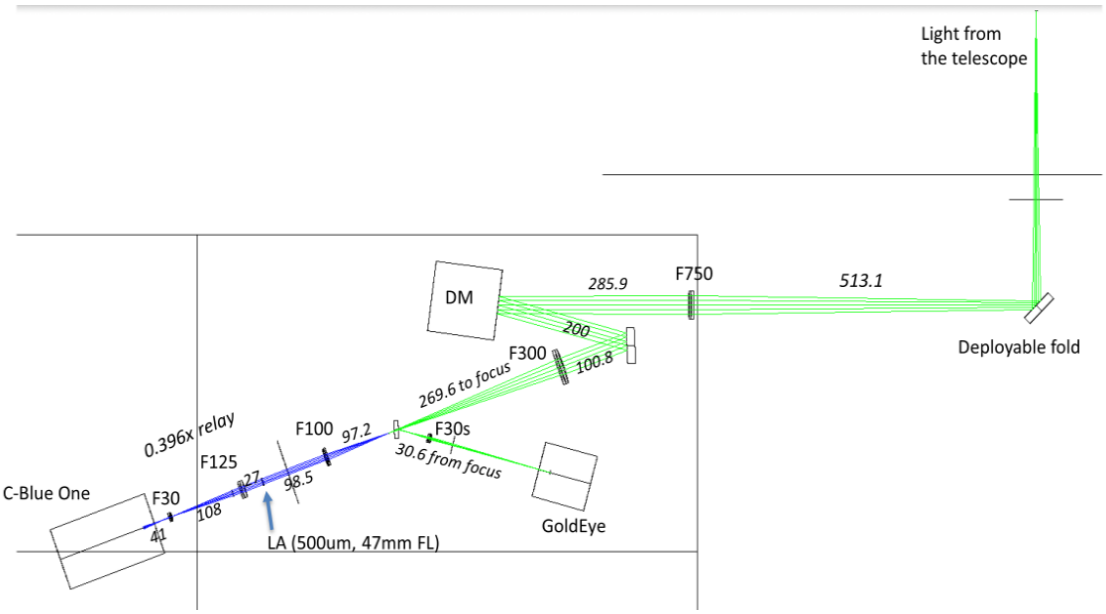

Figure 5.1: Optical layout of the REVOLT: Light from the coudÃ© focus is relayed to the DM which is refocused and split into visible and near-infrared paths. The visible light continues past the dichroic beamsplitter toward the SHWFS (blue path) while the reflected near-infrared is sent to the science camera (green path). All indicated distances are in mm.

et al., 2022), GNAO (Dunn et al., 2022), GIRMOS (Mueller et al., 2022) and TMT NFIRAOS (Gamroth et al., 2022). It consists of generalized RTC code blocks in modular, flexible, and configurable structures that allow for the development of an RTC with reduced effort which improves the quality of the control system by extensive testing of the common code base across multiple projects. It was originally designed for the NFIRAOS RTC and subsequently generalized for application to other AO systems. Implemented in C/C++, its CPU-based architecture can use off-the-shelf hardware that allows for quick deployment. It supports various types of AO systems: SCAO, MCAO, Laser Tomography AO (LTAO) / Ground Layer AO (GLAO), and MOAO. The primary goal of HEART is to reduce the development time and cost of next-generation AO control systems while providing more reliable and robust control software that minimizes maintenance effort and promotes code reusability.

REVOLT has allowed the HEART team to extensively test the RTC with an on-sky AO system. A HEART graphical user interface was built for REVOLT and is shown in Figure 5.2. The HEART interface allows users to adjust parameters as well as save telemetry directly from the user interface.

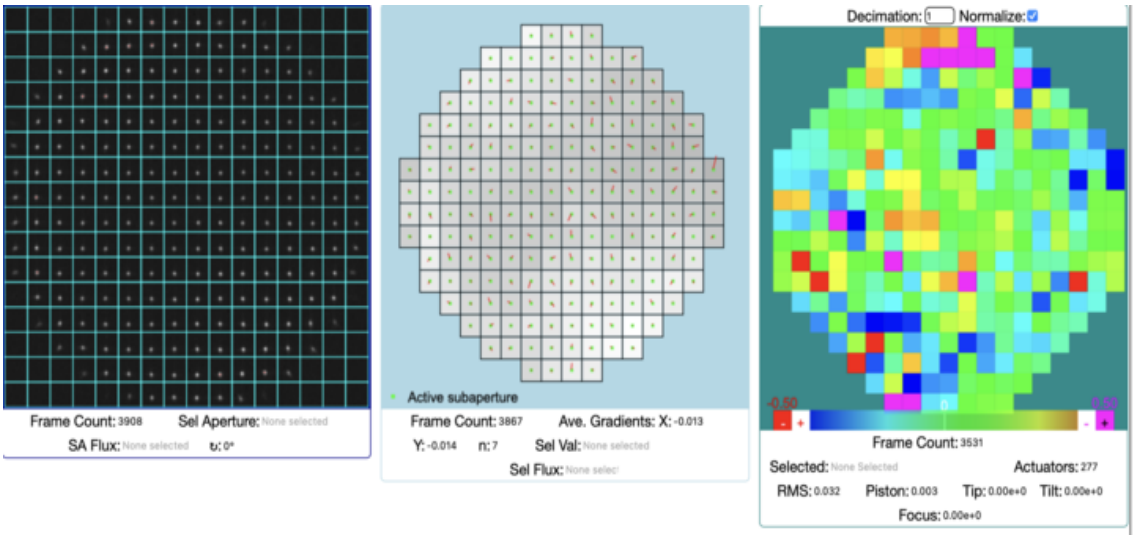

Figure 5.2: Graphical user interface of HEART as seen from REVOLT operation.

5.2.3 Integration with McKellar Telescope

The McKellar Telescope is a 1.22 m telescope with an f/34.5 beam that feeds the coudé focus. The telescope is primarily used with a visible coudé spectrograph. We measured the transmission of the telescope at the coudé focus in the optical and near-infrared. The transmission was 60% in the R-band, 55% in J-band, and 33% in H-band. The median seeing at the site is poor, usually between 1.5-2" which is roughly equivalent to $r_0 = 5$ cm at 0.5 μm. The site influenced the REVOLT design, as we recognized that we would need small subapertures ($\sim$ 8 cm subapertures) to provide a reasonable AO correction. We also knew that the system would have to operate with a high frame rate to keep up with the turbulence moving across these small apertures. These two factors limit the REVOLT target selection to very bright stars.

REVOLT was first built in a laboratory at NRC HAA. A calibration source replicating the telescope focus was placed at the same distance from REVOLT as the planned location of REVOLT in the coudé room. After optics were aligned in the laboratory REVOLT bench was moved to the coudé room (see Fig. 5.3) and final adjustments were made to align the bench using the telescope focus and the calibration source. A motorized fold mirror directed the light from the telescope to either REVOLT or the McKellar coudé spectrograph when REVOLT is not in use. As we discuss below, we observed vibration with REVOLT. The telescope is likely producing a significant fraction of this vibration. Compressors intermittently run and dome movement may induce vibrations that REVOLT can sense.

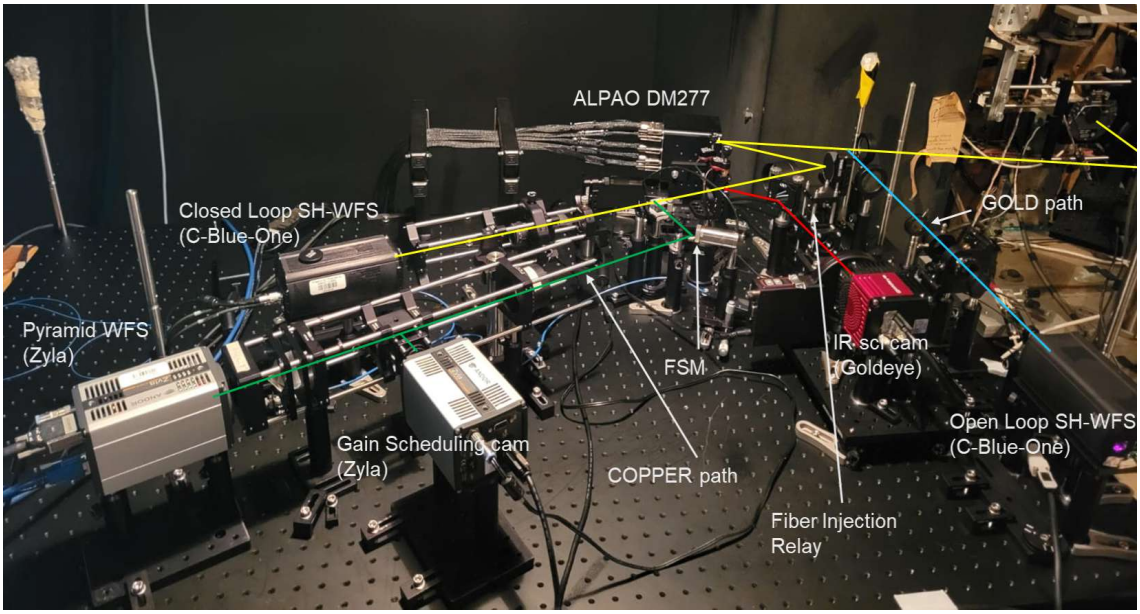

Figure 5.3: REVOLT in the coudÃ© room of McKeller telescope. The yellow and red path shows the base REVOLT instrument.

5.3 Observations

The REVOLT system has been deployed during multiple observing runs. The on-sky data used in the paper was acquired during the night of September 28-29 under clear weather conditions. The typical seeing at the DAO is approximately 2" corresponding to a Fried parameter (r_0) of ~5 cm at 0.5 μm), although it can change drastically over the night. Conditions on September 28-29 were significantly better than average, however, with an estimated seeing closer to 1" to 1.5". The McKellar telescope is equipped with an auto-guider, which is used for both acquisition and tracking of targets throughout the night. Initially, targets were acquired by the telescope, followed by observations conducted with the REVOLT AO loop either engaged (closed) or disengaged (off). Telemetry for REVOLT, including WFS gradients, DM commands, and WFS raw pixel data, is acquired using the HEART RTC. Data from a bright target was utilized to ensure a high SNR. Calibration data used in this paper was acquired on a different day using a broadband light source. The data used in this work is presented in Table 5.2.

Object	exp time(ms)	# of exps	Data taken	Notes
		On-Sky		
Capella	0.75	500	2023 Sep 29	CL science image (AM = 1.09, H = -1.57)
,,	0.891	5768	2023 Sep 29	Telemetry - CL slopes
,,	0.891	7687	2023 Sep 29	Telemetry - OL slopes
,,	0.891	1857	2023 Sep 29	Telemetry - CL WFS raw pixel data
Castor AB	0.75	500	2023 Sep 29	CL science image
		Calibration data		
Calibration source	0.75	1	2024 Jan 23	CL science image
,,	0.891	14164	2024 Jan 23	Telemetry - CL slopes
,,	0.891	15015	2024 Jan 23	Telemetry - OL slopes
Dark	0.75	500	2024 Jan 23	Science camera dark frame
Dark	0.891	10	2024 Jan 23	WFS camera dark frame

Table 5.2: Observation log. AM is the airmass. CL is when loop is closed and OL is open-loop (AO off)

5.4 REVOLT Performance

5.4.1 Science Camera Performance

In this section we discuss the performance of REVOLT science camera.

Throughput of REVOLT science channel

To compute the throughput of the science channel, we use observations of *Capella* due to its high SNR. We first subtracted the median dark frame from each science frame and then the sky background by subtracting the median of a "blank" section of the image. The total analog-to-digital units (ADU) were measured for each image and were divided by the total expected ADU to compute throughput for each image. The median throughput was 0.12 ± 0.02 which is consistent with the expected throughput accounting for losses due to the telescope (Table 5.1), REVOLT optics, and detector quantum efficiency.

After reducing our data, we found that our observations of Capella were close to saturated on the science camera. Only some frames were saturated, and we removed these from consideration. This will reduce our on-sky SR measurement (discussed in Section 5.4.1) slightly because we are removing frames with the largest peak values, and because detector non-linearities will also suppress the maximum reported values. We discuss this more in Section 5.7.6.

Science Camera Platescale

The on-sky plate scale of the REVOLT science camera is important in our performance analysis since plate scale errors can affect SR measurements. To compute the plate scale of the science camera, we compute the distance between the two stars in the Castor binary system and compare it to the 5.5" distance between them in September 2022 (Torres et al., 2022). Computing the distance between the two stars is challenging due to low SNR. After background and sky subtraction we fit Gaussian models to CASTOR A and B to determine that the distance between the model peaks is 61.4 pixels (see Fig. 5.4) which yielded a plate scale of 0.0896 arcsec. This measurement is consistent with the design parameters and an earlier measurement of 0.091" (Jackson et al., 2023).

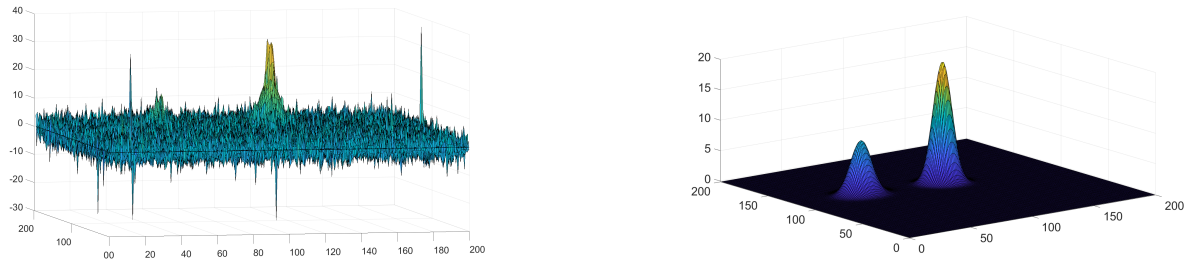

(a) (b)

Figure 5.4: Top: Castor binary system after dark and background subtraction. Bottom: The model fit is used to compute the distance between them.

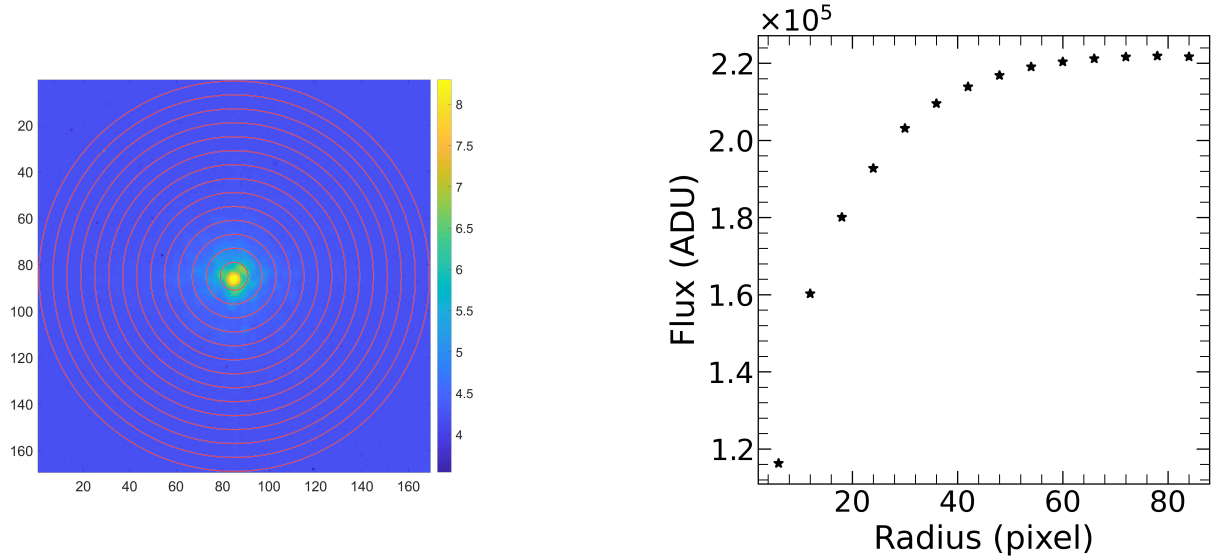

(a) (b)

Figure 5.5: (a) Science camera image of the Capella PSF with progressive circles (b) Curve of growth shows the encircled energy as a function of radius. The curve of growth is constant at large radii, indicating that the background subtraction is good.

REVOLT Strehl Ratio Measurement

An ideal PSF was generated for the 1.22 m McKellar telescope with a central obscuration for the H-band, using a plate scale four times finer than that derived in Section 5.4.1 to mitigate the reduction in peak flux due to sampling. This ideal PSF can then be compared to the on-sky image to estimate the SR. We performed background and sky correction as discussed in Section 5.4.1 and generated a median science frame. To ensure that the background subtraction was reasonable, we plotted the curve of growth, which showed no increase in flux at the edges of the image (see Fig. 5.5). To calculate the SR, we set an aperture radius of 3.5". Using the same Gaussian fitting code mentioned in Section 5.4.1, we computed the peak flux for the science image. The ratio of the peak flux of the science image to the peak flux of the ideal PSF gives the SR. The same method was used to compute the SR for the calibration and OOMAO data (see Section 5.6). We found the SR to be 30% and 58% for on-sky and calibration sources respectively.

5.5 WFS Performance

Read noise computation for WFS

The readnoise of the WFS camera was computed by averaging 10 dark frames taken at 1khz and with an exposure time of 891 μsec. A median was calculated and subtracted from the averaged frame and then we determined a readnoise from the image of 3.5 electrons which is close to the manufacturer-supplied values.

5.5.1 Temporal performance of REVOLT

The PSD of our data was computed by first subtracting the median values computed from the time series from the x- and y-slopes, effectively removing any static offsets. Then we computed the median of each x- and y-slopes for each frame, using only the active sub-apertures with flux equal to or higher than 70% of the median flux. This approach minimized noise while retaining sufficient sub-apertures to compute average x- and y-tilts effectively. Using these average x- and y-tilts we computed the PSD using the *pwelch function* within MATLAB with 50 % overlap with Hanning window (see Fig. 5.6). From the PSD plots, we can see sharp peaks in both on-sky and calibration data for x-tilt but not for y indicating it is likely coming from vibrations propagating through the REVOLT bench. We discuss the calculation of the wavefront error (WFE) due to vibrations in Section 5.7.3. The rejection transfer functions can be computed by taking the ratio of CL and OL PSDs (see Fig. 5.6) which agree with the model transfer function with a 1.3 msec delay.

5.6 OOMAO simulations of REVOLT

To compare REVOLT's on-sky results and evaluate system performance, we performed OOMAO simulations, a Monte Carlo modeling code for adaptive optics simulations (Conan & Correia, 2014). To closely replicate the on-sky results of REVOLT, we modified the OOMAO simulations to match the telescope and REVOLT parameters described in Table 5.1.

Since HEART provided complete telemetry, including WFS pixel data, we were able to accurately measure the noise in regions of the WFS away from NGS images. The measured

noise was twice the detector readnoise. The bright night sky likely contributed to the excess noise. We therefore used this measured WFS noise in our OOMAO simulations of REVOLT. Compounding this excess noise, significant scintillation was observed that night which manifested as changing NGS brightnesses subaperture-to-subaperture and from frame-to-frame. We discuss the potential effect of scintillation on REVOLT performance in Section 5.7.6. The NGS magnitude in OOMAO was set to reproduce the median flux measured in on-sky WFS sub-apertures.

After initializing OOMAO with these parameters, we ran several simulations with different values of the Fried parameter (r_0) until the standard deviation of the OOMAO y-slopes equaled the standard deviation of the measured on-sky y-slopes (Fig. 5.7). We ignored the x-slopes as they suffered from vibration (see Section 5.7.3 and Fig. 5.6). We found that OOMAO simulations using an $r_0 = 9$ cm most closely matched the on-sky data. A value of $r_0 = 9$ cm at DAO was significantly better than usually observed at this site, but other data from that night, such as the telescope tracking camera, also suggest that the seeing was excellent for DAO. We did look at science images of Capella taken before the REVOLT AO loops were closed, but unfortunately those images had large static errors, probably due to the uncommanded DM shape, so the quality of these images was poor.

Although OOMAO is an excellent tool for evaluating how an ideal AO system would perform, it cannot account for all sources of error, including non-common path aberrations (NCPA), errors due to imperfect optical surfaces, vibration, and other errors present only observed on-sky.

5.7 Wavefront Error Budget for REVOLT

In this section, we evaluate the various known sources of wavefront errors for these REVOLT observations. We derive these error terms through a variety of means, including measurements from the PSDs and Rejection Transfer Functions, measurements from the on-sky science images and WFS data, calibration data, and OOMAO simulations.

Figure 5.8 shows the cross-section of the PSFs for different datasets used to compute the SR. Note that the on-sky and calibration PSFs are broadened due to vibration. Table 5.3 presents the SR for different data as well as RMS values while Table 5.4 presents the wavefront error budget.

Data	Strehl Ratio	σ (nm)	Notes
On-sky	0.30	288	includes all errors
Calibration	0.58	194	includes optical, alignment, and NCPA errors
OOMAO (matching on-sky)	0.63	177	includes σ_{lag}, σ_{fit} and σ_{wfs}
OOMAO (no-noise)	0.73	147	only σ_{lag} and σ_{fit}
OOMAO (no-noise, open-loop)	0.96	51	only σ_{fit}

Table 5.3: SR and WFS error from observations and simulations.

5.7.1 Fitting and Aliasing Error

The finite size and shape of individual DM actuators can lead to fitting errors when correcting an arbitrary wavefront, particularly at high spatial frequencies. Additionally, coupling between adjacent actuators further limits the DM's ability to fully correct the distorted wavefront. The fitting and aliasing combined error was measured by conducting open-loop simulations with OOMAO. In our setup, we configured the gain to 100% and set the WFS noise to zero. In the open-loop mode, the WFS and DM are presented with a set of realizations of uncorrelated turbulence with an $r_0 = 9$ cm, and then corrections are applied independently, thereby isolating the DM fitting error. The estimate of 51 nm RMS fitting plus aliasing error derived in this way is slightly larger, but consistent with the analytic formula for fitting and aliasing error, $0.3(d/r_0)^{5/3}$.

5.7.2 WFS Noise

The WFS noise impacts the correction of an AO system by introducing inaccuracies in the measurement of slopes. These inaccuracies propagate through the system, degrading the effectiveness of the wavefront correction and resulting in residual errors. WFS noise levels are influenced by the luminosity of the guide star and the readout noise of the camera. To quantify the error due to WFS noise, we repeated the OOMAO simulations, replicating the REVOLT results but without including any WFS noise. By quadratically subtracting the RMS from the SR of this WFS noise-free simulation from that of the simulation replicating the REVOLT results, we determined an error of 99 nm RMS attributable to WFS noise.

5.7.3 Vibration

To compute the wavefront error due to vibration, we examined the PSD for x- and y-tilt using on-sky data (see Fig. 5.6). For the x-tilt, we observed prominent peaks at 55 Hz and a smaller peak at 121 Hz indicating a vibration predominantly propagating in x-direction but not in y. To determine the noise contribution from these vibration peaks, we compared the PSDs with and without these peaks (see Fig. 5.9) and multiplied the ratio by the variance of the x-tilts. This result was then converted into nanometers using the WFS plate scale to yield a vibration wavefront error of 63 nm RMS. We found a similar contribution for the x-tilt in the calibration data. The contribution from the significantly smaller peaks in the

y-tilts was negligible and was therefore ignored.

5.7.4 Lag error

Lag error occurs due to the time delay between the wavefront measurement and the correction applied by the DM. This delay results in corrections based on outdated information, leading to incomplete correction and residual wavefront errors. Assuming Kolmogorov turbulence and a large outer scale ($L_0 \to \infty$), the lag error can be represented by the Hardy equation (Hardy, 1998):

$$\sigma_{lag}{}^2 \simeq 28.4 \left(\frac{t}{t_0}\right)^{5/3} \tag{5.1}$$

Here, t is the delay, which we computed earlier as 1.3 ms (see Section 5.5.1), and t_0 is the inverse of Greenwood frequency given by r_0/V, where r_0 is Fried parameters (see Section 5.6) and assuming V = 20 m/sec, we determine a lag error of $\sigma_{lag}{}^2 = 3.58$ radians or $\sigma_{lag} =$ 150 nm RMS.

5.7.5 Calibration errors

The REVOLT wavefront error budget also needs to contain a term accounting for the imperfect optics in the system. There are some elements of the optical path that are different between the science and WFS channels, so errors recorded and corrected by WFS are not the same seen by the science camera, which are called non-common path aberrations. The REVOLT WFS uses visible light while the science camera is optimized for H-band, the differences in the index of refraction for different wavelengths can introduce wavelength-dependent wavefront errors. In addition, optical elements cannot be perfectly aligned and temperature fluctuations can contribute to the wavefront error. As described above, we did use a calibration data set to try and correct for some of these optical errors, including non-common path aberrations by applying different modes to the DM to maximize the calibrated SR. This measurement of 58% SR sets the maximum SR possible with REVOLT (Table 5.3) and includes all errors coming from the bench including vibrations (see Section 5.7.3). If vibrations could be removed, the calibration SR would increase to 62%. In Table 5.4, we list the calibration wavefront error excluding vibration (since vibration is tabulated separately).

Term	Errors (nm)	Ref
Fitting error	51	Section 5.7.1
WFS	99	Section 5.7.2
Vibration	63	Section 5.7.3
Lag error	150	Section 5.7.4
Residual calibration	183	Section 5.7.5
Total	269	
On-sky	288	
Difference	103	Section 5.7.6

Table 5.4: Wavefront error budget

5.7.6 Residual Wavefront Errors

In Table 5.4, we present the REVOLT wavefront error budget including all the terms above. Adding all individual terms in quadrature, we find that the total REVOLT wavefront error should be 269 nm RMS. We find a close agreement between the on-sky measurement of 288 nm RMS and this quadrature sum of WFE terms. Only a small unexplained residual WFE of 103 nm RMS remains.

As discussed in Section 5.4.1, the on-sky science frames for Capella were nearly saturated (and some saturated frames were removed from the analysis). Detector non-linearities and the removal of saturated frames both would suppress the measured SR slightly. It is possible that this could account for a substantial fraction of the residual 103 nm RMS WFE.

Another source of WFE not accounted for above that could account for the residual WFE is scintillation observed in the WFS. As discussed in Section 5.6, the observed WFS noise was significantly higher compared to the simulations. We analyzed the WFS frames for both the on-sky, calibration and the OOMAO simulations data. We selected sub-apertures that were not close to the edges or the central obscuration and plotted the net fluxes for each frame. We found that the fluxes varied significantly over time for the on-sky data, comparing to calibration and OOMAO data as shown in Fig. 5.10. This indicates that on this quite good night at DAO ($r_0 = 9$ cm is excellent for the site), we were observing atmospheric scintillation even though we were observing at low airmass. This suggests that the significantly larger noise seen in the on-sky data is likely due to this scintillation which furthermore could explain the small residual WFE error.

5.8 Summary

REVOLT is a single conjugate adaptive optics system installed on the 1.22m McKeller telescope at Dominion Astrophysical Observatory in Victoria, Canada. It uses a C-blue One high-speed camera as a SHWFS which drives the commercially available ALPAO deformable mirror. The RealTime control is established using HEART RTC system developed by NRC-Herzberg, Victoria. The light from the telescope is split into visible WFS and NIR science paths. We collected AO telemetry and science frames both from calibration sessions and on-sky observations. We observed a SR of 30% in H-band on-sky for Capella on the night of September 28, 2023.

Utilizing OOMAO simulations, various calculations, and both calibration and on-sky data, we computed the distinct contributions of wavefront errors arising from DM fitting, WFS noise, lag, vibrations, and the residual calibration errors, including optical misalignments, residual non-common path aberrations, chromatic errors, and other bench-related errors. The difference between the contributions to the WFE budget and the on-sky measurement was small and could be due to wavefront errors associated with scintillation. Efforts to enhance REVOLT performance have focused on utilizing the calibration source to refine alignment and further correct NCPA, which is expected to significantly improve overall performance when the conditions are favorable ($r_0 \sim 10$ cm). Future versions of REVOLT are expected to deliver overall performance improvements, including reductions in residual and vibration errors.

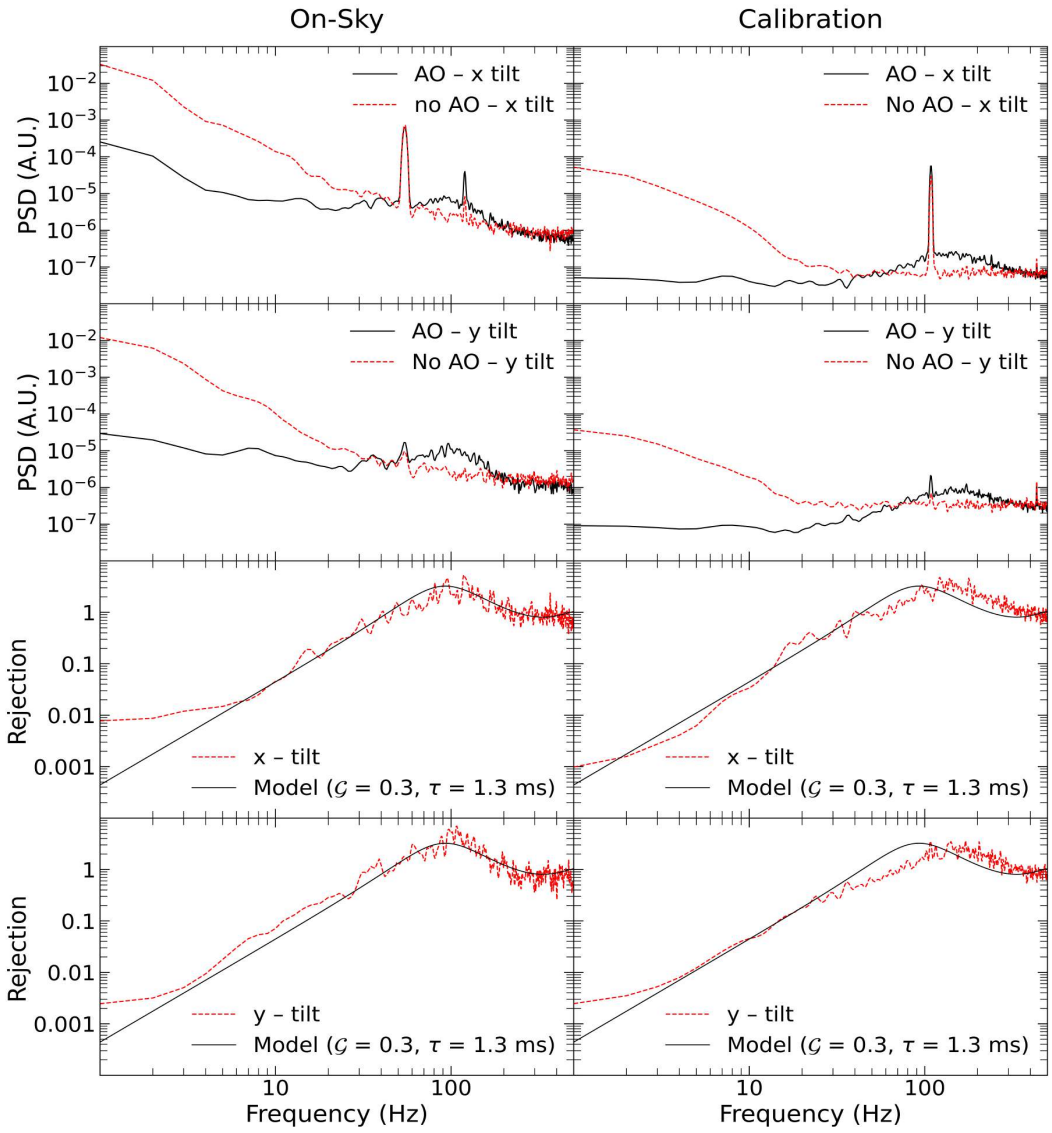

Figure 5.6: Left panels: PSD in arbitrary pixels unit (A.U.) and Rejection transfer function vs frequency for OL (i.e. AO–off) and CL case for on-sky data, here $\mathcal{G}$ and τ represents delay and gain respectively. Right panels: same for calibration data. The sharp peaks in PSDs for x-tilt indicate a vibration predominantly propagating in the x-direction.

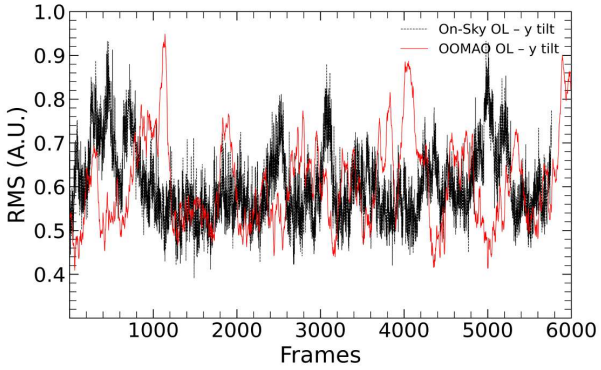

Figure 5.7: Computing r_0: RMS Y tilt from OOMAO and on-sky data plotted together.

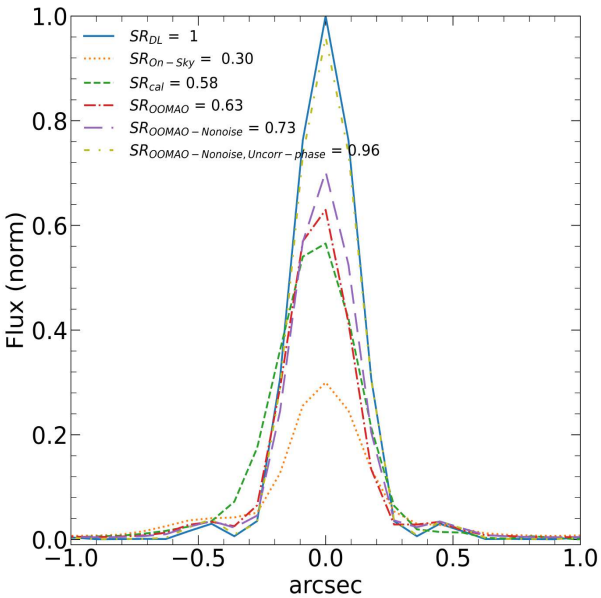

Figure 5.8: Cross-section of PSFs for different datasets used to compute SRs corresponding to different wavefront error terms.

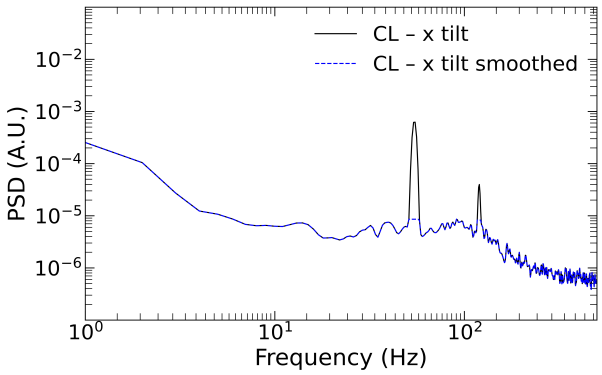

Figure 5.9: PSD vs frequency for CL with peaks due to vibrations smoothed out.

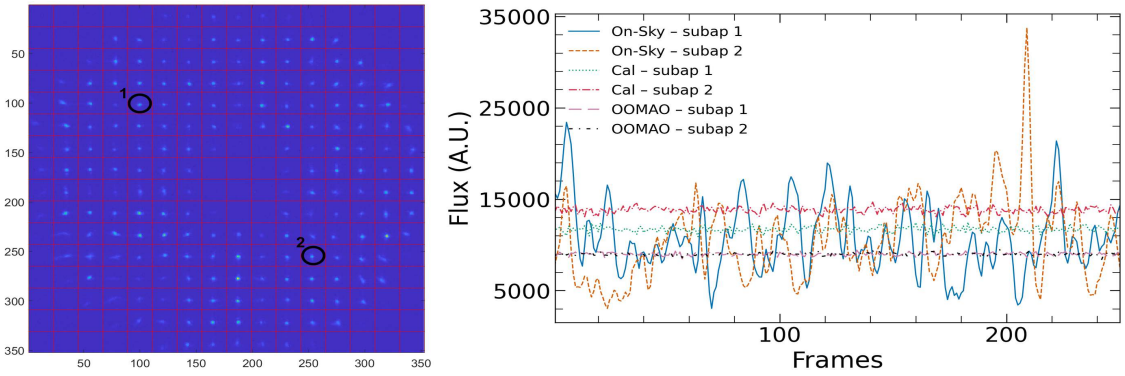

Figure 5.10: (a) a WFS with selected sub-apertures marked (b) Flux computed in each marked sub-aperture vs frames for on-sky, calibration, and OOMAO data. For clarity, we only plotted two sub-apertures.

Chapter 6

Conclusions

This thesis presents a comprehensive exploration of adaptive optics, photometric analysis, and precision calibration tools, all contributing to the broader field of observational astronomy. Each of the four major projects: MCAO performance with globular cluster photometry, the Herzberg NFIRAOS Optical Simulator, the Keck Precision Calibration Unit, and the performance analysis of the REVOLT instrument demonstrates significant advancements in the optimization and application of adaptive optics systems. By synthesizing the key results from these projects, it is possible to understand how they contribute to the future of astronomy, particularly in the era of extremely large telescopes.

6.1 MCAO Performance with Globular Cluster Photometry

The photometric analysis of the globular cluster NGC 5904 using the GeMS, provided a critical evaluation of MCAO ability to resolve dense stellar fields. The NIR photometry obtained from this study surpassed previous observations by delivering higher spatial resolution and greater photometric depth. This allowed for the indication of multiple stellar populations below main sequence, advancing the understanding of globular cluster formation and stellar evolution. The most significant result of this project was the successful use of crowding correction techniques to improve the accuracy of photometric extractions in dense stellar regions. This is particularly important for future ELT systems, as these telescopes will need to handle similarly complex and crowded fields. Therefore, this study helps de-

velop the necessary tools to exploit future MCAO systems fully. In future, a second epoch of GeMS photometry for M5, taken in 2019 (Program ID: GS-2019A-Q-203, P.I.: Taheri), will be combined with this data to test astrometric solutions from ground-based AO imaging alone. In addition, existing UVâ€“VIS photometry data from the HST can be combined with these observations to place tighter constraints on the photometry, particularly along the red giant branch and in determining chemical abundances. This, in turn, would also aid in proper motion cleaning and help eliminate field stars, although we have already taken robust steps to substantially clean our photometry.

6.2 Herzberg NFIRAOS Optical Simulator

HeNOS was developed to simulate the performance of the NFIRAOS adaptive optics system for the TMT. By simulating real-world conditions, HeNOS allowed for extensive testing of wavefront sensors, guide stars, and deformable mirrors. The simulation results were instrumental in refining the design of NFIRAOS, ensuring that it will be capable of delivering high-resolution images across a wide field of view. One of the most important findings from this project was the identification of potential sources of distortion, such as artifacts caused by interference from camera windows and the Talbot effect. Therefore, we suggest that using a focal plane mask instead of a lenslet array may be more effective in mitigating ghost imaging caused by the Talbot effect. Addressing these issues early in the development process is essential for achieving the desired performance when NFIRAOS is eventually deployed on the TMT. Furthermore, HeNOS demonstrated the importance of simulating real-world conditions, providing valuable insights that will be applicable to future adaptive optics systems. Once an NGS pattern that produces a clean pupil image at the Pyramid WFS is established, next aim would be to study the matched filters (MFs) used for centroid measurements on the LGS WFS (Gilles & Ellerbroek, 2006). The MF, derived from the mean reference image of elongated LGS spots, acts as a normalized gradient mask in x and y. When applied as a dot product with WFS images, it yields x and y slopes. Additionally, a pinhole grid could also be added to HeNOS to measure optical distortion. This will help in understand the quality of astrometry produced by NFIRAOS with its focal plane mask.

6.3 Keck Precision Calibration Unit

The Keck PCU was designed to improve the geometric distortion calibration of adaptive optics instruments, such as NIRC2 and OSIRIS, on the Keck Telescope. The primary innovation in this project was the use of a pinhole mask with known reference points, allowing for calibration during the day and reducing the need for valuable on-sky time. This project demonstrated a significant improvement in calibration accuracy, reaching an order-of-magnitude better precision compared to traditional methods. The PCU has broad implications not only for Keck but also for future ELT systems, such as NFIRAOS on the TMT, which will require similarly high levels of precision. The PCU project serves as a precursor for future calibration units, ensuring that upcoming telescopes can achieve the astrometric accuracy necessary for their ambitious scientific goals. Since our involvement in the project concluded, the PCU hardware has been installed on the Keck AO bench (Surendran et al., 2022), and the necessary tools required for daytime calibration are being developed (Wizinowich et al., 2024).

6.4 Performance Analysis of the REVOLT Instrument

The REVOLT instrument, developed to simulate and analyze adaptive optics performance in real observational conditions, provided key data on how an adaptive optics system responds to environmental changes and atmospheric turbulence. The analysis of the opto-mechanical design, wavefront sensor performance, and temporal characteristics of the system revealed areas for improvement in adaptive optics technology. One of the major outcomes of the REVOLT project was the detailed wavefront error budget, which identified residual wavefront errors, vibration-induced distortions, and lag errors as critical areas of focus for future systems. The data obtained from REVOLT simulations are invaluable for refining the next generation of adaptive optics systems, particularly those that will be deployed on extremely large telescopes. This project highlights the importance of continuous testing and refinement in ensuring the success of complex optical systems. The REVOLT on-sky experiment will continue to expand and mature in the future. Already, a Pyramid WFS and open loop channel have been added to REVOLT, and in the future ALPAO DM will be replaced by a low-powered MEMS DM currently being developed by the NRC Nanotechnology Center in Edmonton.

The four projects presented in this thesis are united by a common theme: the optimization of adaptive optics systems to maximize their scientific potential. Whether through improving the performance of MCAO systems in resolving dense stellar fields, simulating real-world conditions for NFIRAOS, developing high-precision calibration units, or refining the performance of adaptive optics under real-world conditions, each project contributes to the overarching goal of improving astronomical observations. Adaptive optics systems are essential for overcoming the limitations imposed by Earth's atmosphere, allowing ground-based telescopes to achieve near-diffraction-limited imaging. The projects in this thesis illustrate how adaptive optics technology is evolving to meet the demands of next-generation telescopes, such as the TMT, which will push the boundaries of astronomical discovery. By improving the resolution, precision, and calibration of these systems, astronomers will be able to study faint and distant objects with unprecedented clarity. The synthesis of the scientific and technological contributions from these projects demonstrates the critical role that adaptive optics will play in the future of observational astronomy. As ELTs come online in the coming decades, the tools and techniques developed through this research will be essential in unlocking new discoveries about the universe. This thesis, therefore, serves not only as a contribution to the field of adaptive optics but also as a foundation for future research that will continue to shape the course of astronomical exploration.

Appendix A

Detailed data calibrations

Here, we describe the detailed steps of the data reduction process for the photometric analysis of M5, as discussed in Chapter 2.

A.1 Crowding correction

As discussed in section 2, apart from trimming the standard photometric catalogue to improve the zero point calibration (see Fig. A.1 for Ks band). To correct the effects of crowding, we adopted the crowding correction technique developed by Turri et al. (2017). However, improvements in the technique were needed as this did not provide homogenous photometry as described in section A.2. The adopted steps are described below.

- The first step involves computing the "seeing" of the standard photometric catalogue which basically means computing the median of the distances of the closest neighbor for each star in the standard photometric catalogue (see Fig. A.2). which turned out to be ~ 1" for each J and K_s-band so if two neighboring stars are at least 1" apart it's highly likely that they will be resolved.
- Next, the standard stars that have been matched to the instrumental catalogue and are less than 1.5" apart from each other are removed (Fig. A.3). This is to ensure that the calibration stars are isolated. This step was not included in the method described by (Turri et al., 2017) and was found to be the cause of inhomogeneity observed in the photometry. For the remaining stars in the matched calibration catalogue, their positions

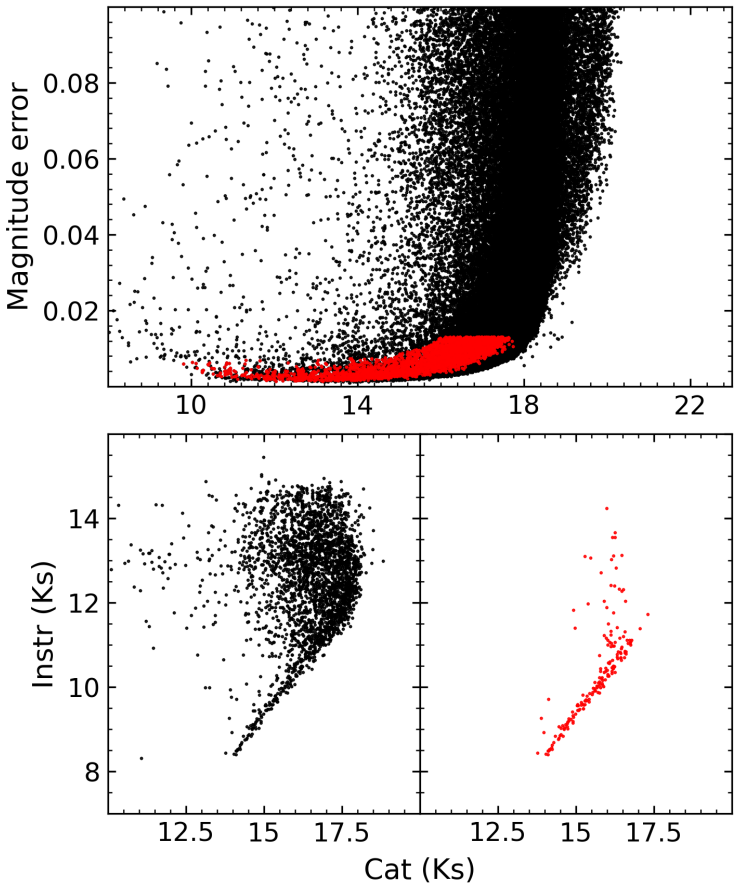

Figure A.1: Same as Fig. 2.7 for the K_s band

are transformed into detector pixel coordinates and overlaid with the GeMS instrumental magnitude measurements.

- The instrumental magnitudes of stars that are within 50 pixels ($\sim$ 1") of the corresponding matched standard catalogue star are combined and replaced with the old instrumental magnitude of the stars in calibration. In this step, we are merging the stars that are resolved in GeMS but not in the standard catalogue to create an equivalent instrumental catalogue 'blob'. Replacing the instrumental magnitude with this provides a better match and improved photometric zero point for calibration.

- As a final step, the new matched catalogue magnitudes were compared to the standard calibration magnitudes, and those with differences larger than 3 sigmas from the mean were removed. Fig. 2.8 and A.4 show improvement in the zero points for one of the exposures of 160s after crowding correction has been applied.

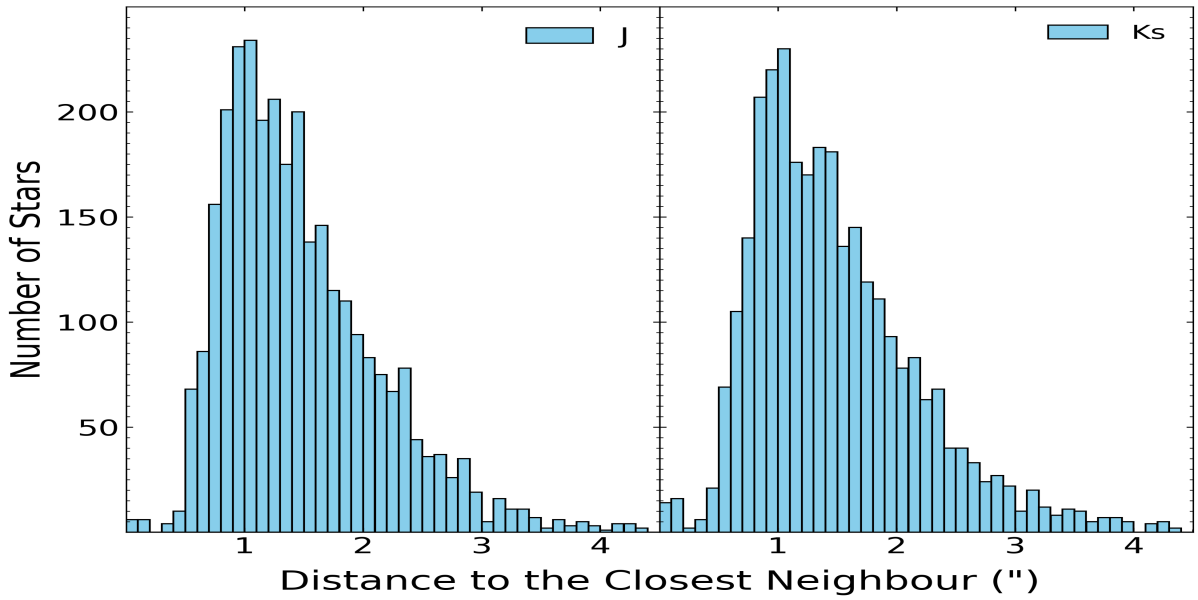

Figure A.2: Distance to the closest neighbor for each star of the standard photometric catalogue for J (Left) and K_s (Right) band.

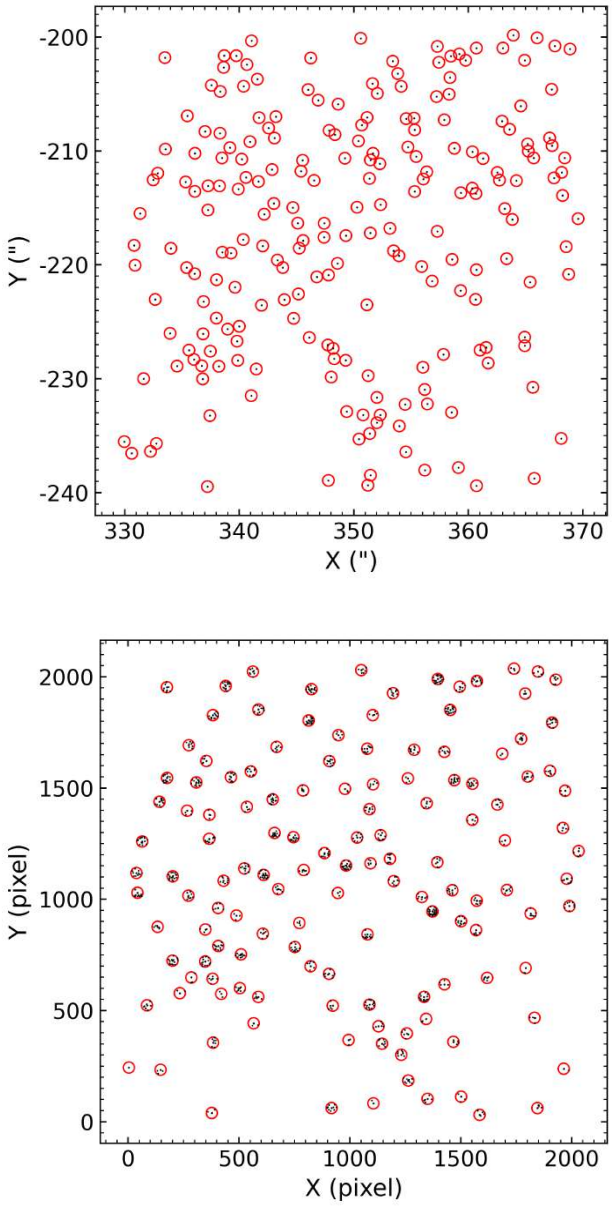

Figure A.3: (a) Calibration stars for one of the chips and 160 sec of J band with a circle of 1" drawn around them. Stars that are closer than 1.5" to each other are removed. (b) The remaining calibration stars are transformed into detector pixel coordinates and are plotted along with the instrumental catalogue stars that are within 1" (or 50 pixels) from each one of them. The magnitudes of these instrumental catalogue stars are combined and replaced with the old instrumental magnitude of the stars in calibration match files.

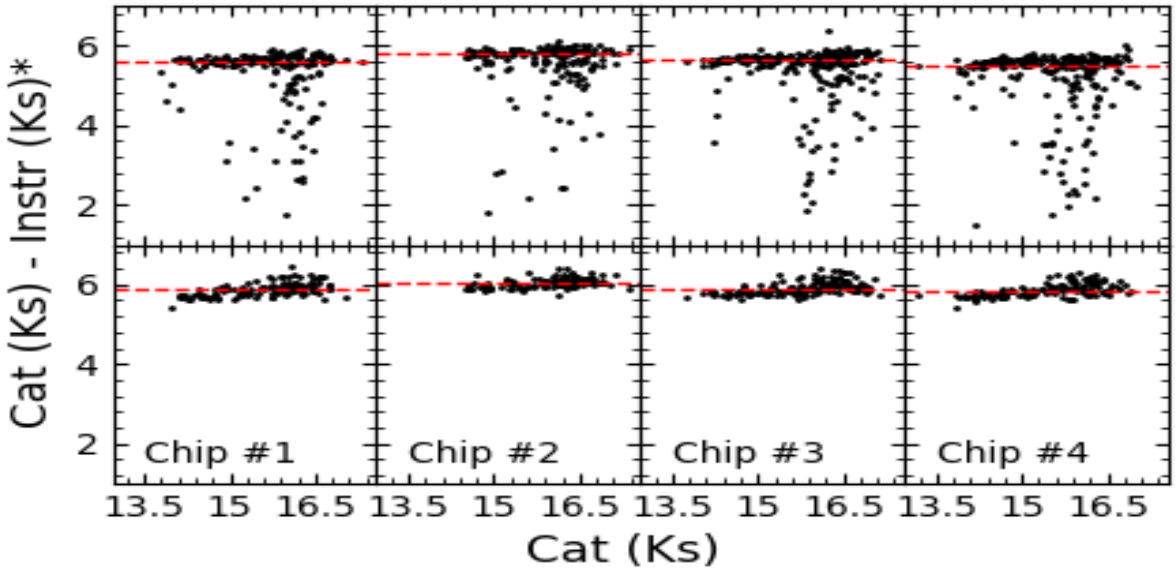

Figure A.4: Same as Fig 2.8 for the K_s band

A.1.1 Cleaning final photometry

After the zero-points are applied to each chip and exposures of the J and K_s band, they are combined to create a master J and K_s catalogues containing calibrated stars. These catalogues are then subjected to a series of cleaning steps to rid of any extended objects, cosmic rays, spurious detection, and poor photometry Artifacts in the data are quantified using magnitude errors, the parameter χ, and the sharpness, which are all quantities provided by DAOPHOT and briefly described below.

- Magnitude error is a compromise between the uncertainty estimated from the photon statistics and the readout noise in the stellar image, and the uncertainty estimated from the residuals of the pixel data from the best-fitting model profile, weighted toward the larger of the two.
- The parameter χ is effectively the ratio of the profile-fitting residuals to the photon statistics and readout noise, quantifying the similarity between the observed and expected profiles (or lack thereof).
- Sharpness is the difference in width between the object and the PSF. Objects that are too small are usually bad pixels or cosmic rays, objects that are too large are usually galaxies or unrecognized blends.

These corrections are applied sequentially. Magnitude errors, χ, and then sharpness are examined (see Fig. A.5). Stars above the red curves are removed from the final catalogues.

Additionally, stars that were not detected in at least three exposures out of the total of eight (with 160-second exposures) were removed, unless they were detected in either the 90-second or 23.5-second exposures. This step helps to eliminate random noise and cosmic ray detections while ensuring a sufficient number of bright stars on the upper CMD.

Finally, after matching the J and K_s band catalogues using DAOMASTER to generate the K_s vs J – K_s CMD, any matched stars with positional differences greater than 0.01" are removed to further refine the CMD's cleanliness.

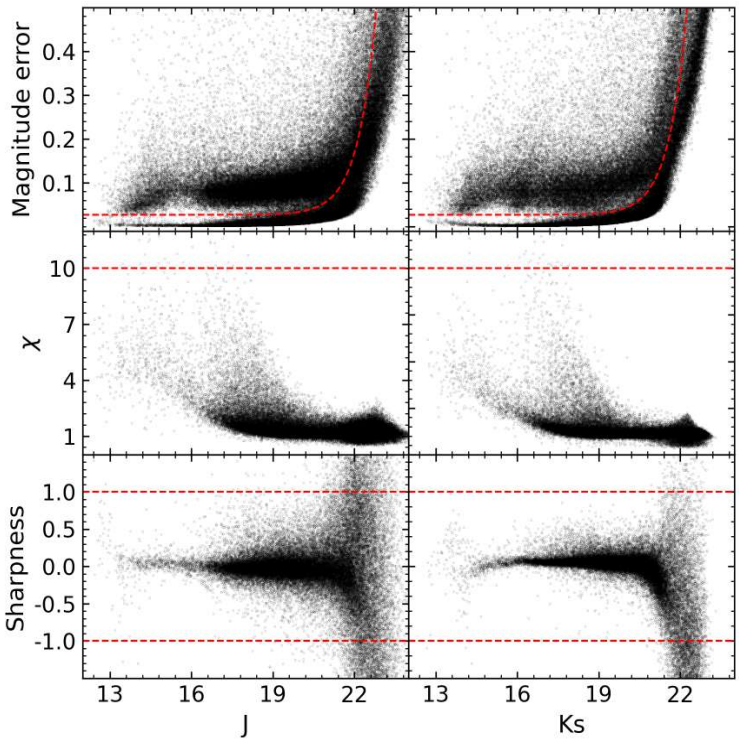

Figure A.5: Cleaning up GeMS photometry: Cut applied to magnitude error, χ and sharpness for each J and K_s band. Cuts were applied sequentially. First for magnitude error: all stars above the curve were removed; resulted data was subjected to χ cut with stars only below line were kept and finally for sharpness: only stars between two lines were used.

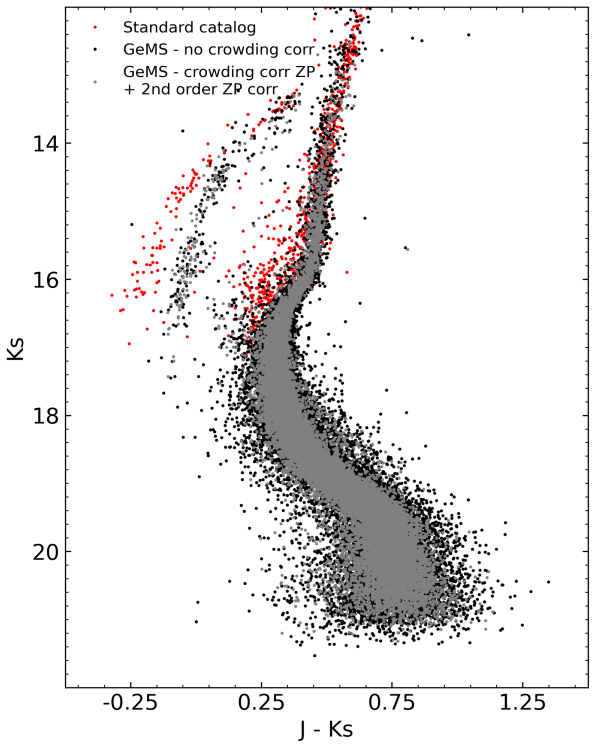

Figure A.6: Color magnitude diagram with or without crowding correction. Second order zero-point correction has been applied to crowding corrected CMD to match with the standard catalog while no such correction was needed for CMD without crowding correction.

A.2 Improvement made with crowding correction in CMD

Fig. A.6 shows the final CMDs when zero-points with or without crowding corrections are applied for calibration. Crowding corrected CMD has been subjected to 2nd order zero-point correction to match with the standard catalog while no such correction was needed for CMD without crowding correction. When both CMDs are overlaid on top of each other, they perfectly match each other but CMD with crowding corrections is better quality-wise and has less photometric errors.

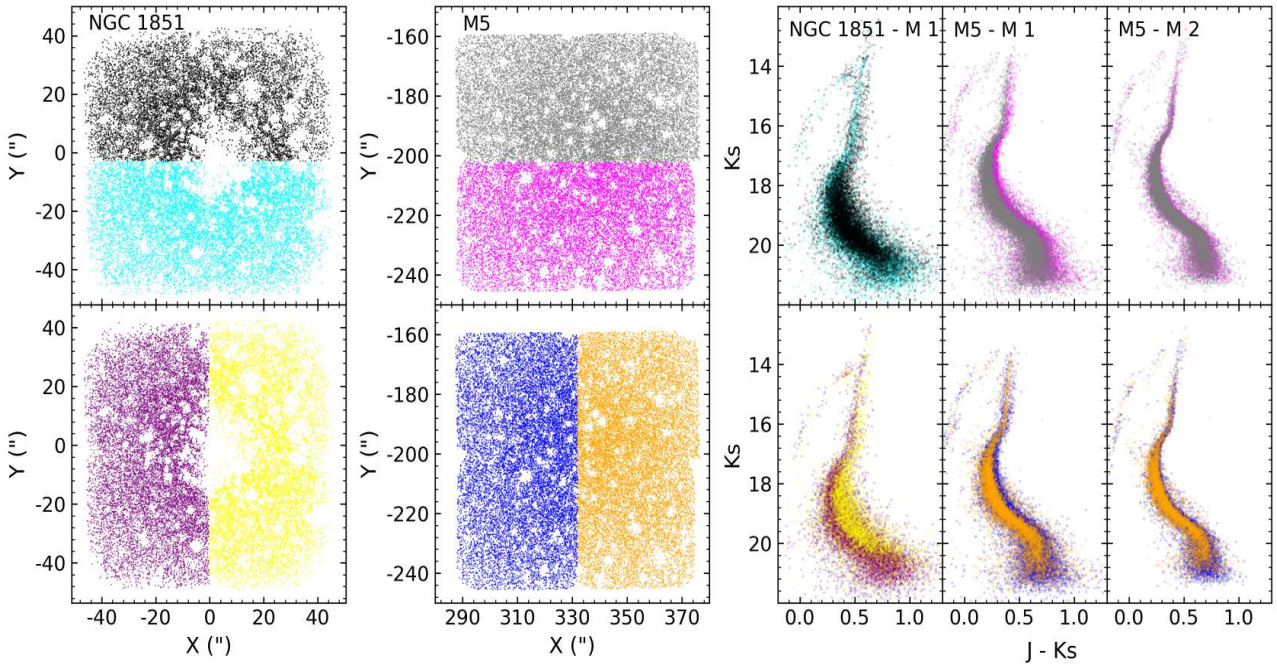

Figure A.7: In the original crowding correction approach discussed by Turri et al. (2017) (referred to as Method 1 or M1 here), resulted photometry was not homogeneous. This becomes evident when star positions for NGC 1851 a central subject in the referenced study (original data provided by Paolo Turri) are visualized and divided into equal sections along the horizontal and vertical axis, and plotted on the colour-magnitude diagram. A similar effect is observed for M5 when using Method 1 for calibration. However, the improved crowding correction method that is adopted in this study (referred to as Method 2 or M2) significantly enhances photometric uniformity, as shown.

A.3 Comparison between crowding correction technique

As mentioned in the main text and Appendix A, the method used by Turri et al. (2017) for crowding correction did not provide homogenous photometry so improvements in the technique were made. The issue was caused by the overlapping stars in the standard photometric catalogue within the seeing radius. Therefore when instrumental magnitudes were summed to create an equivalent seeing limited star (or "blob") many of the stars would be overlapping creating a systematic error. Therefore we decongested the standard photometric catalogue by removing the stars that were closer than 1.5" from each other which improved the homogeneity of the photometry. See Fig. A.7 for details.

B List of Acronyms

ACS Advance Camera for Surveys. 9, 18

AO Adaptive Optics. iv, viii, ix, xiv, xv, 1, 3–7, 9, 12–15, 17, 18, 25, 28, 35, 49, 58–60, 62–65, 68–73, 75–78, 83, 85, 88, 89, 93, 94

CL closed-loop. viii, xv, 78, 82, 89, 91

CMD color-magnitude diagram. xi, xii, 9, 10, 20, 34–36, 39, 41–45

DAO Dominion Astrophysical Observatory. 72, 73, 77, 83, 87

DM Deformable Mirror. ix, xiii, xv, 3, 5, 7, 8, 14, 47–50, 72, 74, 75, 77, 83, 85, 86, 88, 94

E-ELT European Extremely-Large Telescope. 13, 18, 71

ELT Extremely-Large Telescope. iii, 7, 94, 95

ESO European Southern Observatory. 13, 71

FDR final design review. 61, 69

FOV Field of View. ix, 6–8, 18, 24, 25, 35, 36, 47, 48, 61, 62, 66, 74

FWHM full width at half maximum. 2, 21, 63

GC Globular Cluster. 9, 10, 18, 19, 28, 44

GeMS Gemini Multi-Conjugate Adaptive Optics Systems. iii, viii, x–xii, 7, 9, 14, 18–22, 24, 28, 29, 33–37, 40–43, 45, 46, 71, 92, 93

GLAO Ground Layer adaptive optics. 7

GSAOI Gemini South Adaptive Optics Imager. x, 18, 20, 21, 23

HB horizontal branch. 35, 36, 40, 44, 46

HEART Herzberg Extensible Adaptive Real-Time Toolkit. xv, 14, 72, 73, 75–77, 82, 88

HeNOS Herzberg NFIRAOS Optical Simulator. iii, iv, viii, xiii, 11, 15, 47–51, 53, 54, 57, 93

HST Hubble Space Telescope. xii, 9, 10, 12, 18–20, 39, 43–45, 59, 60, 93

LGS Laser Guide Star. ix, x, xiii, 6–8, 23, 47, 49, 93

MAD Multi-Conjugate Adaptive Optics Demonstrator. 71, 72

MCAO Multi-Conjugate Adaptive Optics. iii, ix, 1, 7–11, 14, 15, 18–20, 24, 45, 47, 71, 75, 92, 95

MF matched filter. 93

MLA micro-lenslet array. xiii, xiv, 47–57

MOAO Multi-Object adaptive optics. 7, 72, 75

MORFEO Multi-conjugate Adaptive Optics for ELT Observation for E-ELT. 7

MSK main-sequence knee. xi, xii, 9, 34, 40–43, 45, 46

MSRL main sequence ridge line. xi, 34

MSTO main sequence turn-off. xi, xii, 20, 34, 41–43, 46

NCPA non-common path aberrations. 83, 84, 88

NFIRAOS Narrow-Field Infrared Adaptive Optics System. iii, iv, viii, 7, 11, 13–15, 47, 48, 50, 75, 93–95

NGS Natural Guide Star. viii–x, xiii, 3, 6–8, 21–23, 47–49, 54, 57, 93

NIR Near-Infrared. x, 6, 9, 10, 18, 20, 23, 42, 43, 88, 92

OL open-loop. viii, xv, 78, 82, 89

OOMAO Object Oriented Matlab Adaptive Optics. xv, 81–85, 87, 88, 90, 91

PCU precision calibration unit. xiv, 11, 13, 15, 62–65, 69, 70, 94

PDR preliminary design review. viii, 61, 63, 66, 68, 69

PSD power spectral density. xv, 82, 83, 85, 89, 91

PSF Point Spread Function. ix, x, xv, 2–4, 24–26, 48, 49, 51, 73, 81, 83, 90

REVOLT Research, Experiment and Validation of Adaptive Optics with a Legacy Telescope. iv, viii, xv, 1, 13–15, 47, 71–77, 79, 82, 83, 85–88, 94

RGB red giant branch. 10, 18, 35, 36, 40, 44–46

RMS root-mean-square. xv, 3, 83, 85–87, 90

RTC Real-Time control. 72, 73, 75, 77, 88

SCAO single conjugate adaptive optics. ix, 6, 7, 72, 73, 75

SHWFS Shack-Hartmann Wavefront Sensor. xiii, xv, 14, 47, 49, 72, 73, 75, 88

SNR signal-to-noise ratio. 21, 63, 77, 79

SR Strehl Ratio. viii, ix, xv, 3, 4, 72, 79, 81, 83–88, 90

TECI TMT early career initiative. 69

TMT Thirty Meter Telescope. iv, 1, 11, 13–15, 18, 47, 71, 72, 75, 93–95

UV Ultraviolet. xii, 9, 10, 19, 20, 43–45

VIS Visible. xii, 9, 10, 19, 20, 43–45

WFE wavefront error. 82, 87, 88

WFS Wavefront Sensor. viii, ix, xiii, xv, 3, 5–8, 14, 15, 48, 49, 54, 71–74, 77, 78, 82–88, 91, 93, 94

Bibliography

Allan A., Edenfeld D., Joyner W. H., Kahng A. B., Rodgers M., Zorian Y., 2002, Computer, 35, 42

Ammons S. M., Gavel D. T., Dillon D. R., Reinig M., Grigsby B., Morzinski K. M., 2008, in Hubin N., Max C. E., Wizinowich P. L., eds, Society of Photo-Optical Instrumentation Engineers (SPIE) Conference Series Vol. 7015, Adaptive Optics Systems. p. 701546, doi:10.1117/12.789816

Andersen D. R., Fischer M., Conan R., Fletcher M., Véran J.-P., 2008, in Hubin N., Max C. E., Wizinowich P. L., eds, Society of Photo-Optical Instrumentation Engineers (SPIE) Conference Series Vol. 7015, Adaptive Optics Systems. p. 70150H, doi:10.1117/12.789792

Andersen D. R., Jackson K. J., Blain C., Bradley C., Correia C., Ito M., Lardiere O., Véran J.-P., 2012, Publications of the Astronomical Society of the Pacific, 124, 469

Anderson J., 2007, HST Instrument Science Report, pp 07–08

Anderson J., King I. R., 2002, Publications of the Astronomical Society of the Pacific, 115, 113

Anderson J., King I. R., 2006, ACS Instrument Science Report, 1

Baffa C., et al., 2001, Astronomy & Astrophysics, 378, 722

Baumgardt H., Vasiliev E., 2021, Monthly Notices of the Royal Astronomical Society, 505, 5957

Baumgardt H., Hénault-Brunet V., Dickson N., Sollima A., 2023, Monthly Notices of the Royal Astronomical Society, 521, 3991

Bernard A., Neichel B., Mugnier L. M., Fusco T., 2018, Monthly Notices of the Royal Astronomical Society, 473, 2590

Besold B., Lindlein N., 1997, Pure and Applied Optics: Journal of the European Optical Society Part A, 6, 691

Boesgaard A. M., Deliyannis C. P., 2023, arXiv preprint arXiv:2307.14473

Bono G., et al., 2009, The Astrophysical Journal Letters, 708, L74

Bono G., et al., 2010, The Astrophysical Journal Letters, 708, L74

Borysow A., 2002, Astronomy & Astrophysics, 390, 779

Borysow A., Jørgensen U. G., Fu Y., 2001, Journal of Quantitative Spectroscopy and Radiative Transfer, 68, 235

Bouchez A. H., et al., 2014, in Marchetti E., Close L. M., Vran J.-P., eds, Society of Photo-Optical Instrumentation Engineers (SPIE) Conference Series Vol. 9148, Adaptive Optics Systems IV. p. 91480W, doi:10.1117/12.2057613

Boyer C., Ellerbroek B., 2016, in Marchetti E., Close L. M., Véran J.-P., eds, Society of Photo-Optical Instrumentation Engineers (SPIE) Conference Series Vol. 9909, Adaptive Optics Systems V. p. 990908, doi:10.1117/12.2232945

Bressan A., Marigo P., Girardi L., Salasnich B., Dal Cero C., Rubele S., Nanni A., 2012, Monthly Notices of the Royal Astronomical Society, 427, 127

Calamida A., et al., 2009, The Astrophysical Journal, 706, 1277

Cameron P. B., Kulkarni S., 2007, AAS, 211, 144

Cardelli J. A., Clayton G. C., Mathis J. S., 1989, Astrophysical Journal, Part 1 (ISSN 0004-637X), vol. 345, Oct. 1, 1989, p. 245-256., 345, 245

Carrasco E. R., et al., 2012a, in Adaptive Optics Systems III. pp 213–230

Carrasco E. R., et al., 2012b, in Ellerbroek B. L., Marchetti E., Véran J.-P., eds, Society of Photo-Optical Instrumentation Engineers (SPIE) Conference Series Vol. 8447, Adaptive Optics Systems III. p. 84470N, doi:10.1117/12.926240

Carretta E. e. a., et al., 2009a, Astronomy & Astrophysics, 505, 117

Carretta E., Bragaglia A., Gratton R., Lucatello S., 2009b, Astronomy & Astrophysics, 505, 139

Carretta E., Bragaglia A., Gratton R., D'Orazi V., Lucatello S., 2009c, Astronomy & Astrophysics, 508, 695

Casali M., et al., 2006, in McLean I. S., Iye M., eds, Society of Photo-Optical Instrumentation Engineers (SPIE) Conference Series Vol. 6269, Ground-based and Airborne Instrumentation for Astronomy. p. 62690W, doi:10.1117/12.670150

Cassisi S., Salaris M., Pietrinferni A., Hyder D., 2017, Monthly Notices of the Royal Astronomical Society, 464, 2341

Chapman S. C., et al., 2018, in Adaptive Optics Systems VI. pp 527–535

Chapman S. C., et al., 2022, in Adaptive Optics Systems VIII. pp 1080–1086

Chen Y., Girardi L., Bressan A., Marigo P., Barbieri M., Kong X., 2014, Monthly Notices of the Royal Astronomical Society, 444, 2525

Chen Y., Bressan A., Girardi L., Marigo P., Kong X., Lanza A., 2015, Monthly Notices of the Royal Astronomical Society, 452, 1068

Cheriton R., et al., 2022, in Advances in Optical and Mechanical Technologies for Telescopes and Instrumentation. p. 121885F, doi:10.1117/12.2619244

Choi J., Dotter A., Conroy C., Cantiello M., Paxton B., Johnson B. D., 2016, The Astrophysical Journal, 823, 102

Ciliegi P., et al., 2024, in Jackson K. J., Schmidt D., Vernet E., eds, Society of Photo-Optical Instrumentation Engineers (SPIE) Conference Series Vol. 13097, Adaptive Optics Systems IX. p. 1309722, doi:10.1117/12.3019058

Conan R., Correia C., 2014, in Marchetti E., Close L. M., Vran J.-P., eds, Society of Photo-Optical Instrumentation Engineers (SPIE) Conference Series Vol. 9148, Adaptive Optics Systems IV. p. 91486C, doi:10.1117/12.2054470

Coppola G., et al., 2011, Monthly Notices of the Royal Astronomical Society, 416, 1056

Coppola G., et al., 2012, Memorie della Societa Astronomica Italiana Supplementi, 19, 190

Crane J., et al., 2018, in Close L. M., Schreiber L., Schmidt D., eds, Society of Photo-Optical Instrumentation Engineers (SPIE) Conference Series Vol. 10703, Adaptive Optics Systems VI. p. 107033V, doi:10.1117/12.2314341

D'Antona F., Caloi V., Montalbán J., Ventura P., Gratton R., 2002, Astronomy & Astrophysics, 395, 69

Davidge T., 2001, The Astronomical Journal, 122, 1386

Davidge T., Rigaut F., Chun M., Brandner W., Potter D., Northcott M., Graves J., 2000, The Astrophysical Journal Letters, 545, L89

Davies R., Kasper M., 2012, Annual Review of Astronomy and Astrophysics, 50, 305

Dell'Agli F., et al., 2018, Monthly Notices of the Royal Astronomical Society, 475, 3098

Diolaiti E., et al., 2010, The Messenger, 140, 28

Diolaiti E., et al., 2016, in Marchetti E., Close L. M., Véran J.-P., eds, Society of Photo-Optical Instrumentation Engineers (SPIE) Conference Series Vol. 9909, Adaptive Optics Systems V. p. 99092D, doi:10.1117/12.2234585

Do T., et al., 2019, Science, 365, 664

Dotter A., 2016, The Astrophysical Journal Supplement Series, 222, 8

Dotter A., Chaboyer B., Jevremović D., Baron E., Ferguson J. W., Sarajedini A., Anderson J., 2007, The Astronomical Journal, 134, 376

Dotter A., Chaboyer B., Jevremović D., Kostov V., Baron E., Ferguson J. W., 2008, The Astrophysical Journal Supplement Series, 178, 89

Dunn J., et al., 2022, in Schreiber L., Schmidt D., Vernet E., eds, Society of Photo-Optical Instrumentation Engineers (SPIE) Conference Series Vol. 12185, Adaptive Optics Systems VIII. p. 121850U, doi:10.1117/12.2630698

Dupuy T. J., et al., 2018, The Astronomical Journal, 156, 57

Faugeras O. D., Luong Q.-T., Maybank S. J., 1992, in European conference on computer vision. pp 321–334

Ferraro F. R., et al., 2009, Nature, 462, 483

Fiorentino G., Tolstoy E., Diolaiti E., Valenti E., Cignoni M., Mackey A., 2011, Astronomy & Astrophysics, 535, A63

Fried D. L., 1982, JOSA, 72, 52

Gach J., et al., 2022, in Adaptive Optics Systems VIII. pp 873–881

Gaia C., et al., 2018, Astronomy & Astrophysics, 616

Gamroth D., et al., 2022, in Schreiber L., Schmidt D., Vernet E., eds, Society of Photo-Optical Instrumentation Engineers (SPIE) Conference Series Vol. 12185, Adaptive Optics Systems VIII. p. 121856I, doi:10.1117/12.2630206

Gemini Observatory AURA 2016, Gemini IRAF: Data reduction software for the Gemini telescopes, Astrophysics Source Code Library, record ascl:1608.006 (ascl:1608.006)

Gendron E., et al., 2011, Astronomy and Astrophysics, 529, L2

Ghez A. M., et al., 2008, The Astrophysical Journal, 689, 1044

Gilles L., Ellerbroek B., 2006, Applied optics, 45, 6568

Gillessen S., et al., 2012, Nature, 481, 51

Gnedin O. Y., Ostriker J. P., 1997, The Astrophysical Journal, 474, 223

Gontcharov G. A., Mosenkov A. V., Khovritchev M. Y., 2019, Monthly Notices of the Royal Astronomical Society, 483, 4949

Gould A., Yee J. C., 2014, The Astrophysical Journal, 784, 64

Gratton R., Sneden C., Carretta E., 2004, Annu. Rev. Astron. Astrophys., 42, 385

Gratton R. G., et al., 2013, Astronomy & Astrophysics, 549, A41

Grillmair C. J., 2019, The Astrophysical Journal, 884, 174

Hardy J. W., 1998, Adaptive Optics for Astronomical Telescopes. Oxford University Press

Hartley R. I., 1993, in Joint European-US workshop on applications of invariance in computer vision. pp 235–256

Herriot G., et al., 2014, in Adaptive Optics Systems IV. p. 914810

Heyden A., Astrom K., 1996, in proceedings of 13th International Conference on Pattern Recognition. pp 339–343

Jackson K., Véran J.-P., Lardière O., Dunn J., Gamroth D., Chapin E., Kumar T., Andersen D., 2023, Research Notes of the American Astronomical Society, 7, 8

Kerley D., et al., 2022, in Schreiber L., Schmidt D., Vernet E., eds, Society of Photo-Optical Instrumentation Engineers (SPIE) Conference Series Vol. 12185, Adaptive Optics Systems VIII. p. 121856H, doi:10.1117/12.2630705

Kraft R. P., Ivans I. I., 2003, Publications of the Astronomical Society of the Pacific, 115, 143

Kumar T., Turri P., Venn K. A., Andersen D. R., Stetson P. B., McConnachie A. W., Taheri M., 2024a, Monthly Notices of the Royal Astronomical Society, 531, 602

Kumar T., Andersen D., Jackson K., van Kooten M. A., Lardiere O., Veran J.-P., 2024b, in Jackson K. J., Schmidt D., Vernet E., eds, Society of Photo-Optical Instrumentation Engineers (SPIE) Conference Series Vol. 13097, Adaptive Optics Systems IX. p. 1309785, doi:10.1117/12.3019212

Lagrange A.-M., et al., 2009, Astronomy & Astrophysics, 493, L21

Lardière O., et al., 2014, in Adaptive Optics Systems IV. pp 527–540

Lee J.-W., 2017, The Astrophysical Journal, 844, 77

Lee J.-W., 2019, The Astrophysical Journal, 883, 166

Lee J.-W., 2021, The Astrophysical Journal Letters, 918, L24

Lin Z., Kumar T., Chen X., Lu J., Wizinowich P., Lilley S., Wetherell E., McConnell N., 2020, in Adaptive Optics Systems VII. p. 1144879

Lindegren L., et al., 2018, Astronomy & Astrophysics, 616, A2

Lohmann A. W., Silva D., 1971, Optics Communications, 2, 413

Lu J., Ghez A., Hornstein S. D., Morris M., Becklin E., Matthews K., 2008, The Astrophysical Journal, 690, 1463

Lu J., Campbell R., Sitarski B., Ghez A., Anderson J., et al., 2016a, Publications of the Astronomical Society of the Pacific, 128, 095004

Lu J., Sinukoff E., Ofek E., Udalski A., Kozlowski S., 2016b, The Astrophysical Journal, 830, 41

Maire A.-L., et al., 2016, in Ground-based and Airborne Instrumentation for Astronomy VI. p. 990834

Marchetti E., et al., 2003, in Adaptive Optical System Technologies II. pp 317–328

Marchetti E., et al., 2007, The Messenger, 129

Marino A. F., et al., 2019, Monthly Notices of the Royal Astronomical Society, 487, 3815

Marois C., Macintosh B., Barman T., Zuckerman B., Song I., Patience J., Lafrenière D., Doyon R., 2008, science, 322, 1348

Massari D., et al., 2015, The Astrophysical Journal, 810, 69

Massari D., et al., 2016a, Astronomy & Astrophysics, 586, A51

Massari D., et al., 2016b, Astronomy & Astrophysics, 595, L2

Massari D., et al., 2016c, in Adaptive Optics Systems V. p. 99091G

Max C., 2001, in American Astronomical Society 197th Meeting.

Mészáros S., et al., 2018, Monthly Notices of the Royal Astronomical Society, 475, 1633

Mieda E., Véran J.-P., Rosensteiner M., Turri P., Andersen D., Herriot G., Lardière O., Spanò P., 2018, Journal of Astronomical Telescopes, Instruments, and Systems, 4, 049002

Milone A., et al., 2008, The Astrophysical Journal, 673, 241

Milone A., et al., 2012, The Astrophysical Journal Letters, 754, L34

Milone A., et al., 2013, The Astrophysical Journal, 767, 120

Milone A., et al., 2014, Monthly Notices of the Royal Astronomical Society, 439, 1588

Milone A., et al., 2017, Monthly Notices of the Royal Astronomical Society, 469, 800

Milone A., et al., 2018, Monthly Notices of the Royal Astronomical Society, 481, 5098

Milone A., et al., 2019, Monthly Notices of the Royal Astronomical Society, 484, 4046

Milone A. P., et al., 2023, Monthly Notices of the Royal Astronomical Society, 522, 2429

Monty S., et al., 2018, The Astrophysical Journal, 865, 160

Moorwood A., Cuby J.-G., Lidman C., 1998, The Messenger, vol. 91, p. 9-13, 91, 9

Moretti A., et al., 2009, Astronomy & Astrophysics, 493, 539

Mueller L., et al., 2022, in Software and Cyberinfrastructure for Astronomy VII. p. 1218922, doi:10.1117/12.2629665

Myers R. M., et al., 2008, in Adaptive Optics Systems. pp 52–60

Neichel B., et al., 2014a, Monthly Notices of the Royal Astronomical Society, 440, 1002

Neichel B., Lu J. R., Rigaut F., Ammons S. M., Carrasco E. R., Lassalle E., 2014b, Monthly Notices of the Royal Astronomical Society, 445, 500

Neisser M., Wurm S., 2013, in Proceedings of the international conference on frontiers of characterization and metrology, Gaithersburg, Maryland.

Neisser M., et al., 2018, Journal of Microelectronic Manufacturing, 1, 1

Norris J. E., 2004, The Astrophysical Journal, 612, L25

Ortolani S., Barbuy B., Momany Y., Saviane I., Bica E., Jilkova L., Salerno G. M., Jungwiert B., 2011, The Astrophysical Journal, 737, 31

Patti M., Fiorentino G., 2019, Monthly Notices of the Royal Astronomical Society, 485, 3470

Pfrommer T., Hickson P., 2010, JOSA A, 27, A97

Piotto G., et al., 2002, Astronomy & Astrophysics, 391, 945

Piotto G., et al., 2015, The Astronomical Journal, 149, 91

Platais I., et al., 2018, The Astronomical Journal, 156, 98

Pollefeys M., Van Gool L., 1997, in International Conference on Computer Analysis of Images and Patterns. pp 175–182

Puget P., et al., 2004, in Ground-based Instrumentation for Astronomy. pp 978–987

Rameau J., et al., 2013, The Astrophysical journal letters, 779, L26

Renzini A., 2013, arXiv preprint arXiv:1302.0329

Renzini A., 2017, Monthly Notices of the Royal Astronomical Society: Letters, 469, L63

Richard C., et al., 2012, Journal of Quantitative Spectroscopy and Radiative Transfer, 113, 1276

Rigaut F., Gendron E., 1992, Astronomy and Astrophysics, 261, 677

Rigaut F., Neichel B., 2018, Annual Review of Astronomy and Astrophysics, 56, 277

Rigaut F. J., Ellerbroek B. L., Flicker R., 2000, in Adaptive Optical Systems Technology. pp 1022–1031

Rigaut F., et al., 2014, Monthly Notices of the Royal Astronomical Society, 437, 2361

Roddier F., 1981, in , Vol. 19, Progress in optics. Elsevier, pp 281–376

Roddier F., 2004, aoa, p. 419

Rodet L., et al., 2018, Astronomy & Astrophysics, 618, A23

Ross C., Chapman S., El-Sankary K., Shafai C., Burley G., Zhou Y., Park B., 2018, in Adaptive Optics Systems VI. pp 1180–1188

Sandler D. G., 1999, Adaptive Optics in Astronomy, 271, 330

Saracino S., et al., 2016, The Astrophysical Journal, 832, 48

Sarajedini A., et al., 2007, The Astronomical Journal, 133, 1658

Sbordone L., Salaris M., Weiss A., Cassisi S., 2011, Astronomy & Astrophysics, 534, A9

Scalco M., et al., 2024, Astronomy and Astrophysics, 689, A59

Schöck M., et al., 2014, in Adaptive Optics Systems IV. p. 91482L

Service M., Lu J. R., Chun M., Suzuki R., Schoeck M., Atwood J., Andersen D., Herriot G., 2019a, arXiv preprint arXiv:1908.04504

Service M., Lu J. R., Chun M., Suzuki R., Schoeck M., Atwood J., Andersen D., Herriot G., 2019b, Journal of Astronomical Telescopes, Instruments, and Systems, 5, 1

Sivo G., et al., 2014, Optics express, 22, 23565

Smith M., Chapin E., Dunn J., Gamroth D., Kerley D., Mueller L., Stocks J., Véran J.-P., 2022, in Software and Cyberinfrastructure for Astronomy VII. p. 1218926, doi:10.1117/12.2630528

Stephens A. W., Frogel J. A., 2002, The Astronomical Journal, 124, 2023

Stetson P. B., 1987, Publications of the Astronomical Society of the Pacific, 99, 191

Stetson P. B., 1990, Publications of the Astronomical Society of the Pacific, 102, 932

Stetson P. B., 1992, in Astronomical Data Analysis Software and Systems I. p. 297

Surendran A., et al., 2022, in Schreiber L., Schmidt D., Vernet E., eds, Society of Photo-Optical Instrumentation Engineers (SPIE) Conference Series Vol. 12185, Adaptive Optics Systems VIII. p. 121851V (arXiv:2207.14433), doi:10.1117/12.2628264

Szigeti L., Mészáros S., Szabó G. M., Fernández-Trincado J. G., Lane R. R., Cohen R. E., 2021, Monthly Notices of the Royal Astronomical Society, 504, 1144

Taheri M., et al., 2022, The Astronomical Journal, 163, 187

Tang J., Bressan A., Rosenfield P., Slemer A., Marigo P., Girardi L., Bianchi L., 2014, Monthly Notices of the Royal Astronomical Society, 445, 4287

Tokovinin A., 2004, Publications of the Astronomical Society of the Pacific, 116, 941

Torres G., et al., 2022, The Astrophysical Journal, 941, 8

Trippe S., Davies R., Eisenhauer F., Schreiber N. F., Fritz T., Genzel R., 2010, Monthly Notices of the Royal Astronomical Society, 402, 1126

Turri P., Andersen D. R., Véran J.-P., Spanò P., Rosensteiner M., McVeigh E. A., 2014, in Adaptive Optics Systems IV. p. 91485Y

Turri P., McConnachie A. W., Stetson P. B., Fiorentino G., Andersen D. R., Véran J. P., Bono G., 2015, The Astrophysical Journal Letters, 811, L15

Turri P., McConnachie A., Stetson P., Fiorentino G., Andersen D., Bono G., Massari D., Véran J.-P., 2017, The Astronomical Journal, 153, 199

Turri P., et al., 2022, in Adaptive Optics Systems VIII. pp 1291–1297

Tyson R. K., 2015, Principles of adaptive optics. CRC press

VandenBerg D. A., Bergbusch P. A., Ferguson J. W., Edvardsson B., 2014, The Astrophysical Journal, 794, 72

VandenBerg D. A., Edvardsson B., Casagrande L., Ferguson J. W., 2022, Monthly Notices of the Royal Astronomical Society, 509, 4189

Vasiliev E., Baumgardt H., 2021, Monthly Notices of the Royal Astronomical Society, 505, 5978

Véran J.-P., McWeigh E., Andersen D., Correia C., Herriot G., Pazder J., 2012, in Adaptive Optics Systems III. p. 844750

Vernin J., Muñoz-Tuñon C., 1994, Astronomy and Astrophysics, 284, 311

Vidal F., Gendron E., Rousset G., 2010, Journal of the Optical Society of America A, 27, A253

Wizinowich P., et al., 2024, in Jackson K. J., Schmidt D., Vernet E., eds, Society of Photo-Optical Instrumentation Engineers (SPIE) Conference Series Vol. 13097, Adaptive Optics Systems IX. p. 130970K, doi:10.1117/12.3017853

Yelda S., Lu J. R., Ghez A. M., Clarkson W., Anderson J., Do T., Matthews K., 2010, The Astrophysical Journal, 725, 331

Ziliotto T., et al., 2023, The Astrophysical Journal, 953, 62